Faculté des Sciences et Technologies de Lille

ÉCOLE DOCTORALE SCIENCES POUR L'INGÉNIEUR
INSTITUT D'ÉLECTRONIQUE, DE MICRO ÉLECTRONIQUE,
ET DE NANOTECHNOLOGIE

THESE

pour obtenir le titre de:

Docteur de l'Université de Lille

Spécialité : Micro et Nanotechnologies,
Acoustique et Télécommunications

présentée et soutenue publiquement le 24 juin 2014 par :

Marie Charoy

Incertitudes des traitements des lésions hépatiques
en radiothérapie stéréotaxique avec asservissement à la respiration

Directeur: Prof. F. Cleri   Co-Encadrant : Dr. N. Reynaert

Devant le jury composé de:

Président :	Prof. Tuami Lasri	IEMN – Université de Lille 1
Rapporteurs :	Prof. Stefaan Vynckier	UCL – Université catholique de Louvain
	Dr. David Sarrut	CNRS – CREATIS – Université de Lyon
Examinateurs :	Prof. Dirk Verellen	UZ – Bruxelles
	Dr. Gregory Delpon	CLCC René Gauducheau – Nantes
	Dr. Xavier Mirabel	CLCC Oscar Lambret – Lille
	Prof. Fabrizio Cleri	IEMN – Université de Lille 1
	Dr. Nick Reynaert	CLCC Oscar Lambret – Lille

THESIS

Faculté des Sciences et Technologies de Lille

ÉCOLE DOCTORALE SCIENCES POUR L'INGÉNIEUR
INSTITUT D'ÉLECTRONIQUE, DE MICRO ÉLECTRONIQUE,
ET DE NANOTECHNOLOGIE

Presented by

Marie Charoy

Uncertainties associated with treatments of hepatic lesions
in stereotactic body radiation therapy (SBRT)
using respiratory tracking

Promoter: Prof. F. Cleri   Co-Supervisor: Dr. N. Reynaert

24th June 2014

Examination committee

President :	Prof. Tuami Lasri	IEMN – Université de Lille 1
Reviewers :	Prof. Stefaan Vynckier	UCL – Université catholique de Louvain
	Dr. David Sarrut	CNRS – CREATIS – Université de Lyon
Examiners :	Prof. Dirk Verellen	UZ – Bruxelles
	Dr. Gregory Delpon	CLCC René Gauducheau – Nantes
	Dr. Xavier Mirabel	CLCC Oscar Lambret – Lille
	Prof. Fabrizio Cleri	IEMN – Université de Lille 1
	Dr. Nick Reynaert	CLCC Oscar Lambret – Lille

À mes parents,
À mes soeurs,

À mes grands-parents,

Contents

List of Figures

List of Tables

List of Abbreviations

3D	Three-Dimensional
4D	Four-Dimensional
AP	Anteroposterior Direction
CC	Craniocaudal Direction
CM	Component Module
COM	Center Of Mass
CT	Computed Tomography
CTV	Clinical Target Volume
D	Dose
DSC	Dice Similarity Coefficient
DVF	Displacement Vector Field
DVH	Dose Volume Histogram
DWI	Diffusion-Weighted Imaging
FDG	Fluorodeoxyglucose
FFD	Free Form Deformation
FSU	Functional Subunit
GTV	Gross Tumor Volume
Gd-MRI	Gadolinium-enhanced Magnetic Resonance Imaging
GUI	Graphical User Interface
Gy	Gray
HBV	Hepatitis B Infection
HCC	Hepatocellular Carcinoma
HCV	Hepatitis C Infection
HU	Hounsfield Unit
ITV	Internal Target Volume
TCP	Tumor Control Probability
LED	Light-Emitting Diode
linac	Linear accelarator

LR	Left-Right Direction
MC	Monte Carlo
MCS	Monte Carlo System
MeV	Mega electron Volt
MLC	Multi Leaf Collimator
MRI	Magnetic Resonance Imaging
MU	Monitor Unit
MV	Megavolt
NTCP	Normal Tissue Complication Probability
OAR	Organ At Risk
PEI	Percutaneous Ethanol Injection
PET	Positron Emission Tomography
PTV	Planning Target Volume
RCT	Randomized Control Trials
RF	Radiofrequence
RFA	Radiofrequency Ablation
RPM	Real-time Position Management System
	(Varian ® Medical Systems, Palo Alto, CA)
SI	Superior-Inferior Direction
Rv	Volume Ratio
SBRT	Stereotactic Body Radiation Therapy
SRTS	Synchrony Respiratory Tracking System
TPS	Treatment Planning System
US	Ultrasound
UTC	Uncomplicated Tumor Control
VOI	Volume Of Interest

Summary

Oscar Lambret Center treated with Cyberknife®, since June 2007, liver lesions in stereotactic conditions with respiratory tracking using external LEDs correlated with seeds implanted near the target. Clinical results show excellent local control but there are still uncertainties in the preparation and delivery of treatment. The aims of this thesis are to identify and quantify these uncertainties, to define solutions and/or alternatives and to assess their added value.

As a first step, the method of the target definition by the radiation oncologist is evaluated. Improvement of the method currently used in routine is considered, including the choice of the most appropriate imaging and the intervention of a second operator, expert in imaging (radiologist).

The organ at risk and target movements induced by the respiratory motion are not taken into account in the treatment planning step, performed on the 3D images (the so-called planning CT). The dosimetric impact associated with this type of planning is evaluated using 4D Monte Carlo simulations that take into account patient and linear accelerator movements and the synchrony between both movements. The question of 4D planning as prospect of improvement is then investigated.

Movements and deformations of the liver due to respiration are also implicated in the uncertainties involved in the treatment. The correlation model of external markers with the target, used for respiratory tracking, ignores eventual deformations and rotations within the liver. A study of the impact on the target tracking is performed.

All these studies were conducted using real patient data sets.

Résumé

Le Centre Oscar Lambret traite avec le Cyberknife®, depuis juin 2007, les lésions hépatiques en conditions stéréotaxiques, avec un asservissement à la respiration par des repères externes corrélés à des grains implantés près de la cible. Les résultats cliniques montrent un excellent contrôle local mais il subsiste des incertitudes lors de la préparation et de la réalisation du traitement. Cette thèse consiste à identifier et quantifier ces incertitudes puis à déterminer des solutions et/ou des alternatives et d'en évaluer l'intérêt.

Ainsi, la méthode de définition de la cible par le radiothérapeute est évaluée. Une amélioration de la méthode actuellement en place en routine est envisagée, notamment par le choix de l'imagerie la mieux adaptée ainsi que par l'intervention d'un deuxième opérateur, expert en imagerie (radiologue).

Les mouvements des organes à risques et cibles induits par la respiration ne sont pas pris en compte lors de l'étape de planification, effectuée sur les images 3D en amont du traitement. L'impact dosimétrique associé à ce mode de planification est évalué grâce à des simulations Monte Carlo 4D. La question d'une planification 4D comme perspective d'amélioration est alors posée.

Les mouvements et déformations du foie dus à la respiration sont également mis en cause dans les incertitudes intervenant au cours du traitement. Le modèle de corrélation des repères externes avec la cible, utilisé pour l'asservissement respiratoire, ne tient pas compte des déformations et des rotations possibles au sein même du foie. Une étude des conséquences sur le suivi de la cible est effectuée.

Toutes ces études ont été menées à partir de données réelles de patients.

Introduction

Cancer is a leading cause of death worldwide, causing 8.2 million deaths in 2012, including 745,000 deaths due to liver cancer. The number of cancer cases per year is expected to increase from 14 million in 2012 to 22 million in the next two decades [7]. The number of new cancer cases in France was estimated at 355,000 in 2012 [8]. Thanks to screening and cancer treatment improvements, prognosis improves in France [9]. Many treatment modes are used to treat cancers. Among them, radiation therapy consists of the use of high energy ionizing radiation with biological effects leading the destruction of cancer cells. 70% of patients with cancer resort to radiotherapy during their treatment process [10]. This treatment mode is often combined with surgery and/or chemotherapy. It is also used in the context of palliation or symptomatic care, particularly in the case of liver cancers where radiation plays a limited role because of its extremely damaging effects on healthy liver tissue.

Technological advances in the field of external radiotherapy led to a dazzling evolution of radiotherapy over the past fifty years. Conventional radiotherapy has evolved first into the 3D conformal radiotherapy (3D CRT), more focused, protecting healthy organs and causing fewer side effects, and to conformal radiotherapy with intensity modulation (IMRT), which allows to propose a treatment really "carved" in the shape of the tumor. Recently, the respiratory-gated radiotherapy even takes into consideration the respiratory movements during irradiation of thoracic and abdominal tumors.

The rise in accuracy and performance through these technological advances allow an increase in dose to the target while better protecting the surrounding healthy tissue. Decrease of treatment uncertainties is an im-

portant factor required to escalate the dose. The sources of uncertainty are multiple during treatment with external beam radiation. Indeed, a large number of steps are involved between the dose prescription and the actual dose delivery. During this process, each step introduces a certain amount of uncertainty, accumulating in an overall uncertainty on the absolute dose delivered to the patient. Uncertainties may be related to treatment planning, intrinsic errors of operating devices and errors due to inter-and intrafraction patient movements (respectively the positioning and the organ movements during breathing). A good knowledge of the uncertainties of a treatment mode is essential to ensure the correctness of the dose received by the patient.

Because of variations in tumor and normal tissue response, it is difficult to quantify the impact of geometric and dosimetric uncertainties in a clinical setting. However, it is custom to fix the maximum dose uncertainty of 5% [11] [12]. Beyond, the dose error can lead to significant variations in the tumor control probability (TCP) and the normal tissue complication probability (NTCP). Clinical effects have been noticed for dose errors of 7% [13].

The main objective of this thesis is to quantify the various uncertainties related to a CyberKnife treatment with respiratory tracking for patients with liver cancer. Uncertainties in three steps of the treatment procedure are considered: the method of target delineation by the radiation oncologist, then handling of internal movements during optimisation of the treatment plan, and handling of these movements during the treatment delivery (tracking).

This thesis is divided into five chapters. The first chapter provides an introduction to clinical basics of the anatomy, the functions and the role of the liver. The different types of liver cancers are also briefly described. The second chapter reminds the basic concepts of the physics of ionizing radiation, which is the base of treatment techniques in radiotherapy, and provides an explanation on the CyberKnife device and on the various imaging modalities. The bases of Monte Carlo simulations that will be used during dosimetric studies are also developed. The first two chapters are intended to introduce the clinical and technical basic notions to which

the scientific studies presented in this thesis refer.

In the third chapter, we consider the benefits and disadvantages brought by MRI for tumor delineation as an alternative to CT images. The method currently used in routine is first evaluated, especially by the determination of the reproducibility of the contouring. The comparison between target contours twice performed by the same radiation oncologist, on CT images with contrast enhancement, allows determining this reproducibility. The inter-operators reproducibility of contouring has also been determined by the comparison of the target contouring, on the same enhanced CT images, between two physicians. The dosimetric impact of the contrast product in CT images for treatment planning is another source of uncertainty that was evaluated. Next we focus on the efficiency gain provided by the new contouring method. The reproducibility intra-operator of the target contouring based on MR images has been evaluated in the same way as for the study regarding the contouring based on CT images. The feasibility of its implementation in routine is assessed at the technical and organizational levels. MR images must be supported by the TPS and their interpretation must be fully understood and controlled before being used as a tool for dosimetric calculation. Potential organizational changes for radiation oncologists, imposed by the new method, are also estimated.

In the fourth chapter, we quantify the uncertainty caused by the liver deformation when treating a patient with CyberKnife respiratory tracking. Firstly, the movements and deformations of liver during the respiratory cycle are observed, and then the correlation between the movements of the tumor and those of internal markers tracked during treatment is evaluated by two different methods. One method is based on combined 4D PET-CT; the delineation is performed on the PET images and the CT images are used to determine the fiducial location. The second method is based solely on the 4D CT images, and a 4D deformable registration is used to define the target volumes on each respiratory phase. The utility of the treatment mode using the respiratory tracking system is discussed according to several patient characteristics.

In the last chapter, the dosimetric uncertainty related to organ movement during breathing is determined using Monte Carlo simulation. At first,

we present the MCS Monte Carlo calculation software that simulates the photon beam produced by the CyberKnife. In a second step the dosimetric calculations are explained. These calculations, based on a treatment plan and on 4D CT images, give a more realistic result of the dose actually delivered taking into account the organ motion during the respiratory cycle. The impact of the respiratory motion on the target coverage and on the organs at risk is studied.

In conclusion, we make the synthesis of the results obtained during this thesis and develop the perspectives.

Chapter 1

Clinical Notions

1.1 Liver

The liver is one of the most complex organs in the body. It is a gland performing an astonishingly large number of tasks that impact all body systems. Liver anatomy can be described using two different aspects: morphological anatomy and functional anatomy.

1.1.1 Liver anatomy

1.1.1.1 Morphological anatomy

The liver is the second largest organ in the human body after the skin, and the largest gland. A human liver normally weighs between 1.20 Kg and 1.60 Kg. Chan *et al.* [14] determined a formula to estimate liver weight of adults. The estimated standard liver weight (ESLW) is defined with the Equation 1.1 (with gender = 0 for a female and gender = 1 for a male, and BW the body weight):

$$ESLW(g) = 218 + BW(kg) * 12.3 + gender * 51 \qquad (1.1)$$

The liver is a reddish brown organ, wedge-shaped, with its base to the right and its apex to the left. It has a soft consistency, and is highly vascular and easily friable. The liver is the only human organ that has the remarkable property of self-regeneration in case of injury. If a part of the liver is removed, the remaining parts can grow back to its original size and shape.

Located in the upper right portion of the abdominal cavity and extended to the left upper abdomen, the liver is divided by fissures (*fossae*) into four lobes of different size and shape: the **right** (the largest lobe), **left**, **quadrate** and **caudate** lobes. It lies to the right of the stomach and overlies the gallbladder.

Visceral peritoneum covers most of the surface of the liver. The peritoneum folds back on itself in several places to form five ligaments: the membranous **falciform** (also separates the right and left lobes), **coronary**, **right** and **left triangular ligaments**, and the **fibrous round ligament** (which is derived from the embryonic umbilical vein).
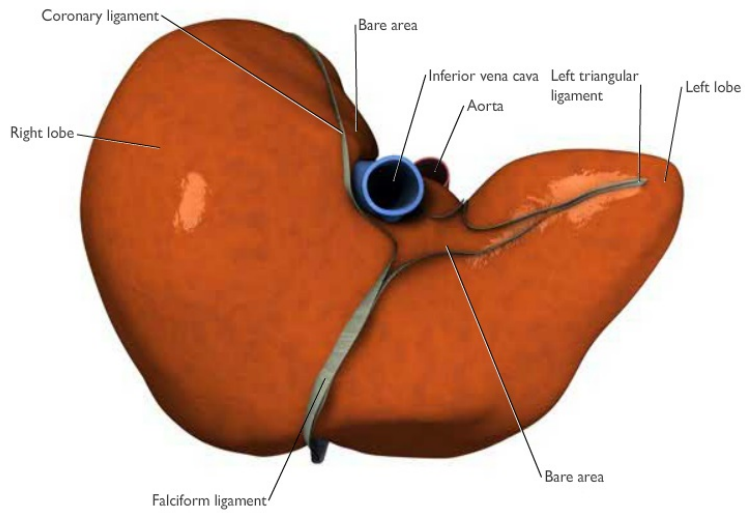
(a) superior view
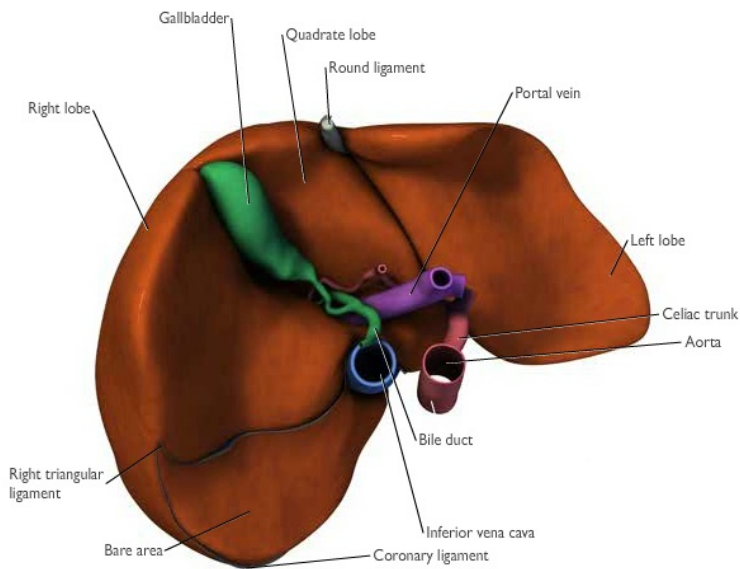
(b) inferior view

Figure 1.1: Liver morphological anatomy in different views
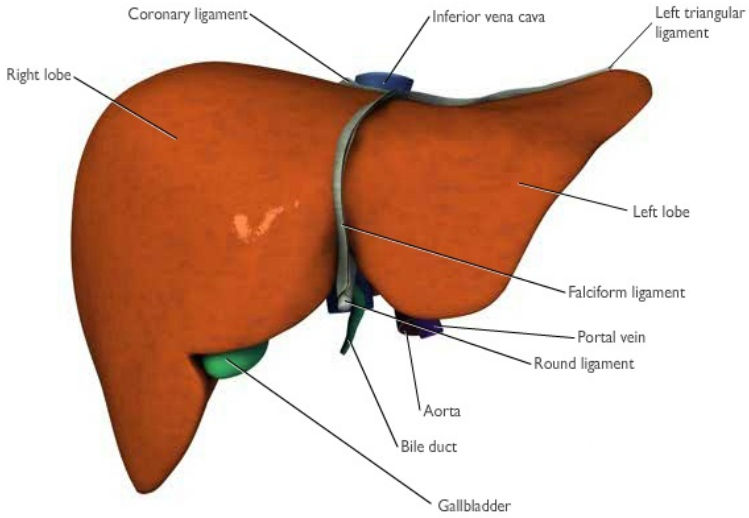
(a) anterior view
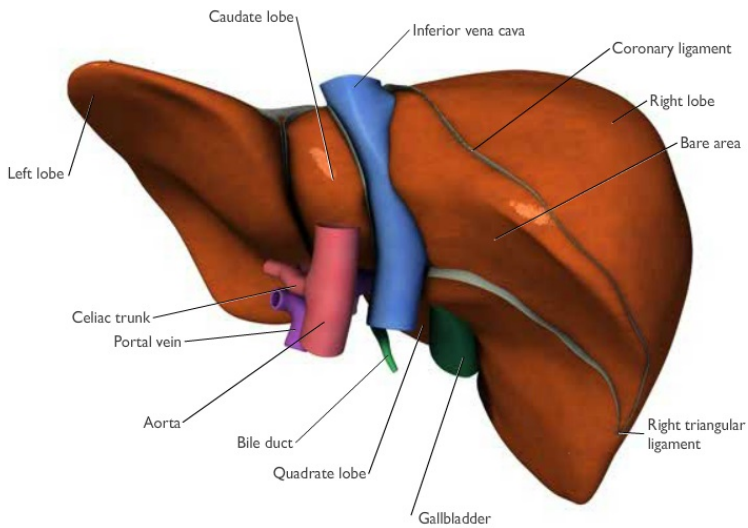
(b) posterior view

Figure 1.2: Liver morphological anatomy in different views

1.1.1.2   Functional anatomy – Couinaud classification

The central area where the common bile duct, portal vein, and hepatic artery enter is the hepatic hilum. A main portal fissure containing the middle hepatic vein divides the liver into functional left and right lobes. The left and right lobes of the liver are supplied by the branches constituted by the duct, vein and artery.
In the Couinaud classification of liver anatomy, the two functional lobes are further divided into a total of eight functionally independent segments. The segments separation is based on the blood flow system.

The liver is located between two veins (portal vein and hepatic vein) in addition to the hepatic artery that supplies 20% of the liver's blood. The **portal vein** is a blood vessel that conducts blood from the gastrointestinal tract to the liver. The liver deoxygenates and cleans blood of the stomach, pancreas, small intestine and colon. The cleaned blood leaves the liver to the heart in the **hepatic veins**.

The hepatic vein is separated in three main branches in the liver:

– **Right hepatic vein** divides the right lobe into anterior and posterior segments.
– **Middle hepatic vein** divides the liver into right and left lobes. This plane runs from the inferior vena cava to the gallbladder fossa.
– **Left hepatic vein** divides the left lobe into a medial (segment IV) and lateral part (segments II and III).

Portal vein divides the liver into upper and lower segments. The left and right portal vein branches superiorly and inferiorly project into the center of each segment.

Fig 1.3 is a schematic presentation of the liver segments. In reality the proportions can be different. The numbering of the segments is in a clockwise manner. Segment I, corresponding to the caudate lobe, is posterior located. Segment IV is sometimes divided into segment IVa and IVb. On a normal frontal view the segments VI and VII are not visible because they are located more posterior. The right border of the liver is formed by segment V and VIII.
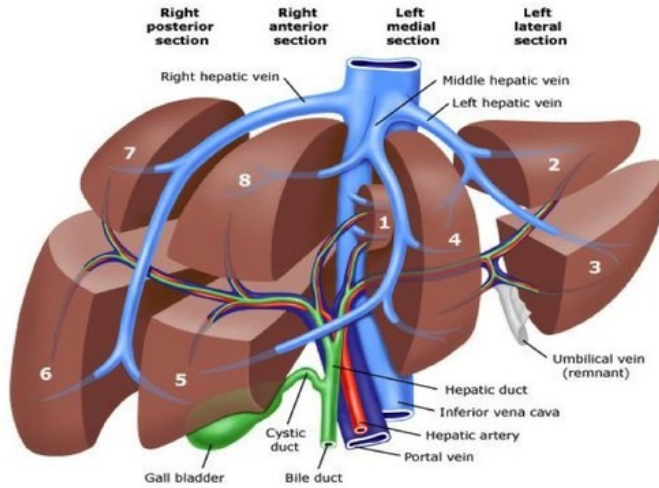
Figure 1.3: Couinaud segments and blood flow system, in anterior view [1]

Each segment has its own vascular inflow, outflow and biliary drainage; in the centre of each segment there is a branch of the portal vein, hepatic artery and bile duct, and in the periphery of each segment there is vascular outflow through the hepatic veins.

Because of this division into self-contained units, each segment can be resected without damaging those remaining. For the viable liver remaining, resections must proceed along the vessels that define the peripheries of these segments.

Anatomic lobes	Couinaud segments
Caudate	I
Lateral	II, III
Medial	IVa, IVb
Right	V, VI, VII, VIII

Table 1.1: Anatomic lobes and Couinaud segments correspondence
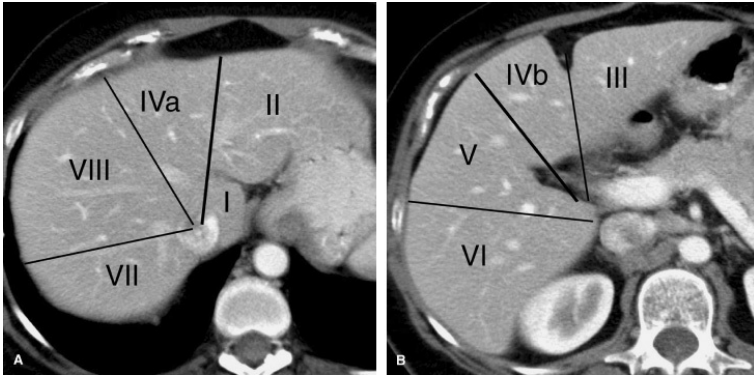
Figure 1.4: Couinaud segments on a CT slice [2]

1.1.2   Functionality

The liver provides a wide range of vital functions, including detoxification, protein synthesis, and production of biochemical necessary for digestion.

– The **secretion of bile** is performed from the hepatocytes, the main liver cells. The bile helps in fats digestion process and in the absorption of substances such as vitamins A, D, E, and K. The bile is stored in the gallbladder and released into the intestines as needed. It is excreted throughout the bile ducts.

– The liver plays a role in the **metabolism of carbohydrates**, **lipids** (source and excretion of cholesterol) and **proteins** as fibrinogen, the major clotting protein in blood plasma.

– **Glycogen**, **iron** and a large number of **vitamins** (A,D and B12) are stored in the liver.

– The liver participates in the **detoxification of the body** removing waste in the blood, especially toxic substances (drugs, consumed alcohol and toxins). It synthesizes urea to excrete nitrogenous waste. It works with the body's immune system to fight harmful cells and substances that threaten the organism. The liver will capture, process and make inoffensive the toxics exposed to by eating, drinking or breathing.

1.1.3   Movements and Deformations

The movement of the rib cage and thoracic and abdominal organs are the result of the diaphragm contraction/relaxation, the principal driver of respiration.
The diaphragm is a muscle, inserted into the lower ribs, forming a dome above the abdominal organs and that separates them of the thoracic organs. During contraction, the top of the diaphragm goes down; this results in compressing the abdominal area and expanding the thoracic area. During relaxation, the diaphragm relaxes naturally and abdominal organs return to their original place.

The liver is located in the upper right abdominal cavity, under the right diaphragmatic dome. Therefore, the liver is directly exposed to the effects of the movement of the diaphragm. As discussed in some studies, liver motion occurs primarily in the craniocaudal direction (CC) direction in the order of 10 mm. The movements in the left-right (LR) and antero-posterior (AP) directions are lower. [15] [16]

The liver is an organ with a density similar to soft tissue and that undergoes deformation during breathing [17]. It is a voluminous organ, which extends to the left side of the abdomen and reaches the intestines, this could enable motion dissimilarities between the different parts of the liver. General models of organ motion during respiratory cycle are based on the study of a reference population. Taking into account individual characteristics provides more accurate models. [18]

Two types of movements have to be distinguished during liver treatment by external radiotherapy: the **intra-fraction** movements, corresponding to movements generated by respiration during a treatment session, and the **inter-fraction** movements corresponding to the differences in positioning between two treatment sessions.

1.2   Hepatic Cancers

According to the World Health Organisation, cancer is a leading cause of death worldwide, accounting for 13% of all deaths. Liver cancer accounts

for 700,000 deaths (in 2008) and is the third leading cause of cancer related death, exceeded only by cancer of the lung and stomach including liver cancers from metastases such as the gut. [19]

Hepatic cancer consists of malignant tumors growing on the surface or inside the liver. There are two distinct types of liver cancer called the primary liver cancer and the metastatic liver cancer.
The primary liver cancer starts in the liver while the metastatic liver cancer is the spreading to the liver of a cancer originating in another organ. Several types of primary liver cancer exist, such as cholangiocarcinoma, angiosarcomas, hepatoblastomas and hepatocellular carcinoma (HCC). The HCC accounts for between 85% and 90% of primary liver cancers. [20]

1.2.1   Hepatocellular Carcinoma

1.2.1.1   Diagnosis

Liver tumors may be detected by medical imaging equipment (sometimes by coincidence) or by a physical examination. During this examination, the diagnosis of liver cancer is based on a set of characteristic symptoms as an abdominal mass, abdominal pain, jaundice, nausea or liver dysfunction.

To confirm a diagnosis of liver cancer and to characterize it, many imaging modalities are available. These include ultrasound (US), computed tomography (CT), magnetic resonance imaging (MRI) and positron emission tomography (PET). Blood tests and sometimes biopsy are needed to determine the malignancy of the tumor. [21]

1.2.1.2   Causes

The causes inducing hepatocellular carcinoma are not clearly defined. However, certain risk factors favoring the development of HCC are well established, this is the case for:

Hepatitis C infection (HCV)
This is one of the primary causes of liver cancer. [22] Hepatitis C virus

infection usually requires direct contact with infected blood, either from contaminated blood products or needles. The chronic hepatitis C infection is a leading cause of cirrhosis.

Hepatitis B infection (HBV)

In patients with both chronic hepatitis B virus and liver cancer, the genetic material of hepatitis B virus is frequently found to be part of the genetic material of the cancer cells. It is thought, therefore, that specific regions of the hepatitis B virus genome (genetic code) enter the genetic material of the liver cells. This hepatitis B virus genetic material may then disrupt the normal genetic material in the liver cells, thereby causing the liver cells to become cancerous.

This infection can be caught from contaminated blood products or used needles, sexual contact or from contamination at birth. The hepatitis B infection is a cause of cirrhosis, and is considered the primary cause of approximately 80% of cases worldwide. [23]

Cirrhosis

Cirrhosis is a serious disease that develops when liver cells are damaged and replaced with scar tissue. Many exposures cause cirrhosis, including HBV or HCV infection, heavy alcohol use, too much iron stored in the liver, and certain drugs. Most cases of liver cancer occur in people who first had cirrhosis, usually resulting from HBV or HCV infection, or from heavy alcohol use.

Alcohol

Heavy chronic alcohol consumption is a leading cause of cirrhosis. It is the most common association of liver cancer in the developed world [24]. Alcohol adds to the risk of developing liver cancer in patients with chronic HBV or HCV infection.

Diabetes and obesity

Although it is hard to separate the effects of diabetes from obesity on the liver, both conditions can cause chronic damage and accumulation of fat within the liver. Not only is the chance of developing cancer enhanced, but patients with diabetes who undergo surgical removal of liver cancer have a higher chance of cancer relapse. [25]

The more risk factors a person has, the greater the chance that liver cancer will develop. However, many people with known risk factors for liver cancer don't develop the disease. The most common risk factors identified include cirrhosis and hepatitis B and C. [23]

1.2.1.3   Management

Not all patients with liver cancer are potentially curable; certain treatments are delivered with a palliative aim. The liver cancer treatments choice is depending on:

- the liver's condition
- the size, location and number of tumors
- eventual spreading outside the liver
- the patient age and overall health

Staging classification, summarized on Figure 1.5, has been proposed by the Barcelona Clinic Liver Cancer (BCLC). This staging system groups HCC patients in four different categories and links staging with treatment indication. Stage A includes patients with asymptomatic early tumors suitable for radical therapies (resection, liver transplantation or percutaneous treatments). Intermediate stage (B) comprises patients with asymptomatic multinodular HCC and the advanced stage (C) includes patients with symptomatic tumors and/or an invasive tumor pattern. Stage B and C patients may receive palliative treatments/new agents in the setting of phase II investigations or randomized controlled trials. End-stage disease, the stage D, contains patients with extremely grim prognosis that should merely receive symptomatic treatment. [3]

Below is the description of the different treatment techniques used :

- **Resection** consists in the removal of the tumor from the liver. It is a partial hepatectomy.
- **Liver transplantation** is a total liver replacement.
- **Cryosurgery**: use of a metal probe to freeze and destroy cancer cells.
- **Radiofrequency Ablation(RFA)**: use of a special probe to destroy cancer cells with heat.
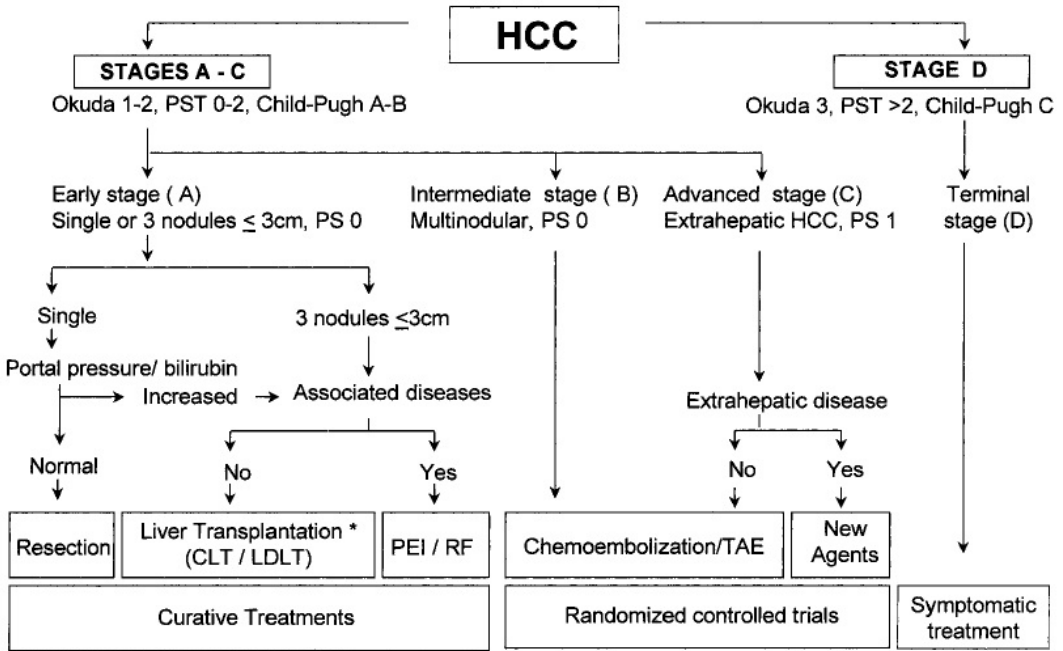
Figure 1.5: Barcelona-Clinic Liver Cancer (BCLC) staging classification and
treatment schedule [3]

– **Ethanol Injection (PEI)**: Ethanol (achohol) is injected directly into
  the liver tumor to destroy cancer cells.
– **Chemotherapy or chemoembolization**: use of drugs to destroy can-
  cer cells. In some cases, the drugs can be directly injected into the liver
  tumor.
– **Radiation therapy**: use of high-energy radiation to destroy cancer
  cells.
– **Sorafenib**: an oral medication for use in advanced cases of hepatocel-
  lular carcinoma.

Hepatic resection, radiofrequency ablation, and liver transplantation are
accepted as an effective treatment for HCC. [26] [27]

Liver transplantation is the only option that provides a cure for both the
tumor and the underlying chronic liver disease. Liver transplantation is
recognised as the best treatment for patients with a unique HCC smaller

than 5 cm in the setting of final stage of cirrhosis and for those with early multi focal disease (up to 3 lesions, no more than 3cm). [28]

Resection is the most favored treatment for HCC in non-cirrhotic patients, who account for about 5% of the cases in Western countries.

The powerful technique used for local ablation of HCC is percutaneous ethanol injection (PEI). PEI is a well-established technique for the treatment of nodular-type HCC. The disadvantage of PEI is the high local recurrence rate, which may reach 33% in lesions smaller than 3 cm and 43% in lesions exceeding 3 cm [29] [30]. Moreover, PEI is unable to create a safety margin of ablation in the liver parenchyma surrounding the nodule, and therefore may not destroy tiny satellite lesions that even in small tumors may be located in close proximity to the main nodule.

RFA imaging techniques such as US, MRI and CT are used to guide the needle electrode into the specific site of the tumor. RFA has been the most broadly assessed alternative to PEI for local ablation of HCC. [31]

Randomised control trials (RCT) have proved that RFA is superior to PEI in the treatment of small HCCs in terms of treatment response, recurrence, and overall survival rates, while some literature report that RFA have higher complication rates.

1.2.1.4   Statistics and Prognosis

Hepatocellular carcinoma is the fifth most common malignancy in men and eighth in women worldwide [19]. Epidemiologically, HCC is most common in Asia and sub-Saharan Africa [23]. HCC worldwide characteristically occurs in the settings of cirrhosis and chronic hepatitis virus infections. Hepatitis B and C account for more or less 80% of cases globally [19].

In patients suffering from hepatocellular carcinoma, secondary spread is common. The most common sites of metastasis from HCC are the lungs (52%) and the lymphatic system (27%), usually occurring at the porta hepatis, celiac axis and around the pancreatic head.
The type and the stage of a patient cancer is important in estimating

their outlook, but many other factors may also affect a patient outcome, such as the overall health (chronic disease, cirrhosis of the liver...), the treatment received and the cancer response to treatment. Even when taking all factors into account, survival rates are rough estimates.
The X-year survival rate refers to the percentage of patients who live at least X years after their cancer is diagnosed. It does not give indication on the maximum survival time. The relative survival rates compare the observed survival with that expected for people without the cancer.

The numbers below are obtained from the National Cancer Institute's Surveillance, Epidemiology, and End Results (SEER) database, and are based on American patients who were diagnosed with HCC between 2003 and 2009 [32]. The 5-year relative survival rates are presented for different groups cancer cases:

– 28% for localized cancer, that means the cancer is still confined to the liver, and includes stages I, II, and some stage III cancers. This includes a wide range of cancers, some of which are easier to treat than others.

– 7% for regional cancer, that means the cancer has grown into nearby organs or has spread to nearby lymph nodes, and includes stages IIIC and IVA cancers.

– 2% for distant cancer, means that the cancer has spread to distant organs or tissues and is the same as stage IVB.

For all stages combined, the relative 5-year survival rate from liver cancer is about 15%. Part of the reason for this low survival rate is that most patients with liver cancer also have other liver problems such as cirrhosis, which by itself can be fatal.
In general, survival rates are higher for people who can have surgery to remove their cancer, regardless of the stage. For example, studies have shown that patients with small, resectable tumors who do not have cirrhosis or other serious health problems are likely to do well if their cancers are removed. Their overall 5-year survival is over 50%. For people with early-stage liver cancers who are able to have a liver transplant, the 5-year survival rate is in the range of 60% to 70%.[32]

1.2.2 Metastatic Liver Cancer

The metastatic liver cancer corresponds to the presence of one or several tumors associated with fixing cancer cells from another location.
Metastatic adenocarcinoma is the most common type of liver tumor. [33]
It develops most often after a digestive cancer, particularly colorectal cancer. Lung and breast cancers are also generators of liver metastases.
As for the primary cancer, the diagnosis is based on physical examination, anatomic and functional imaging, blood test and sometimes biopsy.

1.2.2.1 Causes

Primary cancer cells invade lymph nodes and blood vessels near a tumor and spread to other parts of the body. A liver metastasis is a cancerous tumor that has spread to the liver. The cancerous cells from the location of the primary cancer are found in a metastatic liver tumor.

The risk that cancer will metastasize to the liver depends on the location of the original cancer. The most common sources of liver metastases are primary lung, breast, and colorectal carcinomas. [33] Approximately 50% of patients with colorectal carcinoma develop liver metastases at some point during the course of their disease. [34]

Even if the primary cancer was removed or cured, liver metastasis can still occur years later.

1.2.2.2 Metastasis process

There are six steps in the metastasis process. Not all cancers follow this process, but most do. [35]

– **Local invasion**: Cancer cells move from the primary site into nearby normal tissue.

– **Intravasation**: Cancer cells move through the walls of nearby lymph vessels and blood vessels.

– **Circulation**: Cancer cells migrate through the lymphatic system and the bloodstream to other parts of the body.

– **Arrest and extravasation**: Cancer cells stop moving when they reach a distant location. They then move through the capillary (small blood vessel) walls, and invade nearby tissue.

– **Proliferation**: Cancer cells grow at the distant location and create small tumors called micrometastases.

– **Angiogenesis**: Micrometastases (small tumors created by cancer cells) stimulate the creation of new blood vessels, which supply the nutrients and oxygen needed for tumor growth.

1.2.2.3   Management

Several options are currently used for treating metastatic liver cancer. They can be grouped into two types, the systemic therapy and the localized therapy. Systemic cancer therapies treat the whole body through the bloodstream while localized therapies target only tumor cells and nearby tissue.

The Systemic therapies include:

– **Chemotherapy**, a treatment that uses drugs to kill cancer cells.
– **Biological response modifier (BRM) therapy**, a treatment that uses certain antibodies, growth factors, and vaccines designed to boost or restore the immune systems ability to fight cancer.
– **Targeted therapy**, uses drugs and other agents, which are antibodies designed to identify and attach to specific parts of cancer cells, to facilitate targeted treatment with drugs, radiation, or by blocking growth of cancerous cells.
– **Hormonal therapy** that consists in adding, in blocking, or in removing hormones to slow or stop the growth of tumors. Principally used for breast and prostate cancer.

Localized Therapies include:

– **Radiation therapy**, uses high-energy external or internal radiation to kill cancer cells and shrink tumors. Radiotherapy is generally used in palliative treatment as it is quite inefficient for treatment of metastasis.[36].

– **Surgical removal**. This is the most effective solution in terms of survival. The resection requires a single (or few) and well localized metastases, and that the patient has a good condition. Only 10% to 25% of patients are candidates for surgical resection of their liver metastasis.[34]

Generally, the choice of treatments will depend on:

- the patients age and overall health
- the size, location and number of metastatic tumors
- the location of the primary cancer
- he types of cancer treatment the patient had in the past

1.2.2.4 Prognosis

Often the evolution of metastatic liver cancer is not very good, because the presence of metastases is a sign that the cancer of origin began to "swarm" around the body. The relative success of treatment depends on the location of the primary cancer and how much of it has spread to the liver. Current research is looking for new ways to fight and kill cancer cells, such as hyperstimulating the immune response and disrupting individual steps in the metastatic process.

Chapter 2

Technical Notions

2.1   External radiotherapy

External radiation therapy involves destroying cancer cells through rays produced by an external source. The goal of radiation therapy is to maximize its effectiveness on the tumor while minimizing toxicity to healthy tissue and surrounding organs, also known as organs at risk.

These rays are emitted by a machine called linear accelerator, and directed at the tumor. The radiation type most commonly used are high-energy photons beams. More rarely, electron, proton or heavy ion beams are also used. This thesis work relates only photon beam radiotherapy.

2.1.1   Radiation Interactions

X-rays consist of particles called photons, without mass and charge, but with a non-zero energy and momentum. Photons are indirectly ionizing, i.e. they create ionizing particles by interactions with matter. They are also absorbed or scattered in matter (e.g. tissue).

The photons interact with the electrons of the material by three different effects:

– **Photoelectric effect**: The photon travelling through a medium is absorbed by an atomic electron of the medium, which causes ejection of this electron and the photon disappearance. The electron receives all the photon energy (minus the binding energy).

– **Compton scattering**: The photon is scattered from an atomic electron of the medium (electron considered as free), which leads to the atom ionization. The electron receives a part of the photon energy and the photon is scattered with a lower energy.

– **Pair production (or materialization)**: when a high-energy photon enters in the Coulomb field of a nucleus (possibly of an electron), it can materialize into a positron/electron pair. The incident photon energy must be higher than or equal to 1.022 MeV.

Figure 2.1 shows the three areas of predominant interaction modes as a function of incident photon energy and atomic number (Z) of the medium. In all cases, the ionizing particles created by radiation/matter interactions will deposit their energy along their path in matter.
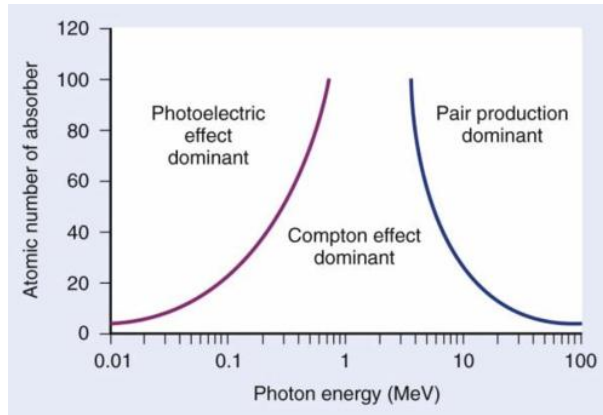
Figure 2.1: Interaction dominance zones

2.1.2 Dose

2.1.2.1 Definition

The absorbed dose by a material element corresponds to the deposited energy in the volume element caused by radiation/matter interactions divided by the mass of the volume element. The dose is measured in Gray (Gy). One gray is equal to an energy deposition of one Joule in one kilogram of matter (Equation 2.1):

$$1 Gy = 1 J.kg^{-1} \tag{2.1}$$

2.1.2.2 TCP/NTCP

The aim of radiotherapy is to get the best possible therapeutic ratio tumor local control versus morbidity. The most important dose-limiting factor is the functional tolerance of the surrounding tissues to radiation, which depends on their ability to continue to operate as an entity, and therefore on their architecture. Each element is considered as being composed of functional sub-units (FSUs) with a particular organization. FSUs in an organ can be organized in series or parallel.

– In **Series**: the damage in one portion of the organ may cause the total organ failure (e.g. gastrointestinal tract and spinal cord).

– In **Parallel**: the organ function is often maintained since the undamaged part operates independently from the damage part. The whole organ is very sensitive to irradiation but a high dose to a small volume is tolerable (e.g. lung or kidney).

The Tumor Control Probability (TCP) and the Normal Tissue Complication Probability (NTCP) are two models that predict the impact of partial or global irradiation on tumor and normal organ converting the dose into biological predictions. A third parameter, called Uncomplicated Tumor Control (UTC) can be defined from the TCP and NTCP (Equation 2.2). The evaluation of probability of induced complications to normal surrounding tissues is based on published data and clinical experience.

Figure 2.2 represents the TCP, NTCP and UTC depending on the dose. The probability of tumor control without normal issue complications (UTC) receives its maximum in the so-called "therapeutic window".
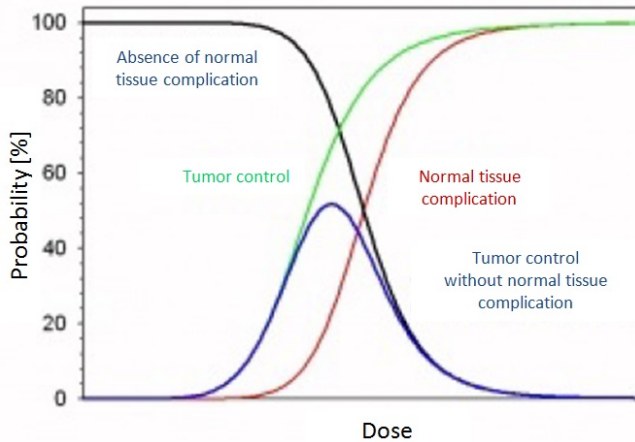
Figure 2.2: Dose dependence of tumor control probability (TCP) and normal tissue complication probability (NTCP)

$$UTC = TCP(1 - NTCP) \qquad (2.2)$$

The NTCP is a function of a total and fraction dose, fraction number and irradiated volume. [37] The dose response relationship is described for each organ in different tables of values depending on the fractionation of the treatment.

2.1.2.3 Dose Volume Histogram

The dose volume histogram (DVH) is a graphical representation of the dose distribution in the volume of organs, with the dose on the abscissa and the percentage volume of the organ on the ordinate. This is currently the way that most fully describes the dose received by an organ at risk.
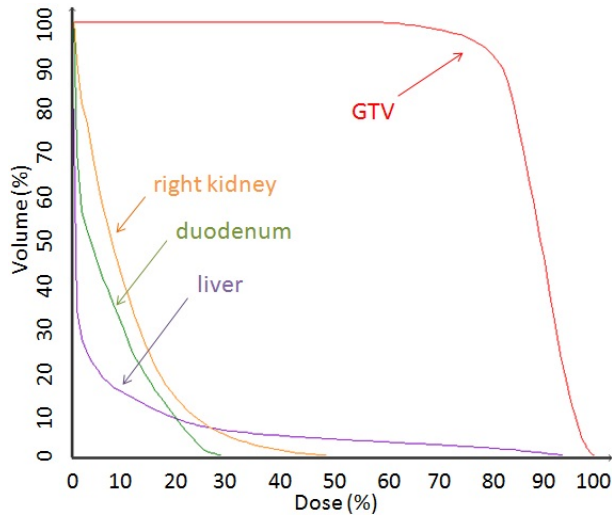
Figure 2.3: Cumulative Dose Volume Histogram

The dose distribution in an organ at risk (OAR) is usually inhomogeneous, some areas receiving more dose than others. The dose tolerance of OARs depends on the dose distribution and the functional architecture of the organ.

– For serial organs: a high dose applied on a small volume is toxic. The dose tolerance is represented by the maximum dose, i.e. the maximum dose delivered to the organ must be at any point less than or equal to the maximum dose.

– For organs in parallel: the dose tolerance depends on the dose distribution within the organ. The dose tolerance is expressed as follows:
Vx $\leq$ Y%, which means that the X Gy dose should not be delivered in more than Y% of volume of the OAR.

DVH as well as TCP and NTCP are very useful for graphical evaluation of tumor control and normal tissue damage, and can be used for guiding

the treatment planning.The DVH may be useful to evaluate the quality of a treatment plan and is used during the optimization process.

2.2   CyberKnife System

2.2.1   SBRT CyberKnife System

The CyberKnife® radiation therapy system (Accuray Incorporated, Sunnyvale, CA) is a Stereotactic Body Radiation Therapy (SBRT) system that uses intelligent robotics to treat tumors with millimetric precision. The Cyberknife can be considered as a radiosurgery device because it is a treatment procedure similar to stereotactic radiosurgery for central nervous system, i.e. a high dose delivery in few fractions. It has an unlimited scope to treat a wide range of tumors anywhere in the body, including the prostate, lung, brain, spine, liver, pancreas and kidneys.

Figure 2.4: CyberKnife System

The combination of imaging guidance technology and computer-assisted robotics can detect, track and correct displacements of the tumor and patient movement throughout the treatment. It allows a significant escalation of the dose to the tumor target with high precision, by lesion tracking throughout the respiratory cycle. This is especially relevant when treating lesions that undergo movements correlated to the respiration of the patients (e.g. lung, liver).

The CyberKnife system is equipped with a **compact linear accelerator**, that delivers a 6 MV photon beam. The accelerator part is comparable to standard linear accelerators. Radiation beams are precisely shaped with either fixed **collimators** or the Iris variable aperture collimator.

Twelve fixed collimators deliver circular field sizes from 5 to 60 mm diameter. The Iris collimator replicates the existing 12 fixed collimator sizes. The Iris collimator creates and shapes beams with characteristics virtually identical to those of the fixed collimators. It consists of two banks of 6 tungsten segments each creating a hexagonal aperture. The two are offset resulting in a dodecahedral (12-sided) aperture. [38]

The accelerator is mounted on a **robotic arm** with six axes of motion, designed to move and manage the accelerating portion with high precision and repeatability, providing irradiation in all directions. The flexibility of the system and its faculty to multiply radiation paths help to minimize the risk of irradiation of healthy cells around the tumor (Figure 2.5). The **RoboCouch** treatment couch has six degrees of motion ensuring precise and rapid patient positioning.

Some types of stereotactic radiosurgery require a stereotactic frame screwed into the patient skull to minimize the movements. This is not the case with the CyberKnife system which is equipped with an **imaging guidance system** that allows continuously adjusting while patient or tumor are moving.

This sophisticated monitoring system also allows 4D treatments, i.e. to irradiate tumors that move with respiration in real time. The target is detected and followed in real time without irradiation interruption. There are two available modes of 4D treatment on the CyberKnife; The Xsight
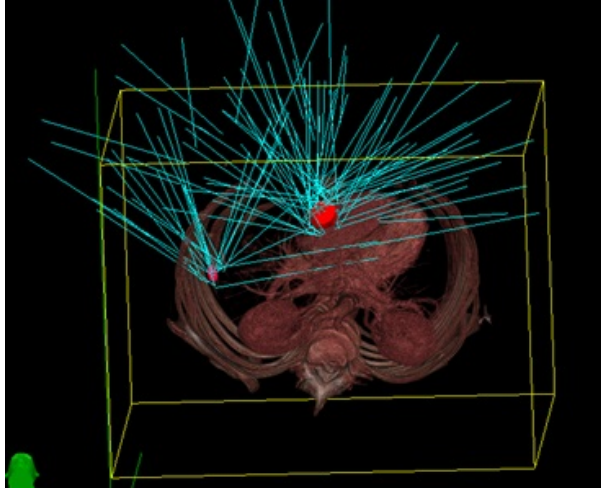
Figure 2.5: Illustration of the CyberKnife System treatment beam geometry –
multiple beam paths for two targets (in red)

Lung Tracking System that uses the image contrast of the lung tumor to
target beams, and the Synchrony™ Respiratory Tracking System, dedi-
cated to abdominal cancers treatment, which requires the use of radio-
graphic fiducial markers implanted near the tumor.

High doses delivered with high accuracy allow hypofractionated treat-
ments. The CyberKnife provides a non-surgical option for patients who
have inoperable or surgically complex tumors, or who search an alter-
native to surgery. The CyberKnife has some disadvantages such as the
need to graft radiographic trackers and sometimes long treatment time,
particularly for liver treatment. Moreover, no irradiation is possible from
below the table and no cone beam CT is available for patient positioning
and target tracking.

2.2.2   Respiratory Tracking - Synchrony System

Breathing is an important source of uncertainties in external radiother-
apy, especially for tumors in the abdominal regions, such as the liver.
With conventional radiotherapy, tumor movements obligate to apply a
larger margin from the Clinical Target Volume (CTV) to define an In-

ternal target Volume (ITV) using 4D CT information. The Synchrony Respiratory Tracking System (SRTS), available on the CyberKnife, enables real-time adjustments with changes in the tumor position during the treatment delivery. It continuously synchronizes treatment beam delivery to the motion of a target, that allows a margins reduction.

Several internal markers are percutaneously implanted under image guidance (ultrasound or fluoroscopy) in the liver and light-emitting diodes (LEDs) are placed on the patient abdomen (Figure 2.6). Cylindrical gold seeds are often used, with dimensions of 0.8–1.2 mm in diameter and 3–6 mm in length. The radiopaque markers, called fiducials, are placed around the lesion being treated to provide an internal frame of reference. The implantation directly in the tumor is avoided due to the potential cancer cells spreading.

(a)   (b)
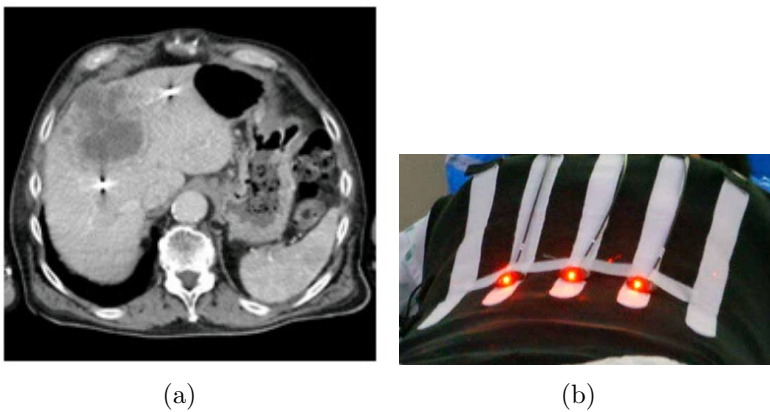
Figure 2.6: CT slice with fiducials implanted in liver (a) and infrared diodes on patient abdomen (b)

A correlation model between the fiducials center of mass location and the respiratory movement amplitude is build using infrared camera signal for real-time breathing pattern monitoring (Figure 2.7(b)) and X-rays imaging to visualize the fiducials (Figure 2.7(a)).
There is a separate correlation model for each external marker. Each model provides an estimate of the fiducials COM, and these individual estimates are averaged to get the final position estimate.
It is possible to deactivate an external marker or to not consider an in-

ternal marker during treatment, when the correlation model is poor.

The correlation model is checked and updated regularly by acquiring additional X-ray images. In fact, the model is based on the latest 15 sets of X-ray images taken and is updated every time a new image is taken, i.e. each 80 seconds, with the oldest image being discarded. The allowable error in the correlation model can be modified by the user and the violation of these set limits causes a pause in the treatment delivery. [38] A new correlation model is build before continuing treatment.
The system automatically determines the best correlation model type to be used for the particular treatment by choosing the model type that minimizes overall correlation error. The model is chosen from linear, curvilinear and bi-curvilinear forms.
Real-time adjustments during treatment delivery are based on the correlation model, and a prediction algorithm overcomes the communication latencies and the robotic manipulator inertia causing delays (up to 115 ms).

(a)   (b)
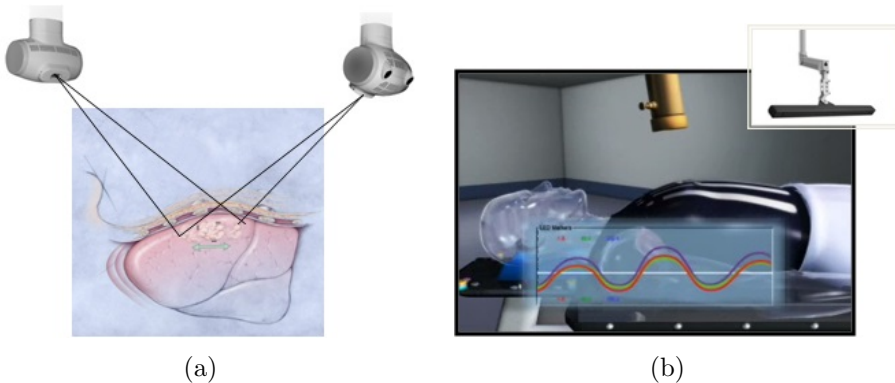
Figure 2.7: x-rays imaging (a) and building of correlation model (b)

A detailed review of studies of geometric accuracy reports a wide range of experiments involving phantom tests and patient data. [39] The total system error of treatment planning and delivery has been defined from test methods with a phantom which moves continuously during treatment to simulate respiratory motion. The phantom-based accuracy measurements with respiratory motion report a total system error below 0.6 mm.
Clinical data-based accuracy measurements with respiratory motion have

been performed by retrospective analysis of treatment data. The correlation model error, which is the distance between the model-based predicted and image-based actual positions, is a measure of the accuracy of Synchrony tracking. In a study in which a linear correlation model was used for all cases [40], the average of 510 correlation error values was 1.4 ± 1.0 mm (mean $\pm$ SD). A more recent study [41] places an upper limit on the correlation and prediction model errors with inclusion of standard features.

2.3   Magnetic Resonance Imaging

The Magnetic Resonance Imaging (MRI) is a technique used in radiology to investigate the anatomy and function of the body without exposure to ionizing radiation.
The physical phenomenon was conceptualized in 1946 by Bloch and Purcell [42] and the first images in humans were produced in 1979. Today, The technique is widely used for medical diagnosis, staging of disease and for follow-up.
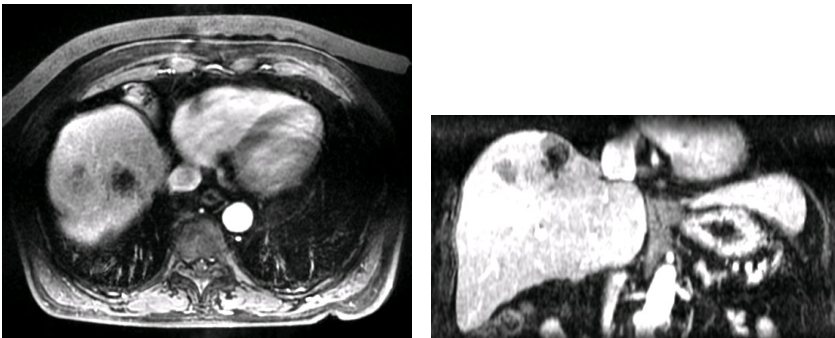
Figure 2.8: MRI images in transverse plane (left) and coronal plane (right)

MRI is a technique based on the observation of the physical phenomenon of nuclear magnetic resonance of water protons contained in the body, i.e. the response of nuclei subject to an external magnetic field and an electromagnetic excitation. The signal intensity collected in a volume element (voxel) depends on the concentration of water and the relaxation time of nuclear spins of protons (describing the return to equilibrium nuclei after

excitation). The signal differs according to the nature of the tissue (bone, fat and other soft tissues). This provides a three dimensional image of the patient and allows observing tissue alteration (such as tumors) (2.8).
The excitation of protons is performed in successive series of radiofrequence (RF) pulses called "sequences". Depending on the intensity, duration and series of RF waves emitted in the sequences, the image contrast will facilitate visualization of specific areas. MRI examination consists of several sequences, that allow seeing the organs in several spatial planes and with different tissue contrasts. Information on structure and metabolism of organs can be investigated by MRI imaging. This allows anatomical and functional imaging.

This imaging technique is made possible because water constitutes about 80% of the human body. However, the signal intensity is sometimes insufficient to observe a suitable difference between healthy and diseased parts of the body. The contrast between two voxels can be increased using a contrast product to influence the signal.

Focal or diffuse disorders of the liver may be evaluated using diffusion-weighted, opposed-phase imaging and dynamic contrast enhancement sequences. Gadolinium-enhanced MRI (Gd-MRI) is a sequence used especially for the detection of small hepatic metastases [43]. Diffusion-Weighted Imaging (DWI) is another sequence frequently used in abdominal imaging particularly for assessment of liver [44]. DWI alone can be used in patients where gadolinium contrast administration is not allowed, but the combination of Gd-MRI and DWI significantly increases diagnostic accuracy [45]

MRI offers abundant biological and pathological information concerning T1 and T2 relaxation times, fat deposition, hemorrhage, metal deposition, perfusion, bulk flow, proton diffusion, and susceptibility, whereas CT offers information on X-ray attenuation and blood flow alone.[46]
MRI can be used in addition or as an alternative to CT imaging if CT cannot be realized.

2.4 4D PET-CT modality

2.4.1 PET imaging

Positron Emission Tomography (PET) is a functional modality of medical imaging that allows measuring the tridimensional metabolic activity of an organ.

PET requires the injection of a radioactive tracer. The most common marker is the 18-Fluorine (^{18}F) radio isotope incorporated into a glucose molecule forming fluorodeoxyglucose (^{18}F-FDG) [47]. ^{18}F-Choline is also a tracer especially used for imaging of hepatocellular and prostate carcinoma [48] [49]. The radioactive isotope ^{18}F has a decay half-life of 110 minutes. The transformation decay of a proton into a neutron leads to emission of a positron β^+ and a neutrino (Equation 2.3).

$$p \to n + \beta^+ + \nu_e \qquad (2.3)$$

After being emitted, the positron loses all its kinetic energy travelling a short distance throughout the tissues, on the order of a millimeter, then it interacts with an electron of the environment by an annihilation interaction. In the course of the annihilation, both particle masses are converted into two gamma photons emitted in opposite directions ($\sim 180°$ $\pm 0.5°$) with an energy of 511 keV (Fig.2.9).
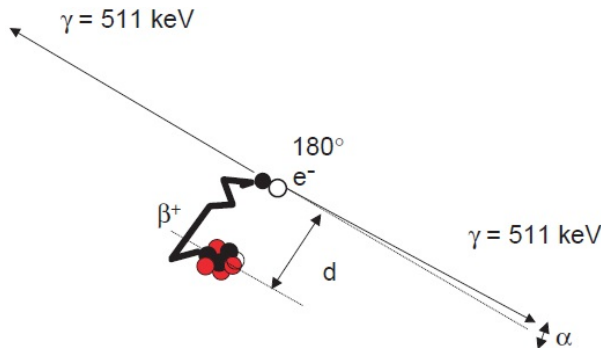
Figure 2.9: Positron emitting and annihilation reaction [4]

The PET consists of the simultaneous detection of both photons to determine the annihilation location. The measured information corresponds to the annihilation location and not to the positron emitting location. The d distance between these two locations, named mean free path of the positron,is determined by the positron emitting energy. The mean free path in water is 0.6 mm for ^{18}F [4].

Most PET systems consist of a series of detector elements distributed in a ring around the patient. Each detector comprises a scintillation crystal and a photomultiplier, optimized for the detection of the gamma photons. The electronic circuit, or coincidence circuit, allows the projection of the annihilation point by means of two elementary detectors. It is based on two criteria: a time window, on the order of 6 to 15 ns, and an energy window. All of the coincidence events detected by the electronic circuit are recorded by the PET computer system and positioned in a matrix. The obtained sinogram contains all the projection elements of object slices.
A computer system reconstructs the images of the tracer distribution as a 3D object, using a tomographic reconstruction algorithm. The spatial resolution of the resulting images is between 4 and 7 mm in clinical imaging.

While traveling throughout the body, many gamma photons undergo attenuation depending on density and thickness of the medium. It is possible to improve image quality by using an attenuation correction. To perform this correction, transmission images obtained by a radioactive source that rotates quickly around the patient was initially used. Nowadays, most PET cameras are coupled to an X-ray CT to obtain a combined PET-CT system.

2.4.2   Combined PET-CT

The PET-CT combines a CT with a PET imaging system in the same gantry, with a patient couch which traverses the bore of both imaging components. The PET-CT system is a practical and effective approach for acquiring co-registered anatomical and functional images in a single scanning session [50].

Combined PET-CT examination starts with the acquisition of an X-ray

overview scan of the patient used to define the axial examination range of the PET-CT study. Then the CT images are acquired. The attenuation correction is based on these CT images, which allows decreasing the examination duration and obtaining a better PET image quality. After completion of the scan, the patient is placed into the PET field of view for the emission scan, by a translation movement of the table [51].

The two acquisition modalities are performed during the same examination without moving the patient using the common coordinates system. This combined imaging system overcomes the registration methods between the two complementary modalities, and the CT adds information regarding anatomic localization to the functional imaging.

(a) CT   (b) PET-CT fusion   (c) PET
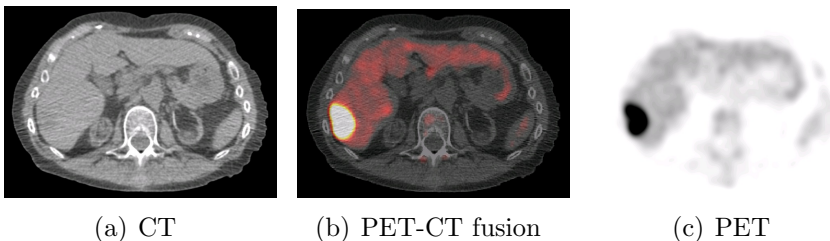
Figure 2.10: CT and PET images from a PET-CT combined device

2.4.3   4D PET-CT

To observe the internal movement during breathing, it is necessary to synchronize image acquisition with the recorded breathing signal; this is the 4D imaging. Images are acquired throughout several respiratory cycles. The collected data are then sorted, or by amplitude or by temporal phase, which are a representation of different configurations depending on the moment of the respiratory cycle. Both exams are divided in the same way enabling the attenuation correction by phase.

Several external devices are used to measure the respiratory signal, such as belt pressure, temperature sensor, spirometer and the Varian Real-time Position Management system (RPM) (Varian Medical Systems, Palo Alto, CA). A physical quantity is measured and correlated to the respiratory motion in all these different devices.

Figure 2.11: Patient examination with the Real-Time Position Management System
(RPM) - infrared camera and reflective box

The RPM™ system is a video based system that measures the motion
amplitude of the patient chest. An infrared camera tracks a block with
reflective markers, placed on the patient chest or abdomen, to measure
the movements in the antero-posterior (AP) direction. Images are contin-
uously collected during several entire respiratory cycles with the patient
breathing freely. The respiratory cycle signal is virtually divided in several
sections, and the 4D images are sorted relative to the cycle time or am-
plitude during acquisition. Each 3D volume is reconstructed by binning
images using temporal phase-based (2.12) or amplitude-based sorting.
4D CT and 4D PET images obtained are directly superimposed thanks
to the unique coordinate system, but the two image sets are not perfectly
consistent. The CT images are acquired during a shorter time than the
PET images which causes some differences in information provides by the
two modalities.

The 4D PET-CT allows capturing anatomical and functional images dur-
ing different times of the respiratory cycle to determine the breathing
impact on the tumor motion.
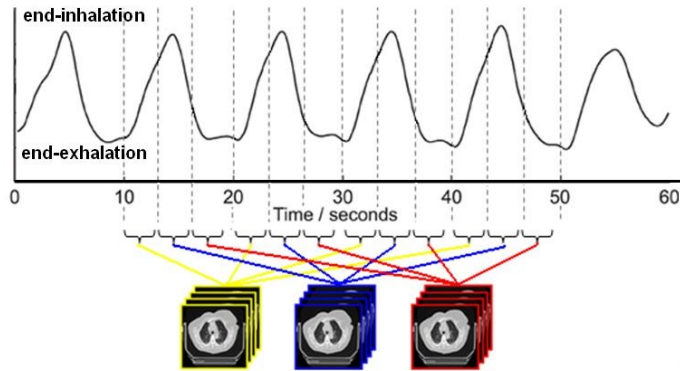
Figure 2.12: Example of temporal phase-based sorting of 4D images acquisition (3 distinguished respiratory phases)

2.5 Monte-Carlo Simulation

2.5.1 Double calculation

The calculation of monitor units by an independent system is a mandatory requirement to receive authorization for care by an external radiotherapy modality. Double calculation of monitor units is not intended to provide the value to use for the treatment of patients but a tool for quality assurance. This is to ensure that the value obtained from the treatment planning system (TPS) is consistent with the prescription and the beam parameters used for treatment. It is necessary to set a leeway which is typically around 3-5%. When this margin is exceeded, it is necessary to look where the differences stem from and to verify if they can explain the magnitude of the observed discrepancy. That allows to choose the number of monitor units that seems best adapted, taking into account limits inherent to the algorithms used in TPS and the independent system. Exceptionally and carefully documented, it is permissible to manually correct the values calculated by one of the systems, to account for approximations used by the algorithms. [52]

Several commercial software systems are available, such as IMSure QA Software (Standard Imaging Company), but many centers have developed internal solutions based on the use of home-made software. Monte Carlo calculation is a solid basis for double calculation software development.

2.5.2   Monte Carlo algorithms for dosimetry

Monte Carlo (MC) is an approach to simulate particles transport in materials. MC dose calculations simulate individual photon and electron tracks through the accelerator treatment head, the collimator and the patient. Along its track, a particle may interact with the medium through which it passes. Using a random number generator and cross section data for the different types of interactions, the program samples the distance to the next interaction for a particle at a given position and with a given speed in a given direction. After propagating the particle to the interaction location, the type of interaction that will take place is sampled. For each simulated interaction, the difference in energy between the incoming and outgoing particle(s) is calculated. The total dose can be calculated by adding the contributions from all interactions taking place within a patient voxel and taking into account the voxels mass.[53]

2.5.3   The EGSnrc code

Monte Carlo methods are often considered the standard for simulated measurements of photon and electron transport for many biomedical applications. Four general purpose Monte Carlo systems are being used in applications for radiotherapy dose calculation. These systems are EGS ([54], [55]), MCNP ([56], [57]), PENELOPE ([58]), and GEANT ([59]). EGS and PENELOPE simulate the coupled transport of photons and electrons (and positrons) that are the particles of interest for radiotherapy dose planning, while other particles such as neutrons or protons are not taken into account. In high energy photon beams (18 MV and higher) the production of neutrons and protons in the accelerator head may impact the physical dose distribution in the patient, especially in bone where even alpha particles have a non-negligible contribution ([60]). These particles can be taken into account in MCNP and GEANT.
Generally, photon transport modeling is quite similar in all four systems in the energy range of radiotherapy applications, although different cross section data are used. The main differences are encountered in the electron transport, which strongly influences the speed and accuracy of the codes.[61]

Much attention has been paid to the electron transport in EGS (Electron-

Gamma Shower). The current EGSnrc code was released in 2000 as the successor to EGS4. An improved multiple scattering theory was implemented, and the electron step length is reduced by the replacement of the parameter reduced electron stepping algorithm (PRESTA) by PRESTAII ([62]) which introduces a single scattering model of electron transport. These adaptations improved the calculation accuracy of angular deflections for electrons, eliminated restriction on the maximum and minimum electron path length, and provided an exact boundary-crossing algorithm by using single elastic collisions of electrons. The EGSnrc code has been extensively benchmarked and is widely used. Individual user codes can be created in a macro Fortran code, called MORTRAN, and connected to the EGSnrc core in a pre-compilation step.

2.5.4 Linear acceleration modeling using BEAMnrc

Accurate patient dose calculations can only be performed when the treatment beams are accurately modeled. BEAMnrc is an EGSnrc user code dedicated to the 3D simulation of RT treatment units [63] and developed for the modeling of a linear accelerator. Each linear accelerator used for external photon beam RT essentially has a modular construction. The technical specifications of the components differ from one manufacturer to another. All component types (target, primary collimator, flattening filter, monitor, jaws, multi leaf collimator (MLC), etc.) are pre-programmed in BEAMnrc as component modules (CMs). Users can build their own accelerator model by selecting the required CMs. The dimensions, materials and transport parameters of each CM have to be defined in an input file but no programming efforts are required. BEAMnrc can be used to determine so-called phase-space files in a scoring plane at the end of a CM, e.g. at the exit of the linear accelerator treatment head. A phase-space file contains all necessary parameters (location, direction, energy, charge etc.) of particles passing through the plane.[61]
Phase-space files can be used as input for dose calculations within a patient or a phantom.

2.5.5 Dose calculation using DOSXYZnrc

DOSXYZnrc is an EGSnrc user code dedicated to the calculation of dose distributions within a phantom consisting of rectangular voxels [64]. Dif-

ferent source types can be selected, including individual beams and full phase-space files generated by a BEAMnrc simulation. A specific material composition and mass density value can be assigned to each voxel, in which the energy deposition is scored. Voxel dimensions are independently variable in all 3 directions. The stand-alone program CTCREATE was developed to convert a CT data set into the appropriate voxel geometry for DOSXYZnrc. Material and mass density data are derived from the Hounsfield number within each voxel. Several CT data set formats are supported, including DICOM.[61] [53]

2.5.6   Monte Carlo dose calculation accuracy

As MC algorithms simulate stochastic processes, statistical uncertainties are inherently associated with the results. This statistical noise decreases with the square root of the calculation time, but is independent of the number of simulated beams. Beyond that, other factors mainly determine the degree of accuracy that can be achieved with MC calculations.
Among them, how accurately the treatment beams are modeled with respect to energy and directional distribution and how accurately the patient geometry and tissue properties relevant to the radiation interactions are modeled. The accuracy of the cross section data used to simulate the various interactions between ionizing radiation and matter is also a main factor determining the calculation accuracy.
Full Monte Carlo algorithms are considered the most accurate dose calculation algorithms as they directly account for tissue heterogeneities. Additionally, scatter and leakage effects are directly taken into account by transportation of individual particles through the MLC.[53]

2.5.7   Monte Carlo System Software

2.5.7.1   Monte Carlo System structure

The Monte Carlo System (MCS) software, which supports some studies of this thesis, is based on the EGSnrc system. BEAMnrc is used to model the treatment linac head of the CyberKnife at Oscar Lambret Center in detail. The geometry and materials were introduced based on the specifications provided by the manufacturer. Figure 2.13 shows a schematic drawing of the treatment head of the CyberKnife installed at Oscar Lambret Center

[5].
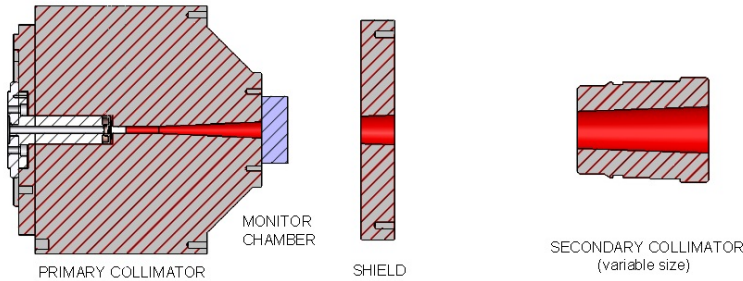
Figure 2.13: The CyberKnife geometry as defined in the BEAMnrc simulations [5]

The phase-space files at the exit of the linear accelerator treatment head can be calculated for each of the 12 fixed collimators and for the IRIS for all aperture sizes available. Once calculated, these phase-space files can be used directly as input for DOSXYZnrc for the calculation of dose distributions within any phantom.

Several MC systems can be used in the MCS software, such as GEANT4 that allows proton MC calculation.

2.5.7.2 Monte Carlo System functionality

MCS can be used as double calculation for the different devices available at Oscar Lambret Center, for quality assurance. Within the scope of this thesis, MCS is specifically used for dose calculation with the CyberKnife system for liver lesion treatment.

The MCS software allows dose distribution calculation from patient or phantom datasets and plan characteristics. The plan characteristics and the dose distribution are respectively an XML object and a DICOM object (RTDose) . Dose volume output can be imported in MCS for dose distributions comparison between two plans.

A graphical user interface (GUI) allows to run the calculations and to visualize the results, displaying dose distributions and dose volume histograms (DVHs). The DVH values can be exported to a spreadsheet application such as Excel (Microsoft) for analysis.

couleur	nom	moy (Gy)		max (Gy)		volume (%)		dose (Gy)	
☐	coeur	4.2	5.7	29.7	35.2	100	100	0.0	0.0
☑	colon	7.8	6.6	44.9	39.6	100	100	0.0	0.0
☐	CTV	47.2	46.9	53.2	53.7	100	100	42.0	39.0
☑	duodenum	2.8	1.9	8.6	6.9	100	100	0.0	0.0
☐	estomac	5.6	5.2	14.8	14.0	100	100	1.0	0.0
☐	External	4.8	4.6	50.9	52.8	100	100	0.0	0.0
☐	foie	17.0	14.1	51.7	53.7	100	100	0.0	0.0
☑	foie sain	13.0	9.8	49.1	45.5	100	100	0.0	0.0
☑	GTV	47.0	48.1	53.0	54.5	100	90	42.0	45.0
☐	moelle	4.2	4.3	10.3	10.4	100	100	0.0	0.0
☑	oesophage	2.7	3.7	7.6	12.3	100	100	1.0	1.0
☑	poumon d	7.5	11.0	50.3	52.4	100	100	0.0	0.0
☐	poumon g	1.4	1.7	7.8	9.5	100	100	0.0	0.0
☑	PTV	46.4	45.7	52.9	53.9	95	95	42.0	36.0

Figure 2.14: Window of visualization of MCS

2.6 Deformable Image Registration algorithms

The registration consists in the mapping of images, by searching a geometric transformation allowing passing from one image to another. The image registration can be single-modality, when images come from the same modality, as CT-CT or MRI-MRI, or multi-modality, such as on the Figure 2.15.
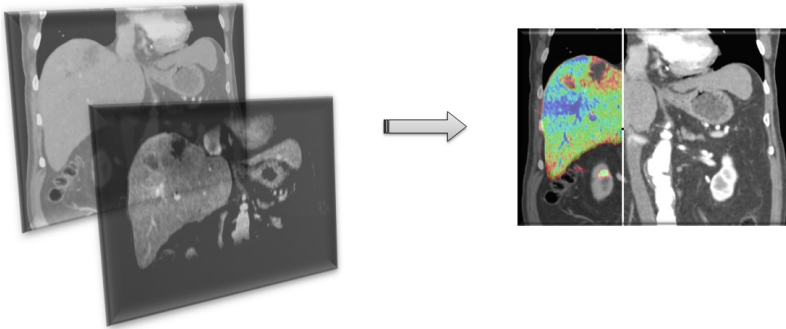
Figure 2.15: Multi-modality image registration (CT and MR images)

2.6.1 Principle of Registration

The principle of registration consists of the estimation of a transformation field allowing the deformed image to be as close as possible to the reference image. Four criteria define the components of a registration method [65] [66] :

– primitives: these are the relevant informations extracted from the images, which can guide the registration. We distinguish extrinsic primitives (e.g. external markers attached to the patient) and the intrinsic primitives, corresponding to information from the image (e.g. gray levels).

– the similarity criterion : defines a "distance " between the attributes, allowing the quantification of the proximity or the similarity between both images.

- deformation model : determines how the image is geometrically modified.

- optimization strategy : the method used to determine the best transformation in the sense of a similarity criterion in the search space defined by the deformation model

Preliminarily, the primitives must be extracted from the two images to be registered. Then, the similarity criterion, theoretically minimum (or maximum) when the two images correspond perfectly, is defined. The deformation model is chosen and the calculation is performed, then the optimization estimates the optimal transformation that minimizes (or maximizes) the criterion to ensure the best mapping between the two images. Equation 2.4 is a general mathematical formulation of a transformation calculation :

$$T = arg\ max\ \{S(I, J, T)\} \tag{2.4}$$

In the equation 2.4, the "arg max" designates the optimisation algorithm and the "S(I,J,T)" the similarity measurement between both images I and J. T represents the calculated transformation.

The choice of the approaches to guide the registration is widely conditioned by the nature of images. We distinguish two principal: The geometric approach and the iconic approach. The first consist in the extraction and the matching of subsets of homologue points, the second uses the intensity information in each pixel of the images.
The choice of the similarity criterion depends on the modality of the images to be registered. Cross-correlation, mutual information, sum of squared intensity differences, and ratio image uniformity are commonly used.

2.6.1.1   Rigid Registration

The rigid transformation involves estimating translations and rotations to reposition a rigid object. This type of transformation preserves distances, angles and parallelism. The number of degrees of freedom is 3 for 2D

and 6 for 3D. This model is primarily used to reset images of the same individual acquired at different time.

There are other types of linear transformation [67]:

– the metric transformation, which consists in the estimation of an isotropic scale factor in addition to translations and rotations. The number of degrees of freedom is 4 to 2D and 7 to 3D.

– the affine transformation, which allows to consider the scaling factor as anisotropic and to model shear. This model is typically used for inter-individual images registration.

– the projective transformation, used mainly to take into account the effects of perspective in images. This type of transformation is used for registration of 3D images to 2D images.

2.6.1.2   Deformable Registration

As described in chapter 1, the liver is a deformable organ. In the context of the registration of several 3D liver images corresponding to several respiratory phases, it is necessary to apply transformations having many degrees of freedom, able to modify the overall shape of the structures. Such models are called non-rigid models or deformable models.

Deformable registration corresponds to the displacement of each point of an image to match the corresponding point in a second image. For two images I and J, the purpose of deformable registration is to calculate a displacement vector for each point x of the image I. For each point x, corresponding to the origin of the vector in the image I, the motion vector calculated by deformable registration associates a point x', corresponding to the end of the vector in image J. Each point is registered with its own function. The set of motion vectors forms a matrix called deformation vector field or displacement vector field (DVF).

Many different models are used for deformable registration images. They are shown in several groups in Figure 2.16 ([6]).
The Demon's and the Free Form Deformation (FFD) methods are frequently used. The main advantage of FFD lies in their ability to estimate

localized deformations, allowing them to properly understand local variations in shape. [67]
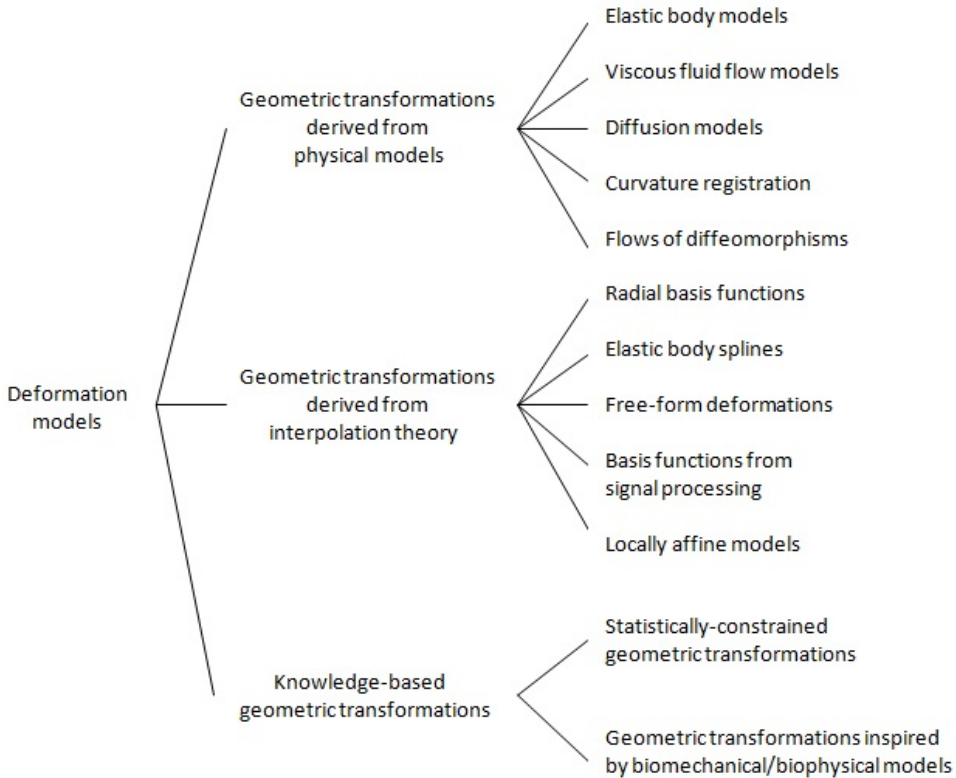
Figure 2.16: Classification of deformation models ([6])

2.6.2 Accuray method for DVF calculation

A team of researcher of Accuray have developed a powerful deformable image registration (DIR) algorithm. The accuray DIR algorithm is a proprietary non-parametric non-rigid image registration method. It assumes no specific parameterization of the transformation; instead it explicitly estimates the deformation field subject to smoothness regularization. Such an approach allows estimating even complex organ deformations. The Accuray DIR optimizes similarity criterion, local Normalized Correlation Coefficient, which allows for robust image matching even in the presence of intensity inhomogeneities and artifacts. The algorithm is implemented

on GPU/CUDA and takes less than 10sec to register two 3D volumes of size 300x300x300. The evaluation of the accuracy of this algorithm is performed in chapter 4.

2.6.3   DIRART method for DVF calculation

An alternative method for DVF calculation was evaluated in order to be more independent from Accuray.

2.6.3.1   Method

The second method of DVF calculation used a MatLab free access program, named DIRART. The DVFs were determined from two 3D images and one deformable image registration algorithm.

The DVF could be defined on the coordinates of the fixed images, it is then called a "pull-back" motion field. Each 3D vector of this DVF is associated with a voxel of the fixed images, and defines the corresponding voxel in the moving image. This DVF defines the coordinate transformation from the fixed image to the moving image.
A DVF that defines how every voxel in the moving image moves, is called a "push-forward" motion field. This DVF is defined on the voxels in the moving image [68]. The "push-forward" motion field calculation is used in our method.

If the two motion fields are not defined on the same coordinate system, they are not necessarily directly negative to each other. We made sure to always work in the same coordinate system to overcome this problem.

The DIRART program is readily usable with a graphical user interface (GUI), displayed on Figure 2.17.
The moving (reference images) and the fixed (target) images were loaded in the GUI. An image cropping was performed in the Max Intensity Projection (MIP) image. The cropped box must contain the area to deform and must be larger on the moving images.
The program requests an image resampling to have the same resolution in both moving and fixed images. The selected resolution was 1 mm in left-right direction (x), 1 mm in anteroposterior direction (y) and 2.5 mm in

craniocaudal direction(z). The image resolution in the z direction can not be inferior to the slice thickness, because it would create information that we do not have in the images. The DVF had the same array dimension and the same 3D resolution as the fixed images.
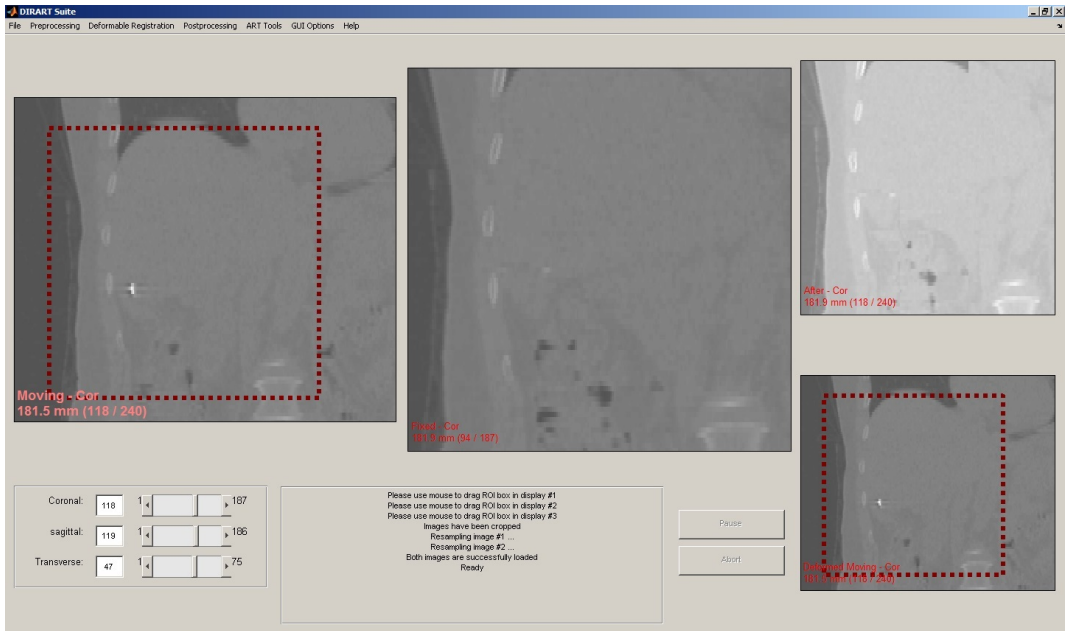
Figure 2.17: Graphical User Interface of DIRART program

(a) moving image   (b) fixed image
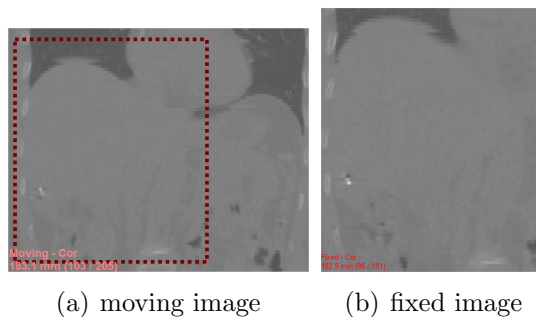
Figure 2.18: Loaded images in DIRART program.
The thick brown dashed box corresponds to the fixed image boundary box

After loading the images, the DIR algorithm was selected, and its parameters were adjusted. The DIRART program offers several algorithms. Some of them will be compared to find the most suitable for our study (refer to section 2.6.3.2).

For each respiratory phase the DVF was determined and saved in MAT-files format.

2.6.3.2   Evaluation of DIRART DIR algorithm

2.6.3.2.a   DIR algorithms comparison

As previously explained, many algorithms using different registration methods are available in DIRART.

Different algorithms may result in different DVFs. This is why it is necessary to determine the impact of the choice of the algorithm. The comparison of the results obtained with several algorithms will allow determining the accuracy of the method, and finding the most appropriate algorithm. The five compared algorithms are: two Optical Flow methods, Original Horn and Schunck (HS) and Iterative Optical Flow (OF), two Demons methods, Original Demons (OD) and Double Force Demons (DFD), and the Free Form Deformation method (FFD).

The choice of the five algorithms has been based partly on advices of the author of the DIRART program, D.Yang [68]. He advocated the Horn and Schunck Optical Flow algorithm and the Original Demons algorithm. Moreover, the results presented by Kadoya et al [69], regarding the evaluation of commercial and public deformable image registration algorithms for thoracic 4D CT images, show that the two most accurate algorithms were Horn and Schunck Optical Flow algorithm and the Demons algorithm confirming the author of DIRART.

Our choice was also based on other criteria, such as the capacity to manage a large number of images, and the calculation time that must be reasonable.

Basics images for comparison

The purpose of the comparison of different algorithms is to find the one that gives the most realistic deformation. The accuracy of the computed

DVF can be measured using landmarks and structures contained in images. The deformed structure should be exactly identical to the real structure contained in the target images when the applied DVF is exact.

This test must be performed on a structure that can be easily delineated. The delineation of the liver is not sufficiently reproducible on the CT images, because of the low density contrast. The test has been realized using the contours of the right kidney, which resembles the liver in density and elasticity but is much easier to delineate [70] [71] [72].
The contouring reproducibility of liver and right kidney has been evaluated. The two organs have been manually delineated five times in a single CT images data set and the structures drawn were compared pairwise. For each pair of structures, the volume difference, the COM location difference and the Dice were calculated. The results are shown in the Table 2.1 for the liver and in the Table 2.2 for the right kidney.

The results are substantially identical for liver and right kidney, especially for the percentage volume difference and the Dice. This is explained in part by the large liver volume, which is about ten times larger than the right kidney. The tests are more sensitive when applied to a smaller volume, such as the kidney. However, the absolute volume difference and COM location difference are lower for the right kidney. We can consider that the reproducibility of the right kidney contouring is better than for the liver. Moreover using the kidney contour is less time consuming, thanks to the smaller cropped box.

All algorithms are applied to the same images to have a reference for the comparison. All obtained DVFs have the same dimensions which are 144*133*135 mm (x*y*z directions), and the same resolution which is 1*1*2.5 mm. The CT scanning resolution is submillimetric in the slice plane and 2.5 mm in craniocaudal direction (z). Ideally, we should have used isotropicaly resampled images. Increasing the z resolution value would invent information in images adding potentially false information that could lead to a bias in the DVF calculation. Therefore we preferred to keep the 2.5 mm scanning resolution in craniocaudal direction.

Number of contours	ΔV (cc)	ΔV (%)	ΔCOM (mm)	Dice
1-2	99	6	2	0.97
1-3	85	6	3	0.97
1-4	84	6	4	0.97
1-5	35	3	4	0.98
2-3	14	1	3	0.98
2-4	15	1	5	0.98
2-5	64	4	4	0.97
3-4	1	0	5	0.99
3-5	50	3	1	0.97
4-5	49	3	5	0.98
mean	**50**	**3**	**4**	**0.98**
liver mean volume = 1526 cc				

Table 2.1: Liver contouring reproducibility
Volume difference (ΔV), COM location difference (ΔCOM) and Dice

Number of contours	ΔV (cc)	ΔV (%)	ΔCOM (mm)	Dice
1-2	11	8	4	0.96
1-3	8	6	1	0.96
1-4	10	7	2	0.96
1-5	7	5	2	0.97
2-3	3	2	4	0.98
2-4	1	1	2	0.98
2-5	4	3	3	0.98
3-4	2	1	2	0.98
3-5	1	1	2	0.98
4-5	3	2	1	0.97
mean	**5**	**3**	**2**	**0.97**
right kidney mean volume = 143 cc				

Table 2.2: Right kidney contouring reproducibility
Volume difference (ΔV), COM location difference (ΔCOM) and Dice coefficient

Algorithms parameters

The first step in the selection of the algorithm is to evaluate the performance of each of the five algorithms independently. For that, the best compromise to obtain a stable result with a sufficient number of iterations

and a reasonable computational time must be determined. Algorithm parameters are adjustable via the parameters panel control (Figure 2.19).
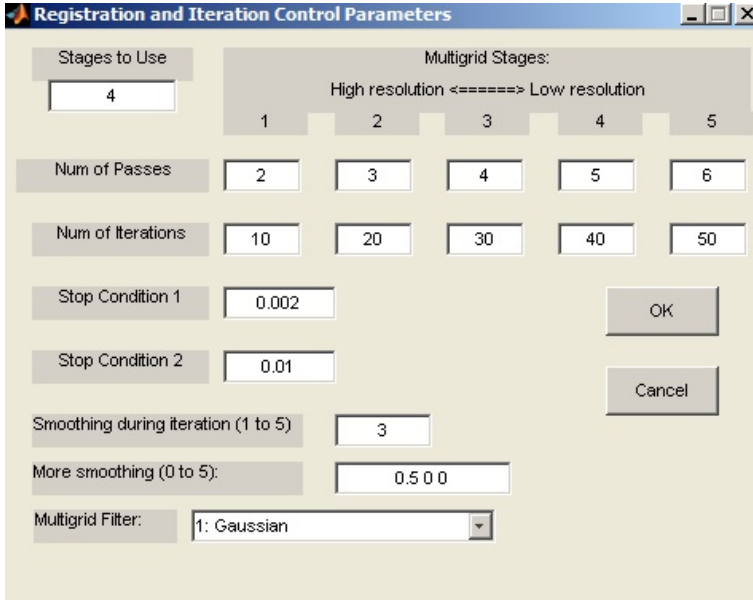
Figure 2.19: Parameters panel control

Several approaches for calculation are possible depending on the algorithm selected. Multigrid and Multipass are approaches to downsample the images, and to perform image registration sequentially from low to high resolution. After registration is finished in one image resolution stage, the result will be used as the initial condition for the next image resolution stage. The approaches support up to 5 stages. All algorithms are calculated with a maximal number of stages.[69].

To define the optimal parameters for each algorithm, it is necessary to evaluate the stability and the accuracy of the DVFs calculated. This was performed using the different tools for DVF assessment.

For each algorithm, the histograms (in the three directions) were calculated for all DVFs obtained with different iteration parameters. The mean DVF values in the three directions stabilize when the iteration number is

sufficient. When the iteration parameters are pushed beyond their limits, the maxima sometimes become senseless because of outliers.

The DVF matrices were applied on the fiducials coordinates and on the right kidney contours of the reference phase. The accuracy of the registration was evaluated by the difference between displaced and target fiducials location and by the overlap measure for the right kidney.

Results - Choice of algorithm

Table 2.3 summarizes the best compromise regarding the number of iterations/calculation time for each algorithm. This Table contains the iteration parameters, the min,mean and max DVF values, and the Dice coefficient for the right kidney.

number of stages	number of passes number of iterations					calculation time	Values of DVF (mm)		
							min	mean	max
Original Horn-Schunck									
5	80	80	120	120	160	1337 s	X=-8.6	X=-1.2	X=4.7
	100	150	150	200	250		Y=-7.8	Y=-0.5	Y=10.8
							Z=-41.8	Z=-6.9	Z=16.1
Iterative Optical Flow									
5	1	1	1	1	1	897 s	X=-5.5	X=-1.6	X=1.0
	200	300	300	400	500		Y=-1.5	Y=1.3	Y=5.7
							Z=-19.4	Z=-5.5	Z=1.8
Original Demons									
5	20	20	30	30	40	2485 s	X=-18.1	X=-0.8	X=10.3
	30	40	40	50	60		Y=-11.6	Y=3.0	Y=16.4
							Z=-100.2	Z=-7.2	Z=165.4
Double Force Demons									
5	1	1	1	1	1	2083 s	X=-8.7	X=-0.7	X=4.7
	400	500	600	700	500		Y=-4.4	Y=1.7	Y=8.7
							Z=-72.3	Z=-6.1	Z=11.4
Free Form Deformation									
5	1	1	1	1	1	522 s	X=-1.4	X=-0.2	X=0.8
	400	500	600	700	500		Y=-1.7	Y=-0.1	Y=2.8
							Z=-11.1	Z=-1.9	Z=2.1

Table 2.3: Best parameters, calculation time and DVF values for each algorithm

In view of our results, we decided to use the "Original Horn and Schunck" algorithm for the DVF calculation.

2.6.3.2.b DVF histogram

The DVF histogram for each direction is displayed in Figure 2.20, for a specific case of chapter 4 (registration of phases #1 and #3 of 4D CT, for target #3). DVF histograms show low displacement values.
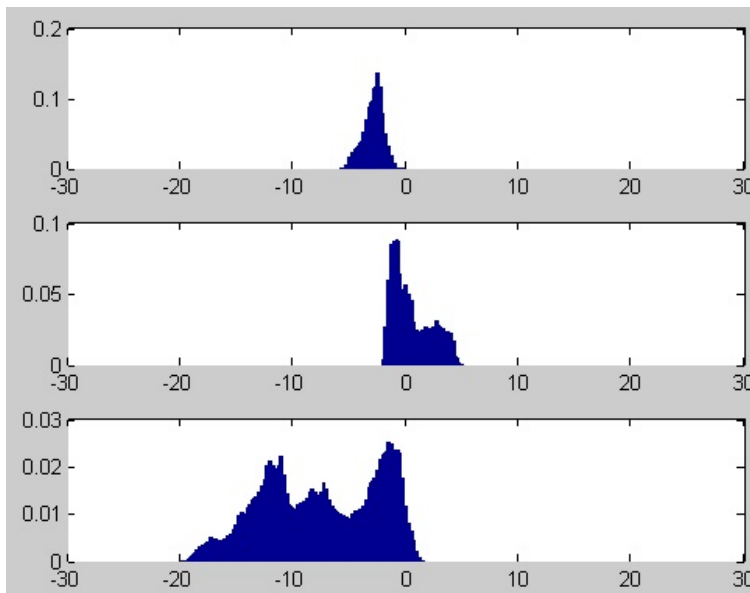
Figure 2.20: DVF histograms (in mm), downward : X,Y and Z component of displacement, for target #3, phases #1 and #3 registered with Optical Flow algorithm (refer to chapter 4)

2.6.3.2.c Fiducials and Structure displacement

The three DVF matrices were applied on the fiducials coordinates. Below, Figure 2.21 represents the fiducials and the fiducials COM location, in reference phase (Ph1), deformed reference phase and target phase (Ph3), for a specific patient of chapter 4 (patient #3).

The fiducials of the registered reference phase and of the target phase should be overlapping exactly. The differences between the fiducials location in Figure 2.21 illustrate that the DIR algorithm is not sufficiently accurate. The calculated displacements are too low relative to the real displacements.
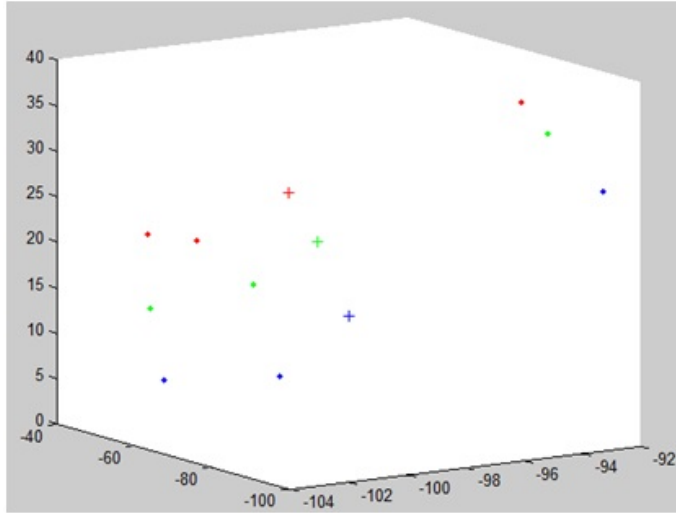
Figure 2.21: Fiducials (points) and fiducials COM (crosses) for patient #3. In blue: reference Ph1 - In green: deformed Ph1 with Original Horn and Schunck algorithm In red: target Ph3 (refer to chapter 4)

The amplitude of fiducial displacement and the differences between displaced and target fiducials location are given by the MatLab function. For patient #3, we obtain the results of Tables 2.4 and 2.5.

	x	y	z
Fiducial #1	-2	-4	8
Fiducial #2	-1	-1	11
Fiducial #3	-1	-1	8
Fiducials COM	**-1**	**-2**	**9**

Table 2.4: Displacement amplitude of fiducials and fiducials COM (in mm), for patient #3 (refer to chapter 4)

In z direction, the real z displacement is underestimated by 5 mm by DIRART. In y direction, the fiducials are slightly displaced while the distance between Ph1 and Ph3 fiducials COM is 6 mm.

The DVFs were applied to the contour points of the kidney for patient #3 (refer to chapter 4). The three subfigures 2.22(a), 2.22(b) and 2.22(c) represent the structure of the reference phase (Ph1), the deformed reference phase (Ph1_def) and the target phase (Ph3), for patient #3 (refer to chapter 4).

The two Figures 2.22(a) and 2.22(b) should be the same if the DVF calculation is accurate, and Figure 2.22(c) should represent two structures overlapping perfectly. Both structures are visually distinct in Figure 2.22(c). These Figures confirm the results observed for the fiducials: the DVF calculation is not accurate enough.

	x	y	z
Fiducial #1	0	10	2
Fiducial #2	-1	6	5
Fiducial #3	1	8	7
Fiducials COM	**0**	**8**	**5**

Table 2.5: Difference between Ph3 fiducial location and Ph1 displaced fiducial location (in mm), for patient #3(refer to chapter 4)

(a) Ph1 (blue) - Ph3 (red)   (b) Ph1 (blue) - Ph1_def (green)

(c) Ph1_def (green) - Ph3 (red)
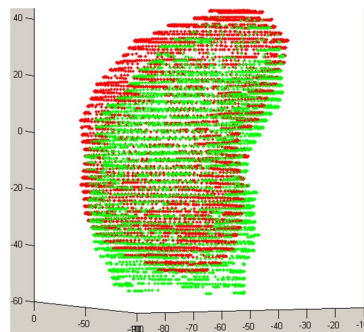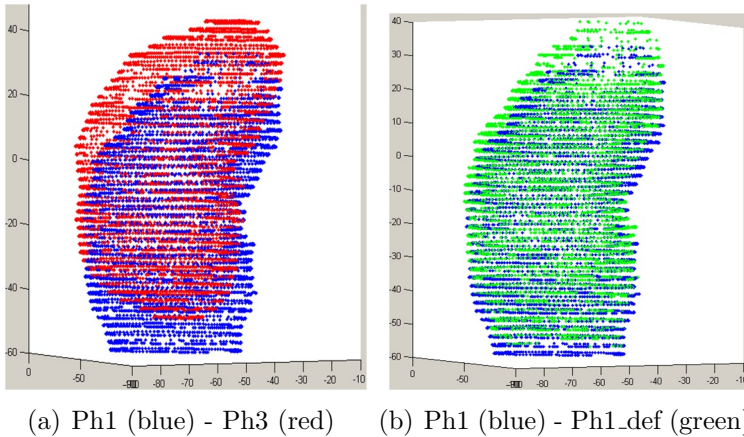
Figure 2.22: Structure of reference phase (Ph1),
deformed reference phase (Ph1_def) and target phase (Ph3)(refer to chapter 4)

Chapter 3

Variability of Target Delineation Using Different Imaging Modalities

3.1   Introduction

Technology in external radiotherapy is constantly evolving. The purpose of this evolution is to improve the treatment while reducing dose delivered to surrounding organs at risk (OARs) along with patient comfort improvement. Persistent inaccuracies during the treatment process provide uncertainty on the final dose actually delivered to the patient.

Uncertainties of various types affect the quality of high energy photon external beam treatment planning. Some uncertainties are related to physical processes, such as the conversion of CT data to electron densities and the weaknesses of the dose calculation algorithm. Other uncertainties are inherent to the treatment machine and combined imaging systems, to the patient positionning, and to the target and OARs delineation.
All uncertainties can potentially have a major impact on the doses to the target volumes and to critical normal tissues which could result in significant alteration of probabilities of tumor control and normal tissue complications [73].

Accurate structure delineation is vital to the success of radiation techniques, because it is the basis of treatment planning. Increasing target contouring accuracy will reduce the overall uncertainty on the delivered dose. It is particularly important for stereotactic radiotherapy by CyberKnife®, which allows delivering precisely a high dose per fraction to the target. It is important to have an accurate definition of the target to not risk treating very precisely, but at the wrong place . . .

The liver lesion and OARs delineation is commonly performed on 3D CT images [74]. The liver lesion is mostly difficult to distinguish because of the low density difference between a hepatic lesion and healthy liver tissue. As often as possible, iodine is used to enhance image contrast for improving the delineation reproducibility.
The interobserver variability in target delineation, which can be attributed to many factors including the influence of the observer (specialty, training, and personal bias) and the impact of the imaging modality [75] should be also decreased using contrast enhancement.

Access to increasingly innovative imaging technology enables continuous

improvement of visualization of lesions. The magnetic resonance imaging (MRI) that allows the acquisition of several imaging sequences with specific characteristics, could be considered for the target delineation. It is well known that MRI offers a better soft tissue contrast than CT. Especially for liver tumours MRI plays a very important role and is often combined with CT for target delineation.

In current chapter, the accuracy (in terms of reproducibility) of target delineation for liver tumors is evaluated both for CT and MRI.

3.2   Methods and Materials

3.2.1   Reproducibility of GTV delineation on CT

3.2.1.1   CT Acquisition

The 3D CT images were acquired with the Aquilion™ LB (Toshiba Medical Co Ltd, Tokyo, Japan). The patients were placed in the supine position with the same contention materials, as used during the treatment delivery. The parameters can be adapted for each patient but they are commonly fixed to 120 kV and 100 mAs for a patient with normal corpulence.
The first part of the examination was performed without contrast product and consisted of a large acquisition in low resolution, to determine the field of view. The second image set was acquired with a smaller field of view and a higher resolution.
In a second time, OptiJECT 350 (Guerbet, France) product containing 350 mg/mL of iodine, was injected in the patient to enhance the image contrast. Several image series were acquired during all phases of the liver transit, including arterial, portal and delayed phases. The CT device locates the time of the first acquisition after injection through the density value of the abdominal aorta, determined from very regular shots. Commonly, the arterial, portal and delayed phases were respectively acquired around 25 seconds, 1 minute and 3 minutes after the beginning of injection.
All 3D CT datasets were acquired in blocked respiration to avoid breathing motion artifacts.
The raw data obtained after acquisitions were reconstructed with a slice thickness of 1 mm for injected images and 3 mm for non-enhanced images.

3.2.1.2 Target delineation on CT images

The target delineation was performed twice on enhanced CT images (portal phase), by a radiation oncologist. The second delineation was performed after a sufficiently long time to ensure that the oncologist is not influenced by a previous visualization of the lesion.
A second radiation oncologist has delineated the GTV on the same enhanced CT images, which allows to compare the target contouring reproducibility between two physicians.

Routinely, CT images are acquired with injection of contrast product, but the contrast product can give problems of renal toxicity and allergic reaction for some patients. The CT acquisition is performed whithout contrast enhancement for these cases. The impact of the contrast product on Gross Tumor Volume (GTV) delineation is studied. The GTV contouring performed on 3D CT images without iodine product injection and on the images of the portal phase, by the same radiation oncologist, were compared. CT acquisitions with and without contrast product have been performed in the same coordinate system during the same examination. No registration is needed between the two image datasets before comparison.

3.2.1.3 Dosimetric Impact of contrast product

The dosimetric impact of the presence of contrast product during CT acquisition was studied by comparison of two dose distributions obtained from the same treatment plan. The one calculated on a CT acquired without injection of contrast product and the other on a CT acquired after injection of contrast product. The study was conducted with the data from ten patients having hepatic lesions and treated with CyberKnife, detailed in Table 3.2.

The applied method consists of several steps. First, the mean Hounsfield Units (HU) of each structure in the CT without contrast product was calculated using PMOD image processing software (PMOD Technologies, Zuirch, Switzerland). The HU values were converted in electronic density using the calibration curve of the Toshiba® CT device. The structures density in the CT with enhanced contrast were manually assigned in the

MultiPlan treatment planning system (TPS), as the mean values of structures density in the CT without contrast product. It is worth noting we did not change the organ densities that were not contoured. It did not seem necessary because these organs fix very little contrast product. Afterward, the dose distribution was calculated for the same treatment plan, on the CT with contrast product with real and changed density values. Finally, the two dose distributions were compared.

3.2.2 Reproducibility of GTV delineation on MRI

3.2.2.1 MRI acquisition

The MRI device used was a Discovery™ MR750 3.0T (GE Healthcare, Waukesha, WI). The patients were in supine position without immobilization materials. Different sequences were acquired in blocked respiration for liver lesion visualization. Images without contrast product are firstly acquired, then a product is injected to the patient to enhance the image contrast. The product can be DOTAREM (Guerbet, France) or MULTI-HANCE (Bracco Imaging, France) and contains 20mL with 0.5 mmol/mL of Gadoteric Acid. The injection was followed by acquisition of several sequences in blocked respiration, such as the T2 enhanced and the Multi ART 20S, which corresponds to 3 acquisition times with 20 seconds between two acquisitions from the arterial time.

3.2.2.2 Target delineation on MR images

A radiation oncologist performed the target delineation twice. The physician has firstly visualized all available sequences and performed the contours alone, on the sequence that provides the optimal target visualization potentially using other sequences. The sequence chosen for the delineation differs from one patient to another.
The best MR sequence to visualize the lesion depends on the patient and the image quality. The different sequences chosen by the radiation oncologist for the nine patients are listed in the Table 3.1.

3.2.2.3 Radiologist support

The interpretation of MR images is a complicated exercise due to the specificities of different sequences. The intervention of a skilled radiologist

No.	MR sequence
1	MULTI ART 20S (2)
2	Axial T2
3	MULTI ART 20S (2)
4	AXIAL T2
5	PORTAL Phase
6	PORTAL Phase
7	AXIAL T2
8	LAVA FLEX WATER
9	AXIAL T2

Table 3.1: List of MR sequences used by the radiation oncologist, for all patients

to assist the radiation oncologist is needed to have an optimal target delineation. The radiologist reviewed the contours previously performed by the radiation oncologist.

3.2.3 Tools for evaluation of delineation reproducibility

Different metrics could be used for the similarity evaluation between two 3D objects. The first metric chosen for this study is the **Dice Similarity Coefficient (DSC)** that quantifies the spatial agreement of a contender- and reference-Volume Of Interest (VOI) according to the whole volume. The DSC can range from zero to one, where zero represents no agreement and one represents perfect agreement between the two volumes. The DSC values are obtained using Equation 3.1, where Cr and Cn are the two structures :

$$DSC = 2 \times \frac{Cn \cap Cr}{Cn + Cr} \tag{3.1}$$

The DSC value represents the overlap rate between two structures but it does not inform on how they overlap. A same DSC value could be obtained between two 3D structures perfectly aligned but with a different absolute volume, as between two 3D structures of the same size but slightly shifted.

Two other metrics, the **Volume Ratio (Rv)** and the **distance between**

the centers of mass (dCOM), have been chosen to distinguish the different possible situations.

The overlap evaluation between 3D volumes previously delineated, was performed using custom software developed in Matlab (Mathworks Inc, Natick, MA). A Graphical User Interface (GUI) was created, allowing users to perform the registration interactively (Figure 3.1).

A registration is required for the comparison of 3D volumes defined on two different sets of images based on different coordinate systems or acquired at two different times. This is the case for the study of the impact of the contrast product on GTV delineation, in which the two image sets were acquired not exactly at the same moment of the respiratory cycle.
In the GUI, several registration methods are available. The first performs a translation of the fiducials COM, based on the fiducial coordinates in the two image sets. The second method includes the fiducial rotation in the calculation of the registration matrix. This method was performed using the Absor function, an already existing tool encoded in Matlab. This tool uses Horn's quaternion-based method for finding the rotation, translation, and optionally also the scaling, that best maps one collection of point coordinates to another in a least squares sense.
The program requests the structure files in DICOM format and the text files containing fiducials coordinates corresponding to the images as input. The functionality is described in detail in Appendix A.
In the study, the visualization of the volumes and calculation of the different comparison metrics were performed using the GUI.

3.2.4   Impact on CTV

The results regarding the reproducibility of GTV delineation need to be put in perspective. In clinical practice a margin of 5 mm is added from GTV to CTV (clinical target). This is (following the ICRU guidelines [76]) partially to take into account uncertainties in GTV delineation and partially to include microscopic spread of tumor cells. The impact of the uncertainty of the delineation reproducibility of the GTV will be decreased considering the CTV.
If one of the GTVs is considered as correct (e.g. GTV2), while the other (GTV1) is the one actually delineated, then one should determine the
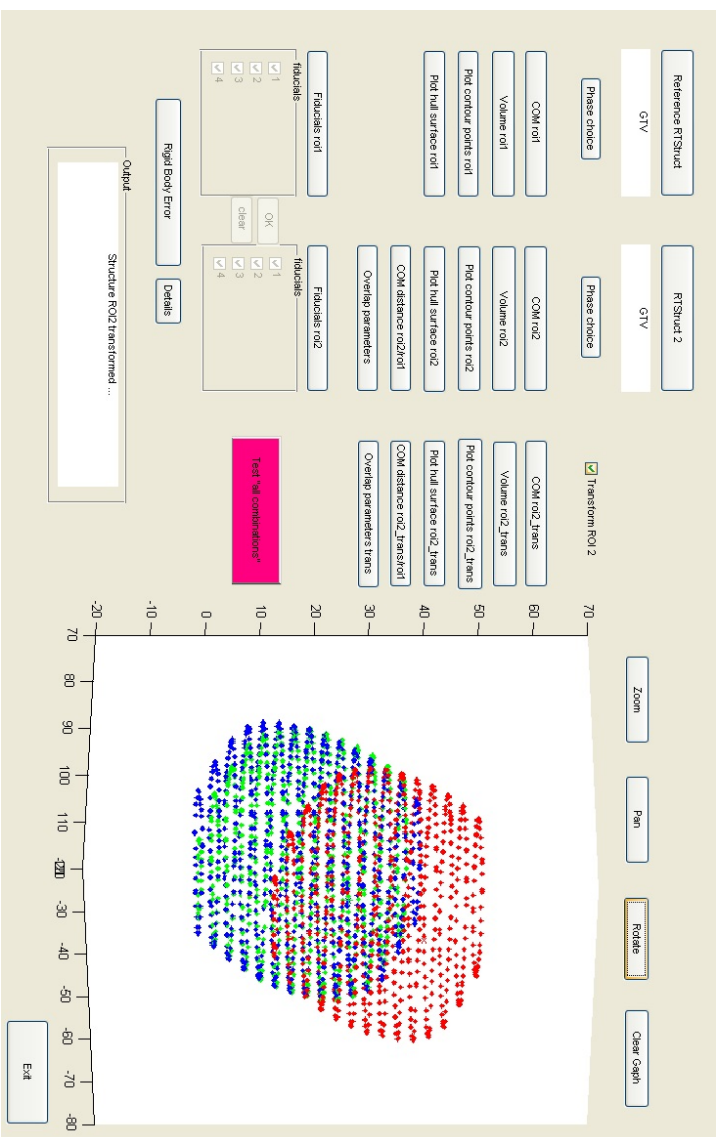
Figure 3.1: Graphical User Interface (GUI) encoded in Matlab. This GUI allows both registering two structures using different registration modes and calculating specific overlap parameters. The green contours are the result of the registration of the red to the blue structure based on the fiducials location. The structures of the CT without and with contrast product correspond to the blue and red contours respectively

overlap between GTV1 plus margin (= CTV1) with GTV2, to have an idea regarding the clinical impact. This was systematically investigated for spherical volumes, determining the intersection geometrically, knowing the radius of the two spheres and the distance between their center of mass. This leads to a general model that can be applied afterwards to the clincal cases, studied in current chapter.

The actual shape of a liver target is not perfectly spherical, but our model provides a good approximation as we are especially interested in a global impact of the applied margins.

3.2.5   Dosimetric Impact of Target Delineation Error

In order to determine the dosimetric impact, a shift of 6 mm in the 3 directions was applied to the GTV to simulate the target delineation uncertainty. The DVH, calculated using the Monte Carlo System software (MCS), allows determining the dose coverage of the shifted GTV when the PTV is targeted.

Only one patient is considered for this test. The applied shift of 6 mm (= global shift of 11 mm) corresponds to the extreme case of the intraphysician contouring uncertainty.

This test was applied with and without CTV.

3.2.5.1   With CTV

In Oscar Lambret Center, a CTV is defined adding a 5mm or 1cm margin from the GTV depending on the pathology (metastasis or HCC). The targeted PTV is defined with a margin of 3mm from the CTV.

The studied case corresponded to a HCC, the GTV-CTV margin was 1cm.

3.2.5.2   Without CTV

In some Centers, no CTV is defined and the PTV is directly determined using a 3mm margin from GTV ([77], [78]). A new plan was performed targeting this new PTV (named PTV_margin).

3.2.6 Patient characteristics

The studies were conducted with the data from patients having hepatic lesion(s) and treated with the CyberKnife (using the respiratory tracking system) with a prescription of 45 Gy delivered in three fractions of 15 Gy, except for one patient (3*12 Gy).

For a group of ten patients, 3D CT images were retrospectively analyzed in order to determine the impact of the contrast product on CT-based delineation and on the dose distribution.
The data sets of nine of these patients were also used for the study regarding the reproducibility of contouring based on CT images. One other patient was included in this study.
For nine different patients, the MR image data sets were analyzed to determine the reproducibility of MR-based contouring.
Patient and tumor characteristics are listed in Tables 3.2, 3.3 and 3.4.

No.	Sex	Age (years)	Tumor location	Tumor size (cc)
1	M	73	HCC SVII	5.9
2	M	73	HCC junction SIV-SVI	73.5
3	M	68	HCC junction SV-SVIII	73.4
4			HCC SIV	3.4
5	M	63	metastasis SI	16.4
6	F	47	metastasis SIII	9.1
7	F	81	metastasis SVIII	9.4
8	F	46	metastasis SV	35.7
9	F	65	metastasis SVIII	67.2
10	F	52	metastasis SVIII	8.2
11	F	83	metastasis SII	21.9
12			metastasis junction SVII-SVIII	74.8

Table 3.2: List of lesion characteristics of patients included in the study of comparison between the delineation based on CT with and without contrast enhancement

No.	Sex	Age (years)	Tumor location	Tumor size (cc)
1	F	47	metastasis SIII	9.1
2	F	81	metastasis SVIII	9.4
3	M	73	HCC junction SIV-SVI	73.5
4	M	67	metastasis junction SIV-SVI	22.0
5	M	63	metastasis SI	16.4
6	F	65	metastasis SVIII	67.2
7	F	52	metastasis SVIII	8.2
8	F	83	metastasis junction SVII-SVIII	74.8
9	M	73	HCC SVII	5.9
10	M	68	HCC junction SV-SVIII	73.4

Table 3.3: List of lesion characteristics of patients included in the study of the reproducibility of delineation based on CT with contrast enhancement

No.	Sex	Age (years)	Tumor location	Tumor size (cc)
1	M	64	HCC SI	176.1
2	M	64	HCC SVII	27.7
3	M	66	HCC SVII	9.2
4	F	79	HCC SVI	182.1
5	M	65	HCC SI	4.1
6	M	61	HCC SII	6.0
7	M	67	HCC SIV	10.4
8			HCC SV	11.4
9	M	66	HCC SV	38.1
10	M	75	HCC SIII	5.9

Table 3.4: List of lesion characteristics of MR images analysed

3.3   Results

3.3.1   Reproducibility of GTV delineation on CT

In this section, all compared contours were delineated on CT series with contrast product. The distance between the COM of the two delineated VOIs and the Dice coefficient are shown in Figures 3.2 and 3.3.
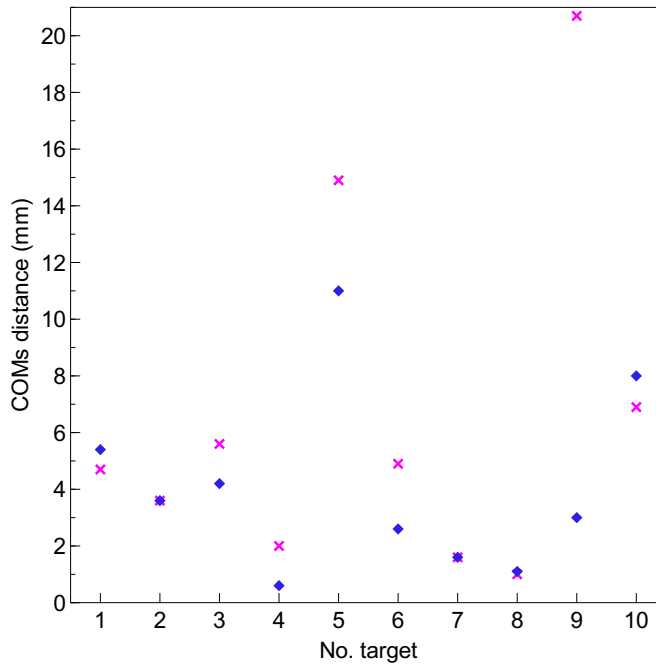
Figure 3.2: Distance between COMs of delineated volumes on CT with contrast product, twice by the same radiation oncologist (blue diamonds) and once by two different radiation oncologists (pink crosses), for all targets

Concerning the reproducibility of target contouring by a radiation oncologist, 80% of the dCOM values are homogeneously scattered between 0.6 and 5.4 mm. Two extremes are observed for targets #5 and #10 with 11.0 and 8.0 mm respectively. The mean value is 4.1 mm and the median value is 3.3 mm.

The two contours present a non-zero overlap for all targets. All Dice

values are between 0.660 and 0.926, except for target #5 for which the Dice is 0.494. The largest dCOM value was also for this target, which is a consistent observation. The mean Dice is 0.749. Four values are superior to 0.8 with three around 0.9.

The mean Rv for all targets is 1.09 with a range from 0.52 to 1.59.
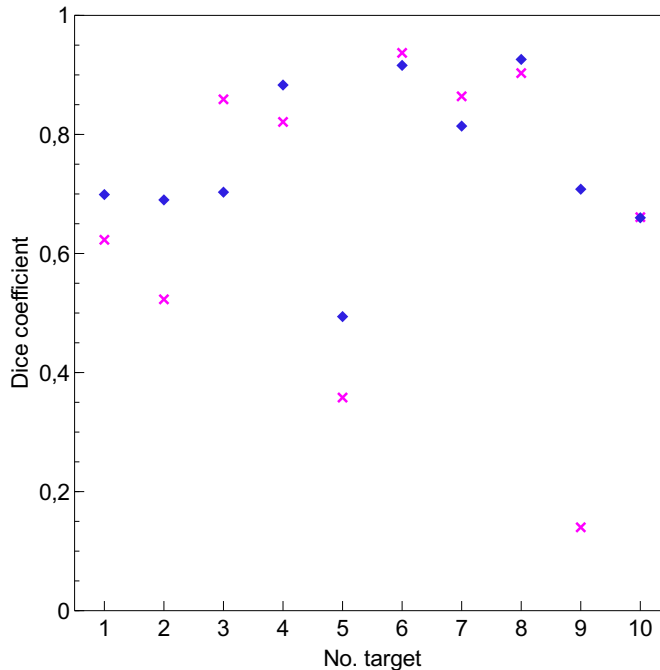
Figure 3.3: Dice coefficient values for delineated volumes on CT with contrast product, twice by the same radiation oncologist (blue diamonds) and once by two radiation oncologists (pink crosses), for all targets

We expected larger dCOM values when comparing delineation performed by two different physicians, but results obtained for the delineation performed twice by the same physician were not systematically better.

Five Dice values are superior to 0.8 but the five others are very low, down to 0.140. The mean Dice is 0.669.

The mean Rv for all targets is 1.20 with a range from 0.57 to 2.73.

The results show large differences between two compared contours for both studies, regarding intra- and interphysician reproducibility.

3.3.1.1   Comparison CT with/without contrast enhancement

The target volumes delineated on CT with and without contrast enhancement product are compared. Figures 3.4 and 3.5 respectively show the distance between the COMs of the two volumes of interest and the Dice coefficients measured.
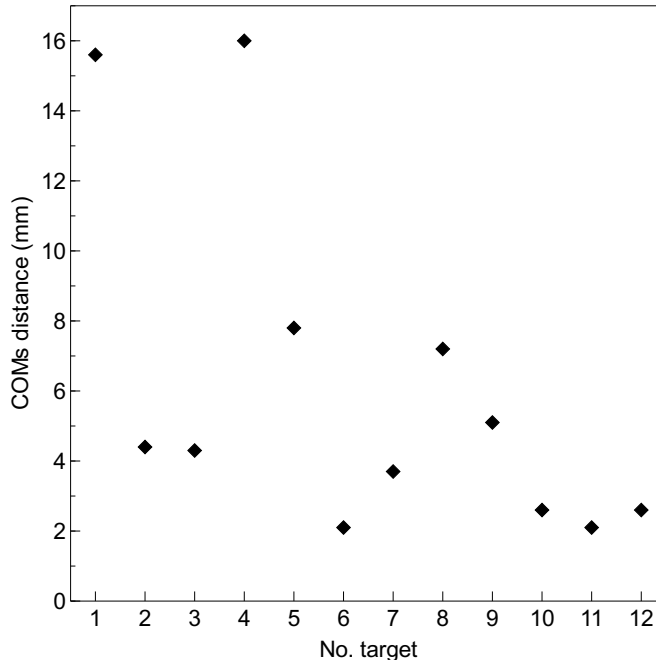
Figure 3.4: Distance between COMs of delineated volumes on CT
with and without contrast product, for all targets

For most of the cases the distances between the COMs are between 2 and 8 mm. For two targets, deviations around 16 mm are obtained though (targets #1 and #4). The median value is 4.4 mm.
The two largest distance values correspond to the two smallest targets.
The dCOM values are completely different for targets #3 and #4, which correspond to the same patient.
The majority of the dice coefficients are between 0.7 and 0.9. For targets #1 and #4 the dice is extremely low, which is consistent with the above observations. For target #4, for which the COMs distance was the largest, the two contours present a zero overlap. The delineated volumes on CT with and without contrast product are completely disjointed.
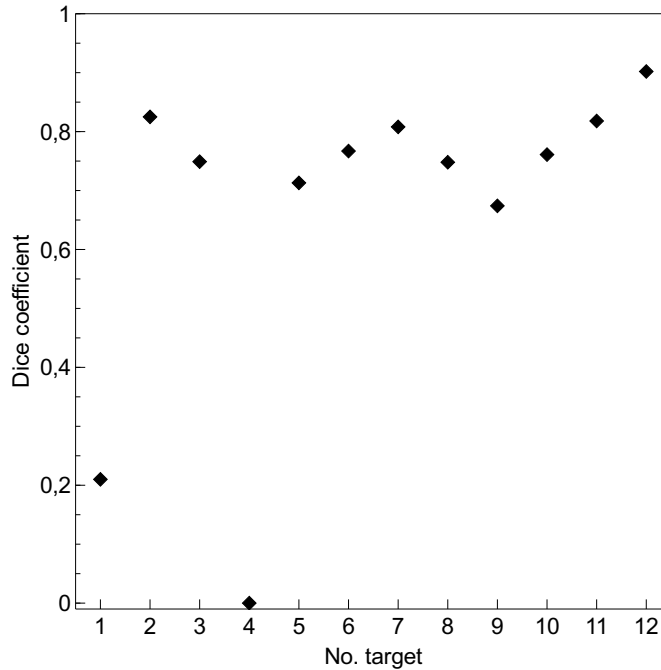
Figure 3.5: Dice coefficient values for delineated volumes on CT with and without contrast product, for all targets

For the four targets #2, #7, #11 and #12, the dice is superior to 0.8. These targets do not correspond entirely to those for which the COMs distances are lower. Only targets #11 and #12 show results that are consistent.

The third factor that plays a role in the overlap evaluation between the two VOIs is the volume ratio. Despite the larger distance between the COMs, the overlap coefficient is better for targets #2 and #7 than for targets #6 and #10. This can be explained by the fact that targets #2 and #7 have a larger absolute volume.
The mean volume ratio ranges from 0.88 to 2.58.

Below, The contours performed on the CT without injection and those on the CT with injection are displayed on the same image. Two different cases are distinguished; on the first image, Figure 3.6(a), we can see an overlap of outlines, that is observed in the majority of studied cases, and in

the second case, Figure 3.6(b), the outlines are completely separated. The contouring performed on the CT acquired without injection of contrast product corresponds to the contour in blue on the Figures. The other contour, in red, was drawn on the CT acquired with injection of contrast product.

(a) partial overlap   (b) non overlap
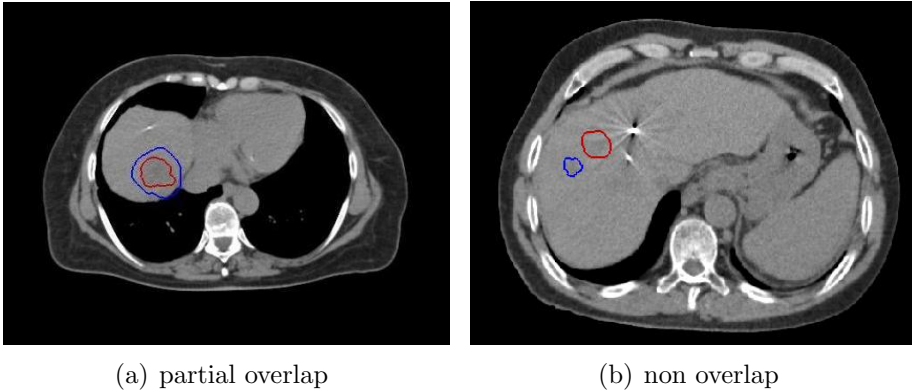
Figure 3.6: Two target contours, for two different patients

3.3.1.2 Dosimetric Impact of contrast product for CT images acquisition

Two dose distributions have been calculated from the CT acquired with injection of contrast product and from the CT with modified densities. Hereafter, the CT with modified densities will be designated as CT without contrast product for convenience.

The dose differences (ΔD) are not visible on the isodose plots. It is necessary to display the subtraction of the two distributions to highlight the differences, as on Figure 3.8.
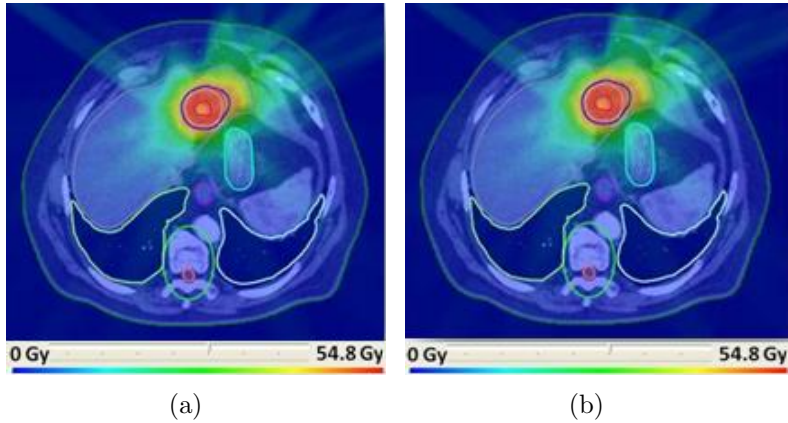
Figure 3.7: Dose distribution calculated on CT
without (a) and with (b) contrast product
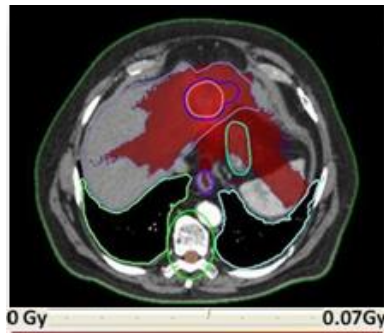
Figure 3.8: Subtraction of the two dose distributions

To locate and quantify the dose differences, the mean dose difference values (ΔDmean) resulting from the subtraction between the two dose distributions were calculated. The ΔDmean in absolute values and normalized to the delivered dose are shown in Table 3.5 and Table 3.6 respectively.

Structure	ΔDmean (cGy)									
	patient 1	patient 2	patient 3	patient 4	patient 5	patient 6	patient 7	patient 8	patient 9	patient 10
GTV	25.4	-16.2	-12.0	12.2	-28.3	3.3	-3.1	1.5	-1.8	-4.8
CTV	24.2	-15.1	-12.9	11.5	-29.9	2.7	-3.5	2.0	-1.1	-3.5
PTV	23.3	-14.4	-12.9	11.1	-27.4	2.7	-3.7	-0.8	-0.8	-3.9
right lung	7.7	-	-1.4	1.2	-1.0	-	0.8	-2.3	1.9	-3.7
left lung	2.9	0.8	-0.7	0.3	-0.8	-0.5	0.2	-1.9	-0.1	-0.2
heart	0.0	-7.7	-0.4	2.2	-	-0.3	-0.2	-0.5	-0.1	-0.7
liver	5.0	-3.6	-	4.0	-3.8	-1.1	-0.2	0.2	-0.7	-1.7
spinal cord	1.0	0.6	-0.6	0	-1.5	-0.4	-1.1	-0.6	0.2	-2.3
esophagus	3.1	-2.4	-2.0	-	-	-0.9	-	-0.4	-	-3.2
stomach	0.6	-1.5	-1.0	1.8	-1.4	-1.1	-0.3	0.5	-1.1	2.2
duodenum	0.5	0	-0.5	0.7	0.1	-0.6	0.7	0	-0.3	-0.7
right kidney	0.4	-0.5	-0.4	-0.8	-	0	-0.2	0	0.6	-0.7
left kidney	0	0.1	-	-0.5	-	-	-	-	-0.3	-0.4

Table 3.5: Mean dose difference in the structures (ΔDmean in cGy) For each patient

A graphical summary is shown in Figure 3.9 to a better overview of the results.
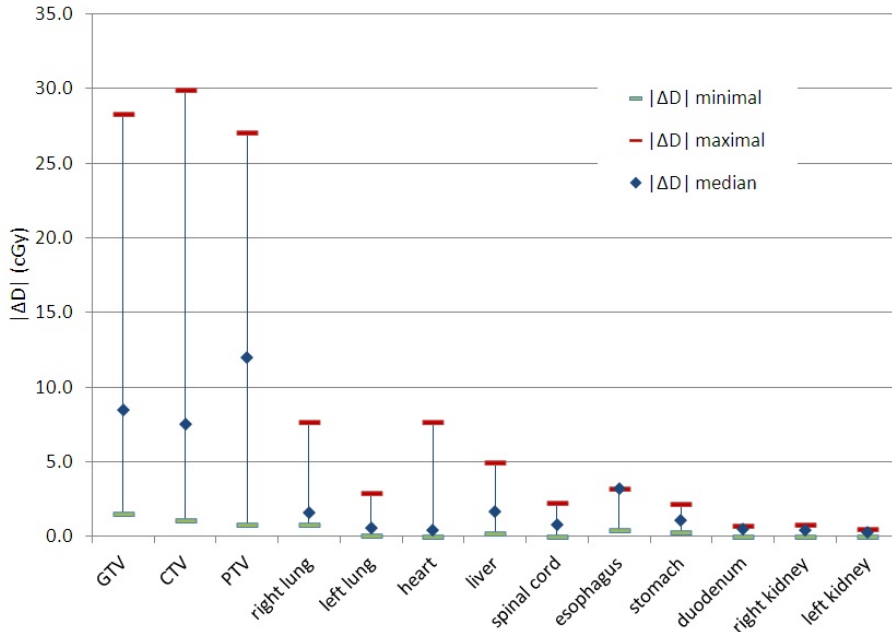
Figure 3.9: Median, minimal and maximal values of ΔDmean, for all structures and all patients

We note that differences vary from one patient to another, but remain in the same order of magnitude. The median values of dose differences are between 1 and 3 cGy for OARs, and between 7 and 12 cGy for tumor volumes. Dose differences do not exceed 30 cGy in absolute value and 1% of the dose received by the volume.

The highest dose differences in absolute value are mostly concentrated in structures that received high doses, especially the target, but all values are extremely low. The dissimilarities between the two dose matrices are too low to be visible on the dose-volume histogram (DVH).

Results are presented in absolute values. The positives and negatives dose differences can be dissociated and localized. In a case of a positive ΔDmean, i.e. while the calculated dose from the CT with injection is higher than the calculated dose from the CT without, the delivered dose is overestimated.

We distinguish 36% of overestimation and 64% of underestimation illusatrating the fact that errors are stochastic and not systematic.

Structure	%Dmean of structure									
	patient 1	patient 2	patient 3	patient 4	patient 5	patient 6	patient 7	patient 8	patient 9	patient 10
GTV	0.5	0.3	0.3	0.3	0.6	0.1	0	0	0.2	-
CTV	0.5	0.3	0.3	0.2	0.6	0.1	0	0	0	0.1
PTV	0.5	0.3	0.3	0.2	0.6	0.1	0	0	0	0.2
right lung	1.3	-	0.6	0.4	-	0.5	1.2	0.4	0.7	-
left lung	1.2	0.1	0.3	0.2	0.3	0.2	1.1	0.1	0.1	0.1
heart	0	0.8	0.2	0.8	-	0.2	0.2	0.1	0	0.3
liver	0.4	0.2	-	0.3	0.5	0.1	0	0	0	0.1
spinal cord	0.3	0.1	0.3	0	0.4	0.2	1	0.5	0.1	0.6
esophagus	0.6	0.3	0.5	-	-	0.3	-	0.2	-	1.0
stomach	0.2	0.2	0.2	0.4	0.2	0.4	0.3	0.1	0.2	0.5
duodenum	0.2	0	0.2	0.1	0.1	0.1	0.2	0	0.1	0.2
right kidney	0.1	0.2	0.2	0.4	-	0	0.1	0	0.2	0.2
left kidney	0	0	-	0.3	-	-	-	-	0.2	0.2

Table 3.6: Percentage of mean dose in the structures (%Dmean) For each patient

3.3.2 Reproducibility of GTV delineation on MRI
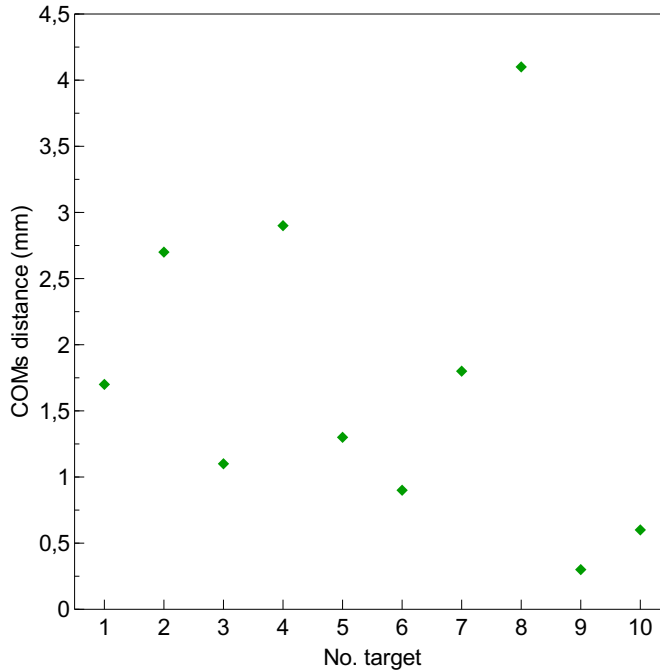
Figure 3.10: Distance between COMs of volumes twice delineated on MRI,
by the same radiation oncologist, for all targets

The results of distance between the COMs and Dice coefficients are shown
in Figures 3.10 and 3.11.

All the distances between the COM of the two contours are inferior to 4
mm with seven lower than 2 mm. The distance for targets #8 is twice
that for target #7, however they belong to the same patient. The mean
distance is 1.7 mm.

Overall, Dice values are close to one. The values are between 0.8 and 1
for or all targets and half of the cases have a dice > 0.9.

The Rv values are distributed around 1.13 with a standard deviation of
0.19.
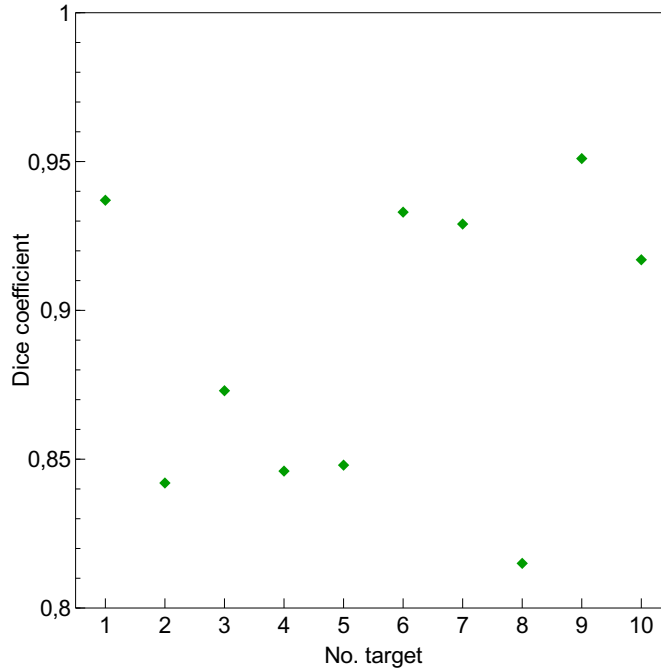
Figure 3.11: Dice coefficient values for volumes twice delineated on MRI, by the same radiation oncologist, for all targets

3.3.2.1   Impact of radiologist

The contours performed by the radiation oncologist have been reviewed by a radiologist expert in interpretation of MR images. For each patient, the radiologist gave his opinion on the sequence used and on the contours drawn. The results are summarized in Table 3.7.

For certain patients, the radiologist confirmed the contours performed by the radiation oncologist. For others, the sequence used was inappropriate or the contours were not correct.

For patient #5, the contours were changed by the radiologist. The comparison between these new contours and the original contour gave a distance between their COMs of 1.8 mm and a dice coefficient of 0.896. The original contour has been expanded.

For patient #6, the contours of the radiation oncologist actually corresponded to an injury due to previous radiofrequency treatment. This type of scar is distinguishable from a liver tumor as it appears white in

a T1 and black in a T2 sequence.

For patient #7, the image quality was too poor.

The images of patient #8 presented duplication artifacts.

	Radiologist reviews
patient 1	agree with the sequence used
	one of the two contours is preferred
patient 2	Portal sequence is preferred - target limits are more clearly defined
	one of the two contours is preferred
patient 3	agree with the sequence used
	one of the two contours is preferred
patient 4	agree with the sequence used
	one of the two contours is preferred
patient 5	agree with the sequence used
	modification of the contour
patient 6	agree with the sequence used
	the two contours are completely wrong
patient 7	poor image quality
	acquire a new MRI examination
patient 8	Lava InPhase or Portal sequence are preferred
	one of the two contours is preferred
patient 9	Arterial time sequence is preferred
	the two contours are correct

Table 3.7: Radiologist reviews regarding the target,
contoured by a radiation oncologist, for all nine patients

3.3.3   Results summary

	dCOM (SD) (mm)	dice (SD)	Rv (SD)
comparison of contouring CT without IV - CT with IV	6.1 (4.9)	0.665 (0.271)	1.38 (0.48)
reproducibility of contouring on CT with IV	4.1 (3.3)	0.749 (0.135)	1.09 (0.29)
comparison of contouring by two physicians on CT with IV	6.6 (6.3)	0.669 (0.263)	1.20 (0.64)
reproducibility of contouring on MRI with IV	1.7 (1.2)	0.889 (0.049)	1.13 (0.19)

Table 3.8: Overview of results for the different studies

3.3.4   Impact on CTV

GTVs radius (mm)	CTV1 radius (mm)	Dice (GTV1/GTV2)	% GTV2 in CTV1
distance between the GTV COMs = 6 mm			
5	10	0.21	0.95
10	15	0.56	0.98
25	30	0.82	0.99
35	40	0.87	1.00
50	55	0.91	1.00
75	80	0.94	1.00
100	110	0.96	1.00
distance between the GTV COMs = 11 mm			
5	10	0.02	0.27
10	15	0.26	0.66
25	30	0.68	0.88
35	40	0.77	0.92
50	55	0.84	0.95
75	80	0.89	0.97
100	110	0.92	0.97

Table 3.9: Dice and percentage of GTV2 included in CTV1 for variable size of GTV

Table 3.9 shows the Dice and the percentage of GTV2 included in CTV1, for variable size of GTV. The margin applied from GTV to CTV is 5 mm, and the distance between the GTV COMs is 6 and 11 mm. 11 mm corresponds to the maximal distance between two GTVs delineated by a unique radiation oncologist.
The results demonstrate that GTV2 is mainly included in the CTV when the distance between the two GTV COMs is small, especially for large targets. GTV2 is only partially included in CTV1 when the distance between the GTV COMs is larger.

For HCC cases, the CTV-PTV margin is 1cm. The contouring uncertainty is even more negligible, with 96% of GTV2 in CTV1 for the smallest target (5mm diameter) for a distance between the GTV COMs of 11mm.

GTVs radius (mm)	CTV1 radius (mm)	distance between the GTV COMs	Dice (GTV1/GTV2)	% GTV2 in CTV1
6	11	5.5	0.36	0.99
8	13	8	0.31	0.84
35	40	11	0.77	0.92

Table 3.10: Dice and percentage of GTV2 included in CTV1, for three patient cases

The calculation was performed for the three patients for which the reproducibility of target contouring on CT was the poorest (Table 3.10). The percentages of volume of the GTV2 included in the CTV1 are high despite a very low Dice between the GTVs, particularly for the two smallest targets. The GTV2 being not totally included in the CTV1, the dose coverage of the GTV actually delineated will be degraded.

3.3.5 Dosimetric Impact of Target Delineation Error

3.3.5.1 With CTV

The DVHs for 3D distribution calculated by MCS when targeting the PTV are shown in Figure 3.12.
The GTV coverage is not degraded, certainly due to the large GTV-CTV margin relative to the shift between the two GTVs.
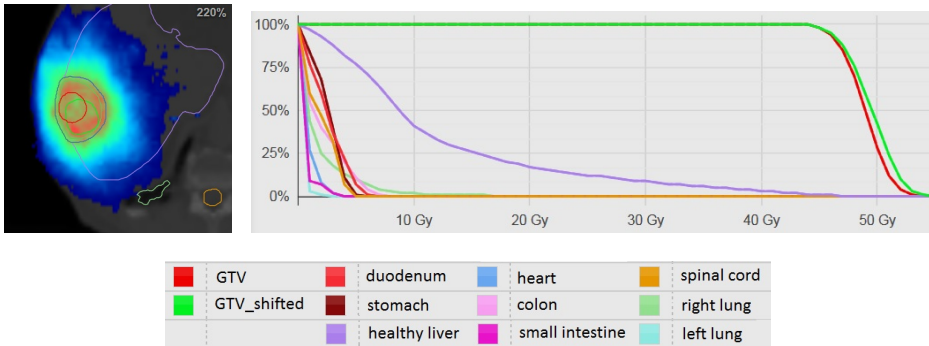
Figure 3.12: DVHs for 3D distribution calculated by MCS, targeting the PTV

3.3.5.2   Without CTV

Figure 3.13 presents the DVHs for 3D distribution calculated by MCS when targeting the PTV_margin.
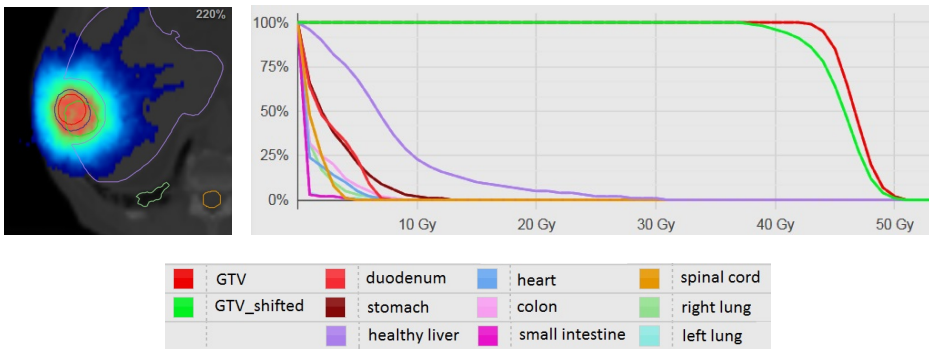
Figure 3.13: DVHs for 3D distribution calculated by MCS, targeting the PTV_margin

The dose coverage of the shifted GTV is degraded. Only 40.5 Gy is received by 95% of the shifted GTV when 44 Gy is received by the GTV. This is directly observable on the Dose distribution image. The shifted GTV is partially outside of the PTV_margin.

3.4 Discussion

The comparison of contours based on CT with and without contrast agent leads to low dice values and large distances between the contours. Extreme outliers are obtained, for which the two structures contoured are not similar, either in size or location. The presence of contrast product during the acquisition of CT has an important impact on the visualization of the target. The CT imaging effectiveness to define liver tumors is dependent on the opacification with iodine. Routinely, the CT images are acquired with injection of contrast product, except for the cases for which iodinating gives problems of renal toxicity and allergic reaction.

The dosimetric analysis demonstrated that the presence of contrast product during the acquisition of CT images for the treatment planning calculation does not have any influence on the dose distribution. In our method, we replaced the density of structures by an average density. This is why it would not be accurate to compare the minimum and maximum doses between both plans. In view of the differences in average doses, it is very unlikely to have spots where the dose is concentrated that would be significant in the recalculated dosimetry. However, it would be possible to push on the study to this level of detail if we could replace each voxel in the enhanced CT structures by the value of the corresponding voxel in the CT without injection. A good deformable registration algorithm would be needed because of respiratory movements which create considerable differences in organs position between the two scans.
The bias introduced by the homogenization of structures density is not significant when the result of the study is not either. Therefore, the CT images with injection of contrast product can be used to perform the treatment planning for patients with hepatic lesions treated on CyberKnife.

The study of the reproducibility of contouring by a physician on an enhanced contrast CT shows a better overlap of contoured targets with a higher average value and a lower variability of results. Both contoured volumes are closer and their differences in absolute volume are lower. We also note the absence of extreme situations where targets have a very low or zero overlap. Although the contrast product allows a relatively better location and delimitation of the target in the liver, the reproducibility of contouring is still rather poor.

When reproducibility of contouring on CT with contrast product is really good, the contours of the same target drawn by two different physicians are very similar, that is not the case in the study. The bias introduced by the difference of their judgment, their experience or their learning, should not be significant when the imaging modality is well appropriated for contouring.

For this reason, the interest of the use of MRI for the delineation step was evaluated and the reproducibility of target delineation based on CT and MR images has been compared.

The results obtained on MRI show a very good reproducibility of contouring. The location and the determination of the target volume of the two contours performed by the radiation oncologist are very good. The MRI modality appears to be very suitable for the target delineation in the liver.

However, the intervention of a radiologist can provide a significant improvement, thanks to his interpretation of the different MR sequences available. Indeed, the study shows that the opinion of the radiologist can lead to changes of the contours performed by the radiation oncologist. The interpretation of the radiation oncologist only of MR images can lead to significant errors. Certain injuries caused by previous treatment look like tumor that only a skilled radiologist can distinguish, as for one case in our study, for which the contoured target actually corresponded to the effects of a previous radiofrequency treatment.

In the case of poor MR images and where the target volume is large, the radiologist will prefer acquiring new MR images to not irradiate more volume than necessary. The radiologist may need a second viewing of the target on another imaging modality, such as CT with injection of contrast product to ensure the accuracy of target contouring.

In the context of target delineation on MR images, the presence of a radiologist during the delineation step appears essential. Routinely, the radiologist could select the preferred sequences (and understands better how to combine several sequences), based on diagnostic MRI images, to avoid the acquisition of multiple sequences for contouring. The radiologist may assist the radiation oncologist during contouring.

The reproducibility of the target contouring is better when it is performed on the MR images, that is why it should be introduced in routine. The ideal process would be to perform the contouring and the treatment planning directly on the MR images for the CyberKnife treatment of liver patients. Future work will focus on the feasibility of MR based treatment planning, but some practical aspects need to be considered.

The liver cancer treatment is usually performed with the respiratory tracking system, for which the treatment planning requests the internal markers location in images. Early research has been conducted to find a sequence that allows both lesion and fiducials visualization in the same images. The Lava Flex Sequence in coronal view seems to solve this problem. The figure shows the images obtained with this MRI sequence.
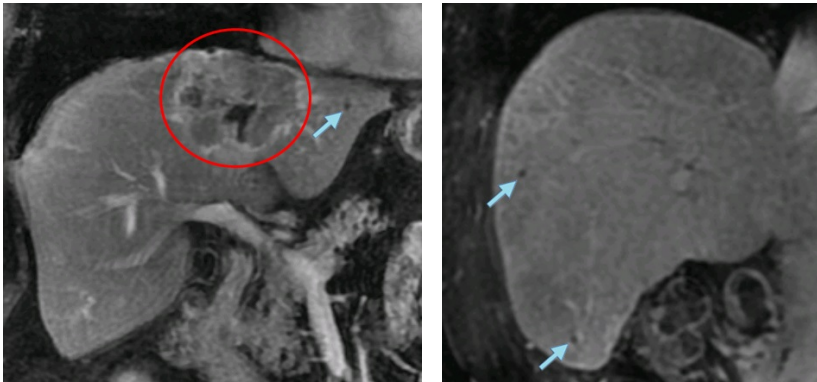
Figure 3.14: MR images of LavaFlex Coronal sequence, for two patients, with target in red circle and fiducials pointed by the cyan arrows

The delineation of OARs should be performed on these images, but this is a difficult exercise because of the blur induced by organs motion, especially in the visceral area.

The treatment plan would be performed on the MR images. In a first time, approximations will be made when using the TPS (Multiplan). The structures density will be manually changed by using so-called bulk densities. We have seen above that the densities homogenization in the TPS does not introduce a significant bias. In a second time, the MRI images will be converted to density and tissue composition information on a voxel by voxel basis, leading to a so-called pseudo-CT dataset that can be imported in the TPS or in our Monte Carlo software [79] [80].

Another practical difficulty will be the MR images acquisition in treatment positioning for which an MRI simulator is needed.

In clinical practice, CT and MRI modalities are often visually combined or rigidly registered. The deformable registration would be a better alternative allowing direct mapping of MRI contours on CT images. This demands accurate elastic registration algorithms which are not yet available in clinical routine.

The results regarding the reproducibility of the GTV delineation need to be translated into clinical impact. At our center a margin of 5 mm (for metastasis) or 1 cm (for HCC) is used when defining the CTV. Obviously part of the GTV delineation error is taken into account in the margin, as illustrated in current chapter. On the other hand, the margin is also included to take into account microscopic spread of tumor cells around the GTV (in principle this is the actual purpose of the CTV margin). In that case part of the actual CTV defined as GTV plus microscopic spread will be underdosed because of the delineation error. For HCC tumors, a margin of 1 cm is applied, but this is again mainly to take into account the microscopic spread. Other radiotherapy departments often do not even use a margin to define the CTV (CTV = GTV). This is for example the case in RTOG 1112 [77] and in the recommendations published by the AAPM TG101 [78].
The dosimetric impact of wrongly delineating the GTV is blurred by the CTV. The dosimetric impact becomes more significant and must not be disregarded when no margin is used to define the CTV.
The 3 mm PTV margin cannot be used as an excuse as this uncertainty is defined to take into account patient setup uncertainties and uncertainties related to the linac. In that case, the main conclusion of this chapter is that liver lesions cannot be delineated correctly without MRI. Even a CT dataset with contrast should be complemented with MRI images. The two image modalities can be combined visually or using rigid or non-rigid registration. And even in that case, the expertise of a radiologist can increase the accuracy and reproducibility of the GTV delineation for liver tumors.

3.5   Conclusion

In future, it should be possible to perform the delineation of targets and organs at risk on another imaging modality than CT, to increase the contouring accuracy. The MR imaging seems to be a good alternative, provided that the radiation oncologist is assisted by a skilled radiologist. Practical aspects should be solved and data should be added to the study, before the introduction in routine of the MR based delineation for liver targets.

Meanwhile, as the presence of contrast product has no influence on the dose calculation, the target contouring can continue to be performed on CT with enhanced contrast, with the aid of MR sequences.

Also, continuous education, training, and cross-collaboration of the radiation oncologist with other specialties can reduce the degree of variability in tumor delineation.

Chapter 4

Correlation between Target and Fiducials movement

4.1   Introduction

The CyberKnife® treatment of liver tumors is typically performed using the Synchrony™ respiratory tracking system in order to reduce errors introduced by respiratory liver motion. Liver motion occurs primarily in the superior-inferior (SI) direction in the order of 10 mm [81] [82] [83] [84]. The movements in the left-right (LR) and antero-posterior (AP) directions are lower. These breathing movements are limited by using an elastic abdominal belt during the treatment.

The Synchrony treatment mode uses external markers, placed on the patient chest, and implanted fiducial markers for target and beam motion correlation. Previous studies show a good correlation between internal fiducial motion and external marker motion [81] [85]. They report that when the fiducials are widely spaced, the correlation is lower because of the presence of liver deformations. The fiducials implantation inside the tumor volume is not possible because of the risk of tumorous cells spreading when pulling out the needle. The distance of the internal markers to the target, and the liver movements/deformations can introduce differences in fiducials and target motion.

The correlation between target and fiducials movements is considered exact when the internal markers are correctly arranged, i.e. the three or four markers encircle the tumor at a distance of less than 60 mm [86]. The fiducial rotations are calculated during patient free breathing and the patient is positioned taking into account the median rotation. During actual delivery, the CyberKnife robot refers to the translations of the fiducials center of mass to adapt the beam position and track the target.

The liver is a mobile organ that undergoes significant movements and deformations during the respiratory cycle. The correlation between target and fiducial motion must be verified to ensure the accuracy of this type of treatment. A bad correlation could introduce errors in beam positioning and thus a difference between the prescribed dose and the dose actually delivered.

The aim of current chapter is to determine the validity of Synchrony tracking by evaluating the respiratory movements of target and fiducials.

4.2 Methods and Materials

The validity of the Synchrony tracking mode depends on the hypothesis that the movements of target and implanted fiducials are identical. To test this hypothesis, different methodologies can be considered. The optimal method would be based on 4D images that provide an optimal visualization of both the target and the fiducials. 4D CT imaging of the liver is performed without contrast product, and as shown in previous chapter, the visibility of the target is poor. The target is easily visible on 4D PET images. On these images the fiducials are not visible though. A logical solution is to combine different image modalities as the PET-CT scanner to visualize the fiducials. The main issue is the large difference in acquisition time between the 4D CT (30s) and the 4D PET (15 minutes). An alternative method, purely based on 4D CT is the usage of deformable image registration to project the target contours on all respiratory phases. The accuracy of this method depends largely on the obtained deformation fields. As both methods have inherent uncertainties, both will be used to investigate the accuracy of Synchrony tracking for liver tumors.

4.2.1 Patient characteristics

The images of 9 patients, 4 women and 5 men, treated for HCC or metastatic liver tumors were analyzed. The number of tumors per patient ranged from one to three, tumors were located in different segments in the liver. Details are shown in Table 5.1. The tumor size corresponds to the Gross Tumor Volume (GTV) delineated.
For three patients, the lesions were hepatocellular carcinoma and the 4D PET-CT examination was realized with injection of [^{18}F]fluorocholine (FCH) radiotracer. For the other patients, the [^{18}F]fluorodeoxyglucose (FDG) radiotracer was used.

The patients were treated on the CyberKnife system using the Synchrony respiratory tracking system, with three fractions of 15 Gy (except for patient #4 who received 3 fractions of 10 Gy).
Four internal markers in average were implanted percutaneously in healthy liver tissue surrounding the tumor using X-ray image guidance. The gold fiducials have a length of 4 mm and a diameter of approximatively 1 mm.

No. target	No. patient	Gender	Age	Tumor(s) location	Tumor size (cc)	Radiotracer
1	1	M	64	metastasis SI	29.8	FDG
2	2	F	55	metastasis SVIII	17.3	FDG
3	3	F	54	metastasis SVI	16.3	FDG
4	4	M	73	metastasis SVII	69.5	FDG
5				metastasis SII	3.2	FDG
6	5	M	64	HCC SVII	2.0	FCH
7	6	F	74	HCC junction SV-SVIII	16.4	FCH
8	7	M	65	metastasis SVIII	18.4	FDG
9	8	F	60	metastasis SVIII	27.9	FDG
10				metastasis SIV	7.2	FDG
11				metastasis SVI	20.1	FDG
12	9	M	66	HCC SIII	3.0	FCH
13				junction SIV-SVI	60.7	FCH

Table 4.1: List of patient characteristics

The distance between target and fiducials has been determined for each target. The breathing movements have been quantified for target and fiducials, and the liver deformations have been evaluated.

4.2.2   METHOD A: PET-CT for 4D target delineation

4.2.2.1   4D PET-CT acquisition

The 4D PET-CT images were acquired with the Discovery™ 690 PET-CT (GE Healthcare, Waukesha, WI) coupled with the Varian® Real-time Position Management™ system (RPM) (Varian Medical Systems, Palo Alto, CA) for patient respiratory recording. A period of at least one week was respected between fiducial implantation and 4D PET-CT image acquisition, to avoid fiducial migration.

The patients were immobilized in the treatment position, i.e. in supine position with all immobilization equipment used during the treatment including the restraining belt (a wide elastic belt). This abdominal compression minimizes the breathing movements amplitude during the acquisition. The 4D images were acquired during patient free breathing.

The two 4D modalities were acquired sequentially, CT imaging first. The whole 4D PET-CT scan duration was approximately 20 minutes, including less than a minute for the CT scan and 15 minutes for the PET scan. The time interval between CT and PET acquisition was about one minute.

All CT series were acquired in cine mode, using the retrospective approach. Images are continuously collected during several entire respiratory cycles with the patient breathing freely. After 4D scanning, images were sorted into several phases evenly distributed over the respiratory cycle, based on the temporal correlation between surface motion and data acquisition. The 3D CT scans were reconstructed with a slice thickness of 2.5 mm. The retrospective 4D scanning produces 5 or 10 volumetric CT and PET datasets according to the protocol used. Each 3D image set obtained corresponds to a specific instance of the breathing cycle and the 0% phase, the first phase of the cycle, corresponds to the end-inhalation. All CT and PET images were imported into Oncentra MasterPlan 3D treatment planning system (Nucletron, Veenendaal, The Netherlands).

4.2.2.2   4D PET-CT segmentation

The fiducial coordinates were manually determined on the CT images of each phase. As the target volume is not visible on the CT scans, the segmentation task was performed on the PET images and duplicated on the CT images.

The Oncentra MasterPlan planning system has been used for the segmentation based on PET images. To have the best visibility of the target volume, a PET intensity threshold has been arbitrarily fixed with the image display characteristics center and width. The contrast values have been used for the threshold determination, because the software used does not give the possibility to know the SUV. The PET signal intensity issued from the lesion was the same for all phases because the PET images were sorted in equal temporal phases. The same threshold was used for all phases to compare the characteristics of the target volumes.
After delineation, the target contours were copied on the CT slices and interpolated on the intermediate slices.

Figure 4.1 illustrates the target delineation in PET images. CT and PET images were merged on this figure.
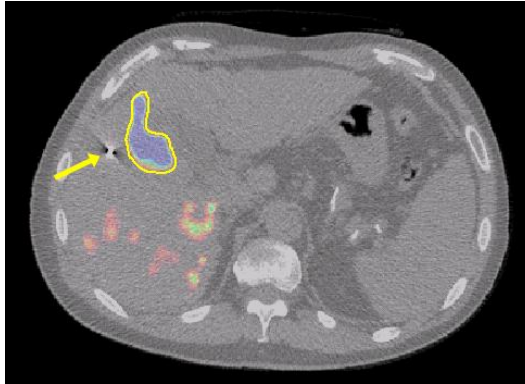
Figure 4.1: Merged CT and PET images. One fiducial is observable (yellow arrow). The target is delineated (yellow line)

4.2.2.3   Evaluation of METHOD A

The target segmentation procedure based on PET images was manually performed, which could be a cause of uncertainties. To ensure the delineation reproducibility, the contours of two targets were drawn ten times by the same operator, for one phase. The first target had an average volume around 70cc (target #4) and the second was smaller with a volume around 3cc (target #5). The contouring uncertainty was evaluated observing the variation of the absolute volume, the Dice coefficient and the distance between the target COMs, between all the different 3D volumes contoured.

Other errors could be introduced by the MatLab program. It is important to verify the correctness of the registration performed with the program. The absolute target volumes before and after registration were calculated for all twelve targets, to ensure that the target contoured is not deformed during the registration process.

Two combined imaging modalities are perfectly registered but they are not necessarily consistent, because both image sets are acquired one after another. In 4D combined PET-CT acquisition, CT is first acquired in a

very short period of a few seconds, and then PET is acquired during a much longer time of about 15 min.

4D PET-CT images of the XSight Lung phantom were acquired to test the quality of the 4D imaging. The phantom, in Figure 4.2, consists of a simulated thorax with lung and bone densities and a moving cylinder with an insert simulating the target (soft tissue). For the test, a solution of FDG has been placed in the insert and four internal markers were implanted in the moving piston nearby. A block with markers, visible to the camera, is placed on the horizontal platform. An engine allows the simultaneous craniocaudal movement of the piston and the anteroposterior movement of the platform, using a sinusoidal signal. Thus, the internal and external abdominal movements are simulated during breathing. As for the acquisition of patient images, the RPM system is used to sort images into several series, corresponding to different respiratory phases. The maximal motion amplitude between the two extreme positions has been measured for the insert COM and the fiducials COM.

Irregularities of the patient breathing during a real examination can affect examination quality. The consistency of PET and CT images has been verified with a real examination; the interdependence between target#3 and fiducial movement has been studied. Fiducial #2 is located very close to the tumor boundary, so their movement should be similar.

Figure 4.2: XSight Lung tracking phantom

4.2.3   METHOD B: Deformable Image Registration for 4D target delineation

4.2.3.1   DIR algorithm method

This method consists of applying a Displacement Vector Field (DVF) to the target contour of the reference phase to determine the target contour on the CT images of the other respiratory phases. The fiducial coordinates were manually determined on the CT images of each phase.

The deformation between two 3D image sets is materialized by a DVF which is a matrix wherein each element is a 3D vector. We distinguish the fixed images, corresponding to the target images, and the moving images, which undergo the transformations.
Overall, the mapping could be summarized by following Equations 4.1, with "moving_image_reg" corresponding to the moving image registered:

$$x_{moving\_image} + DVF\_x = x_{moving\_image\_reg} \simeq x_{fixed\_image}$$
$$y_{moving\_image} + DVF\_y = y_{moving\_image\_reg} \simeq y_{fixed\_image} \qquad (4.1)$$
$$z_{moving\_image} + DVF\_z = z_{moving\_image\_reg} \simeq z_{fixed\_image}$$

The principle of the Deformable Image Registration (DIR) is detailed in chapter 2.

The calculated DVFs were applied to the contour points using a MatLab (Mathworks Inc, Natick, MA) program developed internally. The new contours obtained were saved in a DICOM format file.

4D images for all patients have been sent to a team of researchers of Accuray who have calculated the DVFs with a powerful DIR algorithm and the DVFs were returned for analysis.
An alternative method for DVF calculation using a MatLab free access program named DIRART, which was the object of several papers in e.g. Medical Physics, was evaluated in order to be more independent from Accuray. The method has been found not sufficiently accurate.
The DIR algorithm of Accuray and the evaluation of the accuracy of the second method, using DIRART, are detailed in section 2.6 of chapter 2.

4.2.3.2 Evaluation of METHOD B

The DVF analysis allowed the evaluation of the displacements performed by the algorithm. Several functions have been created in MatLab to have an overview of calculated displacements and to evaluate the performance of each algorithm. Different tests consist of the DVF histogram analysis and applying the DVFs to the fiducials and specific contours.

4.2.3.2.a DVF histogram

A DVF histogram is the graphical representation of the distribution of DVF values. It allows determining, for example, if the calculated displacements are mostly small or large, positive or negative.
A MatLab function was encoded to visualize the DVF histogram and to determine the mean, minimal and maximal values.

4.2.3.2.b Fiducials and Structure displacement

The histogram shows the distribution of displacement values but does not allow assessing the correctness of these values. This is why other functions that provide the possibility to apply the DVFs on specific points were programmed.

Firstly, the three DVF matrices were applied to the fiducial coordinates. The fiducials of the registered reference phase and those of the target phase should be exactly overlapping. The difference between the fiducial coordinates is an evaluation of the accuracy of the deformable image registration algorithm.

Secondly the DVFs are applied to the contour points of the kidney, and the obtained volume is compared to the contours manually delineated. The quantification of the difference between the structure contours is a second mode of evaluation of the registration accuracy. The method of the contour displacement evaluation is identical to the method applied to the fiducial displacements; the three DVF matrices are applied to the contour points. The test is performed on the kidney which provides a volume that can easily be contoured reproducibly (refer to paragraph 2.6.3.2.a).

The registered structure of the reference phase and the structure of the target phase should be exactly overlapping if the algorithm works perfectly. The differences between both structures are measured with the absolute volume difference, the COM location difference and the Dice coefficient.

4.2.4   Correlation evaluation

To test the accuracy of the Synchrony tracking mode, the correlation between the movements of target and fiducials is evaluated. This comes down to assessing the relative position between target volume and fiducials for each phase. For that, the delineated volume of each respiratory phase was compared to the delineated volume of the primary phase, using a rigid registration based on the location of the fiducials. This procedure, divided into stages of registration and overlap evaluation, was performed using custom software developed in MatLab.

The Graphical User Interface (GUI), also used for the study regarding the contouring reproducibility (refer to chapter 3), allows users to perform a rigid registration interactively (Figure 4.3). The GUI functionality is described in detail in Appendix A.
The MatLab program allows choosing the fiducials used to perform the registration between two sets of images, mimicking the choice of the fiducials that are tracked during treatment in the Synchrony mode.
Program automation has been performed to enable testing all possible combinations of selected fiducials without repeating the operations of registration and calculation of comparison indices for each combination of selected ficucials. Only one intervention in the GUI allows obtaining the results (Dice, COM distance...) for each possible combination. The results are stored in a spreadsheet.
This program improvement brings an overview of the possible results depending on the fiducials combination and facilitates the fiducials choice for the user.
The minimal number of fiducials selected is 1 for registration based on fiducials COM translation, and 3 for registration taking into account the fiducials rotation. A maximum of 6 fiducials can be selected for the respiratory tracking during the treatment.
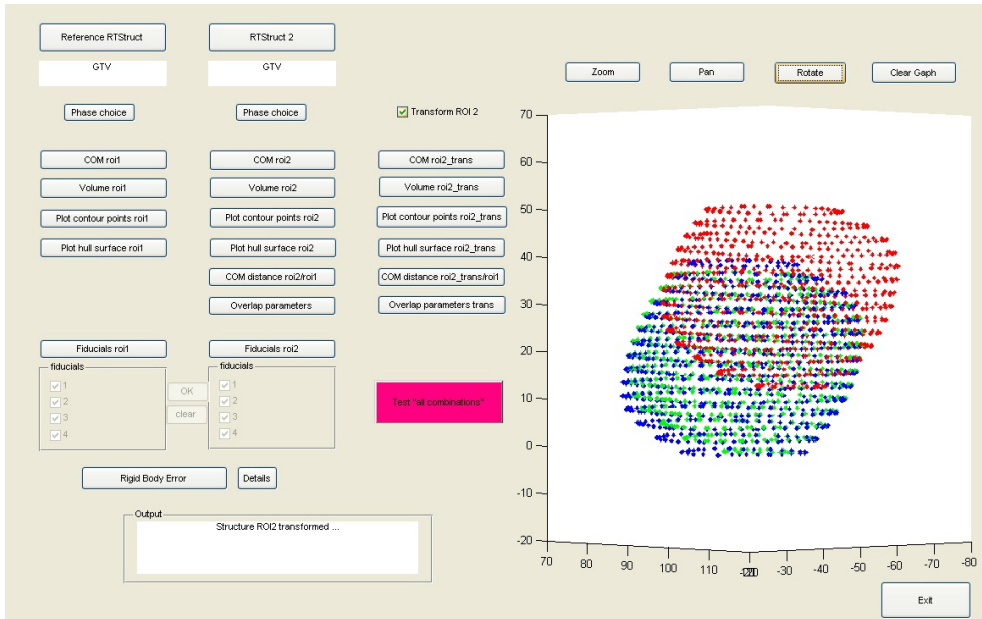
Figure 4.3: Graphical User Interface (GUI) encoded in MatLab. This GUI allows both registering two structures using different registration modes and calculating specific overlap parameters. The green contours are the result of the registration of the red to the blue structure based on the fiducials location

4.2.4.1 Registration

Several rigid registration methods were investigated to register the contoured volume of each respiratory phase to those of the primary phase. In the first method, a translation of the fiducials COM based on the coordinates of the fiducials in the two image sets was performed. Alternatively, the fiducials rotation is included in the calculation of the registration matrix in the second method. The first registration method allows testing the Synchrony tracking mode, while the second method allows evaluating the eventual benefit of the inclusion of the fiducials rotation in the tracking model.

The 0% phase corresponding to the end-inspiration time was arbitrarily taken as the primary phase. A perfect correlation between the movements of target and fiducials should lead to an exact overlap of the target contours of all respiratory phases, if the target is not subject to deformation.

4.2.4.2   Overlap calculation

The similarity between the target contours of each phase and the target contours of the primary phase were quantified by means of indicators, such as the **Dice Similarity Coefficient (DSC)**, the shift between the target COM before and after registration and the volume ratio. These three indicators have been described in the previous chapter.

The similarity measure over sets representing the overlap is determined with the DSC. This coefficient is defined as Equation 4.2, where Cr and Cn are two 3D structures:

$$DSC = 2 \times \frac{Cn \cap Cr}{Cn + Cr} \tag{4.2}$$

The DSC value ranges from 0 in the case when the two volumes are completely disjointed, to 1 when the two volumes have the same absolute volume and are perfectly overlapping.

The absolute volumes and the location of the target COM were calculated using the GUI from the contour DICOM files, for all respiratory phases. The **Center Of Mass location difference (dCOM)** is another indicator that allows the comparison between the target volumes of each respiratory phase.

4.3   Results

4.3.1   Patient characteristics

4.3.1.1   Target/Fiducials distance

The fiducial location were manually determined. The accuracy of this method was evaluated defining the fiducials location 10 times on the 3D CT of each respiratory phase for 3 patients. The absolute uncertainty was defined as the standard deviation (σ) multiplied by the coverage factor 2 to have a probability of 95% to find the value in the confidence interval. The absolute uncertainty of this measure set is 0.6, 0.7 and 0.8 mm for x,y and z coordinate. The fiducial coordinates were compared to

those obtained by automatically fiducial location using MultiPlan (Accuray treatment planning system). The mean coordinate differences were 0.2, 0.3 and 0.3 mm for x,y and z coordinate.

The uncertainty of the manually fiducial location is unsignificant because of the good accuracy of the method.
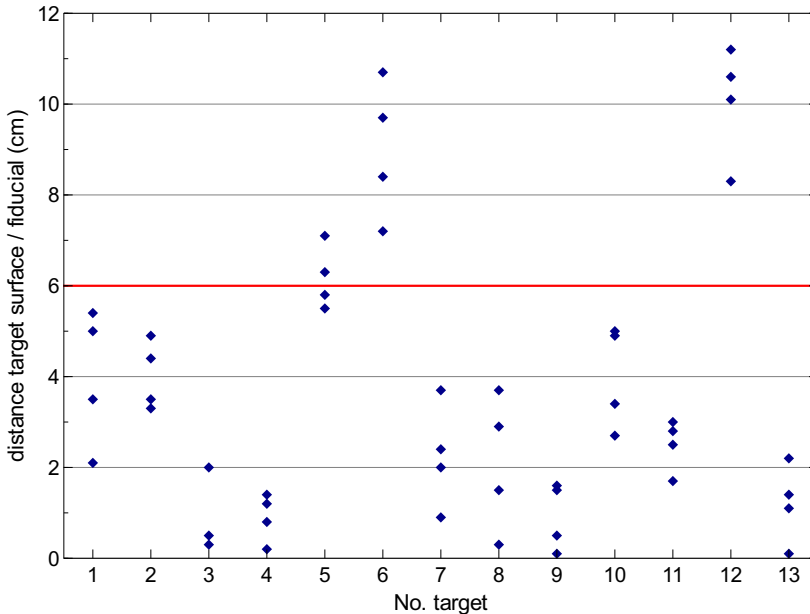
Figure 4.4: Minimal distance between the target surface and each fiducial, for all targets

The distance between the fiducials and the lesion met the recommendation regarding the maximum of 6 cm except for targets #5, #6 and #12, corresponding to the three smaller targets, as shown in Figure 4.4.

For patient #9, the fiducials were placed in relation to target #13 because target #12 was not detected before the PET examination. The use of the Synchrony mode for the treatment is not an obvious choice in this case.

4.3.1.2 Breathing movement amplitude

The distances between the fiducials COM of different phases were calculated. The amplitude of respiratory movements is reduced by the restraining belt. The larger distance corresponds to the maximal amplitude

No. target	Target COM			Fiducials COM		
	x	y	z	x	y	z
1	0	2	6	1	3	8
2	0	3	2	1	2	6
3	1	8	15	2	7	14
4	0	2	4	1	2	5
5	2	2	4			
6	3	4	9	2	3	6
7	2	1	7	1	4	9
8	2	5	10	1	5	9
9	1	0	6	1	1	7
10	1	0	6			
11	1	0	3			
12	0	2	3	2	4	10
13	1	4	8			

Table 4.2: Maximal amplitude of fiducials COM and target COM movements in the directions x, y and z (respectively left-right, anteroposterior and craniocaudal) in millimeters, during the entire respiratory cycle, for the nine patients

of the movement of the fiducials COM. The same calculation was performed for the target COM. The maximal amplitudes obtained in the three directions are shown in Table 4.2 for the nine patients.

For both fiducials and target, the largest movements are in the craniocaudal direction, with a mean of 7 mm for the fiducials and 6 mm for the targets. The fiducial motion is generally a little larger than the target motion. The maximal amplitudes in the three directions are always detected between the extreme respiratory phases.
Patient #3 exhibited the largest fiducials and target motion amplitudes in the craniocaudal and anteroposterior directions with maximum amplitude of 15 mm.

4.3.1.3 Liver deformations

Table 4.2 illustrates that in general, the fiducial and target amplitudes are relatively close, but seem to be different for some cases, suggesting the presence of deformations in the liver. The differences between craniocaudal amplitude for targets #2, #6, #11 and #12, are respectively 4, 3, 4 and 7 mm. The two targets #6 and #12 have the larger distance

between target and fiducials. The observed deformations are larger when the target/fiducials distance is large.

Some patients have several targets to be treated. It is interesting to observe in Table 4.2 if the different targets move in the same way. Three patients are concerned.
patient #4 : Although the target #5 is 5 cm more distant from the fiducials than target #4, the displacement amplitude of both targets is almost identical. The two targets appear to move little, with the same amplitude as the fiducials.
patient #8 : Targets #9 and #10 move as the associated fiducials. Target #11 moves slightly less, probably due to its location, very inferior and close to the ribs.
patient #9 : While target #13 and the fiducials undergo the same movements, target #12 moves much less. This target is very distant from the fiducials (about 10 cm) and located in the other liver lobe.

A function programmed in MatLab is able to calculate the rigid body error (RBE), corresponding to the deformations of the fiducials pattern during the breathing cycle. For each respiratory phase, the distance between all fiducial pairs is calculated. The difference of these distances between two phases represents a tissue deformation and is defined as the RBE. These deformations are checked during the treatment by the CyberKnife in Synchrony mode. If the rigid body error exceeds 5 millimeters, the treatment stops and the fiducial responsible for the large deformation is not taken into consideration for the Synchrony tracking.

The RBE was evaluated for the nine patients from the fiducials location in the 4D CT images. For all patients, the calculated rigid body error was less than 5 mm, without excluding any fiducial. The fiducials pattern did not undergo large deformation, this does not mean that there is no deformation in the whole liver. The case of patient #9 is an example that local deformations around the fiducials are very low while the deformation between the two lobes is significant.

4.3.2   METHOD A: PET-CT for 4D target delineation

4.3.2.1   Evaluation of METHOD A

The contours of two targets, of 70 cc (target #4) and 3cc (target #5) were drawn ten times by the same operator. The results regarding the determination of the delineation reproducibility were summarized in Table 4.3. The absolute uncertainty was defined as the standard deviation (σ) multiplied by the coverage factor 2 to have a probability of 95% to find the value in the confidence interval.

	Relative uncertainty of target volume	Dice coefficient	Absolute uncertainty of distance between the different target volumes contoured (mm)
target #4 mean volume = 70 cc	1.8%	0.99 ± 0.01	0.4
target #5 mean volume = 3 cc	2.3%	0.96 ± 0.01	0.2

Table 4.3: Relative uncertainty on absolute volume definition, Dice value and absolute uncertainty on distance between target COMs

The relative uncertainty on the absolute volume is low for both targets. The Dice values are very high with a negligible absolute uncertainty. The absolute uncertainties on the distance between the different target volumes contoured are submillimetric. The difference of mean distance between target #4 and target #5 is possibly due to a largest difficulty in the extremes slices (in craniocaudal direction) contouring of target #4. Dice coefficients, which are very sensitive to the volume changes, are superior to 0.96.

The reproducibility of the manual target delineation based on PET images is sufficient to not introduce a significant error.

The absolute target volumes before and after registration were calculated for all twelve targets.

The volume ratios ranged from 0.97 to 1.01 for all targets, with an average

of 1.00. The stability of the volume ratios illustrates that the MatLab registration does not deform the structure.

To test the consistency between the two image modalities, the maximal motion amplitude between the two extreme positions has been measured for the insert COM and the fiducials COM, for the phantom. The results are shown in Table 4.4. The target has been segmented on PET images of all phases, using the same arbitrary threshold of detection.

	amplitude	x	y	z
Fiducials COM	24.4	0.6	0.3	24.4
Insert COM	22.8	0.5	0.5	22.8

Table 4.4: Maximal motion amplitude for insert and fiducials COM (in mm)

The measures show the good quality of 4D acquisition for a phantom with a regular breathing cycle. A low difference in craniocaudal direction between insert and fiducials motion amplitude is due to the high speed of phantom motion.
The consistency of PET and CT images has been verified with a real examination to determine the impact of irregularities of the patient breathing during on examination quality. The interdependence between target#3 and fiducial movement has been studied.
For this real case, the fiducial movement measured on CT images and the target movement measured on PET images seem dissimilar (Figure 4.5). The movement of fiducial #2 are more similar to those of the target because is located very close to the tumor boundary. The difference in time duration between PET and CT acquisition impacts the consistency of the two image modalities.

These incoherences between PET and CT images would introduce a too large error in relation to the variable that is being evaluated, that is why this method will not be used for this study. The observation of these inconsistencies between the two imaging modalities provides an important information regarding 4D imaging.
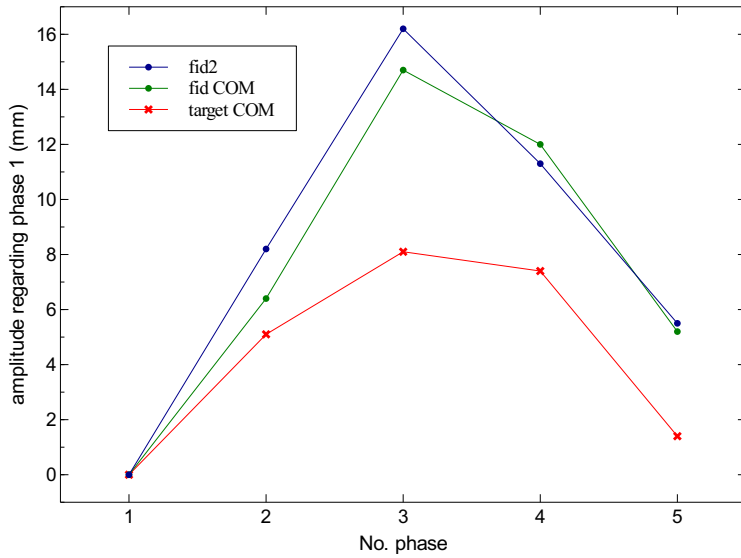
Figure 4.5: Motion amplitude of target and fiducials regarding phase #1, for target #3

4.3.3 METHOD B: Deformable Image Registration for 4D target delineation

4.3.3.1 Evaluation of METHOD B

4.3.3.1.a DVF histogram

The DVF for each direction, for the case of the registration phases #1 and #3 for target #3, is displayed in Figure 4.6.
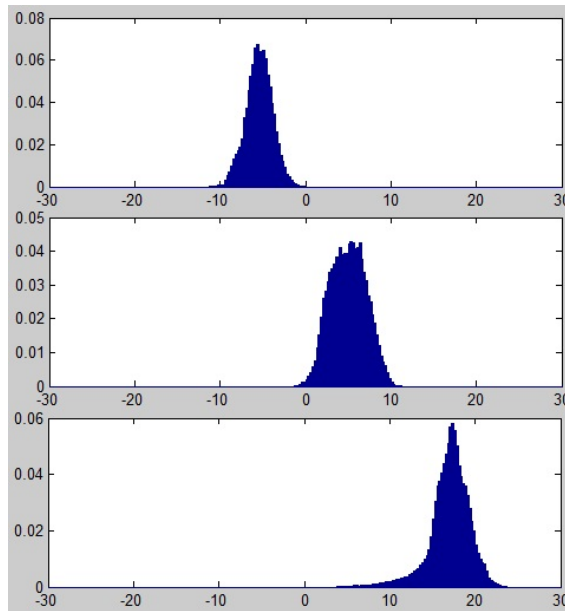
Figure 4.6: DVF histograms (in mm), downward : X,Y and Z component of displacement, for target #3, Ph #1 and #3 registered with the Accuray algorithm

4.3.3.1.b Fiducials and Structure displacement

The three DVF matrices were applied to the fiducial coordinates. The results for patient #8 are shown in Figure 4.7. The original fiducial location, for all phases, and the fiducial location after applying DVFs on the reference phase, are represented.

Globally, the results are submillimetric, demonstrating the accuracy of the DIR algorithm used.
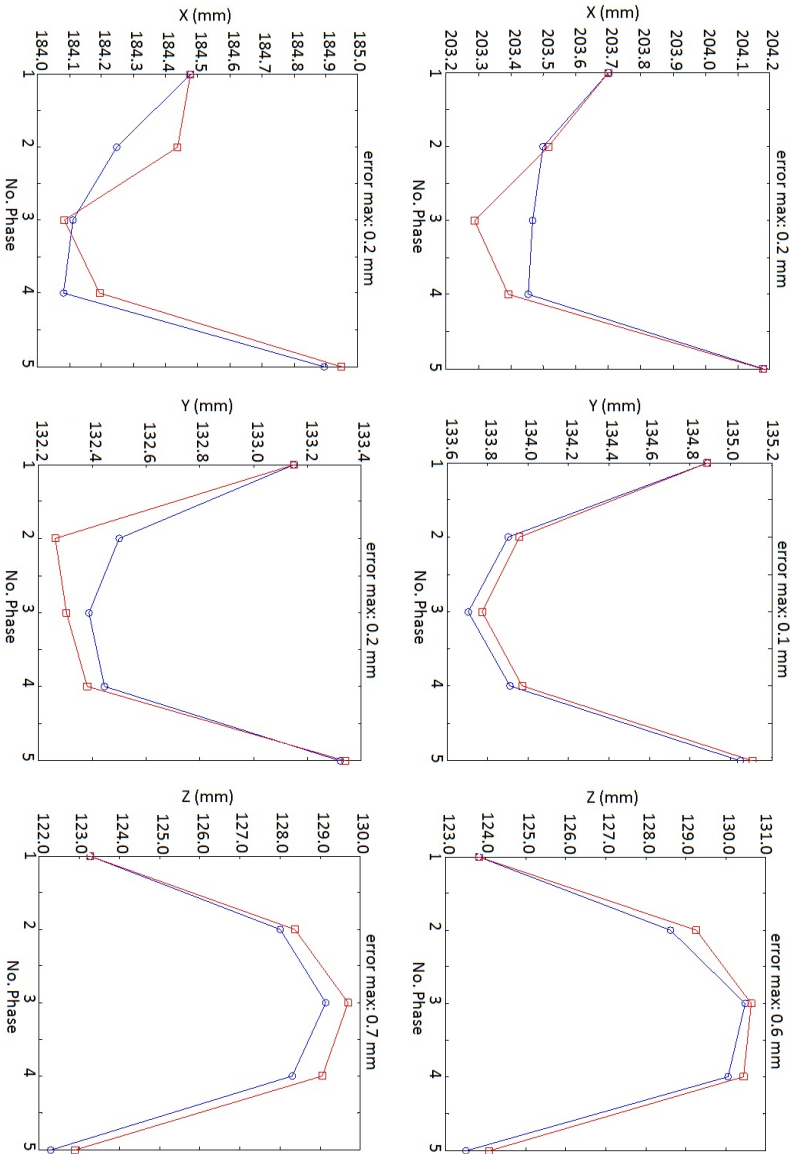
Figure 4.7: Original fiducial coordinates of all phases (red squares) and fiducial coordinates obtained after DVFs applying on reference phase images (blue circles).
Fiducials #1 and #2 of patient #8 (targets #9, #10 and #11)

(a) Ph1 (blue) - Ph3 (red)   (b) Ph1 (blue) - Ph1_def (green)

(c) Ph1_def (green) - Ph3 (red)
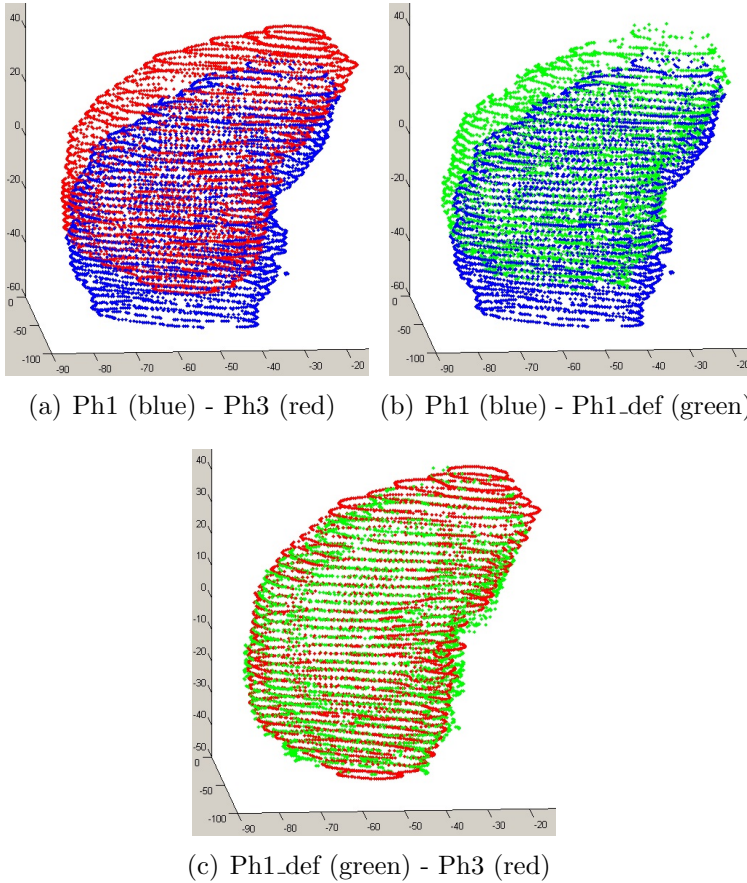
Figure 4.8: Structure of reference phase (Ph1), deformed reference phase (Ph1_def) and target phase (Ph3)

The three DVF matrices are applied to the contour points as a second evaluation mode of the registration accuracy. Three subfigures 4.8(a), 4.8(b) and 4.8(c) represent the structure of the reference phase (Ph1), the deformed reference phase (Ph1_def) and the target phase (Ph3), for patient #3. The two graphs of the figure 4.8(a) and 4.8(b) should be the same if the DVF calculation was accurate, and the figure 4.8(c) should represent a perfect overlap between the two structures. These Figures confirm the results observed with the fiducials, i.e. the DVF calculation is very accurate.

4.3.4   Correlation evaluation

4.3.4.1   Overlap index

The graphs in Figure 4.9 show the Dice coefficient before and after rigid registration based on fiducials, for targets #3, #6, #11 and #12. The distance between the target COM before and after the same registration mode, for the same targets, are presented in Figure 4.12.
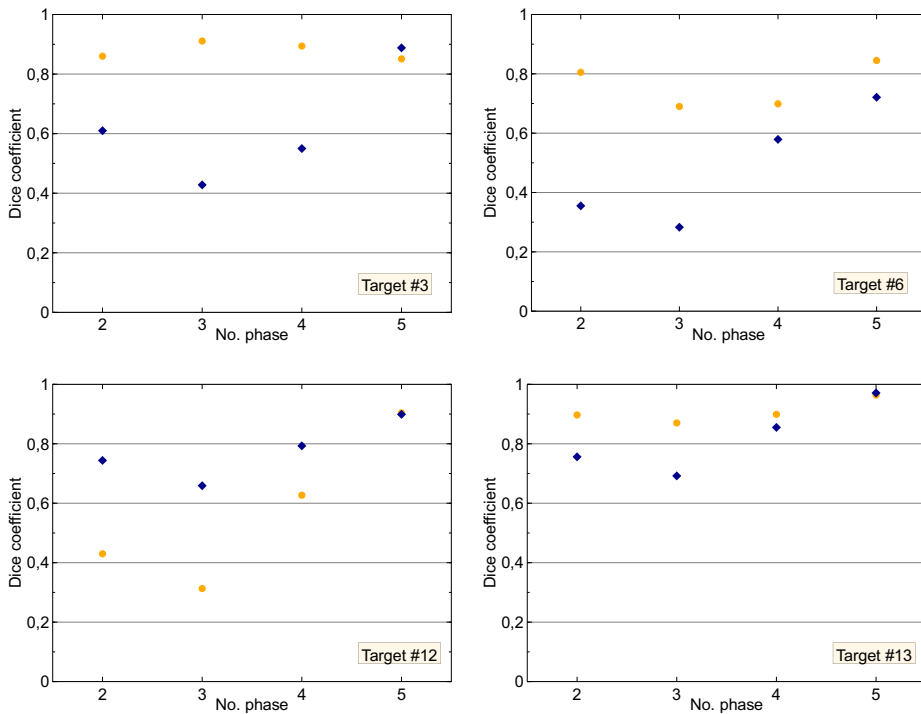
Figure 4.9: Dice coefficients between the targets of each phase and of the reference phase (Ph1), for three patients. Blue diamonds refer to the results without registration, orange circles refer to the registration with fiducials COM translation

No registration corresponds to the situation of an ideal intra-fraction alignment and no respiratory motion compensation, which amounts to a fiducials mode treatment. The registration based on the fiducials COM translation mimics the Synchrony treatment mode. The comparison of the two modes allows determining the usefulness of the Synchrony tracking system for liver treatment.

Globally, the Dice coefficient is better after the rigid registration based on fiducials, except for targets #2 and #12.

Patient #3 is the patient that shows the larger motion amplitude. Dice coefficients are better after the registration.

Patients #5 and #9 are two patients for which the deformations are the most important. For patient #5, the Dice coefficients are better after registration, but they are not very high. Regarding patient #9, the results for two targets are different. For target #13 the registration improves the Dice coefficients but it is not the case for target #12, which is very distant from the fiducials.

A second registration mode taking into account both the fiducials translation and rotation has been applied in the cases for which the registration based on fiducials translation did not improve the Dice coefficients, i.e. target #2 and #12. The results are shown in Figure 4.10.
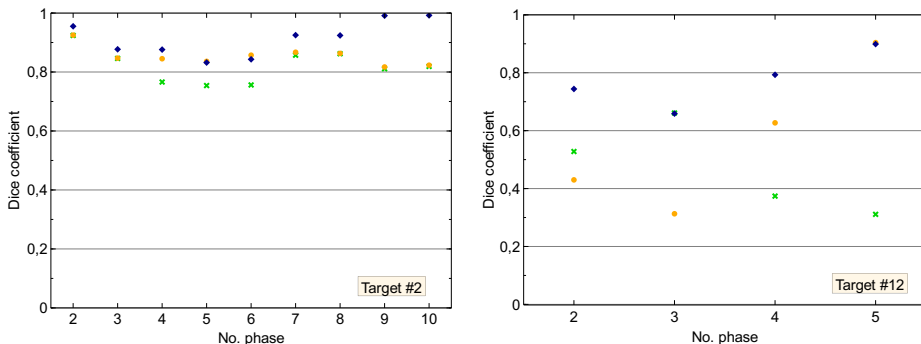
Figure 4.10: Dice coefficients between the targets of each phase and of the reference phase (Ph1), for target #2 4.10(a) and target #12 4.10(b). Blue diamonds refer to the results without registration, orange circles refer to the registration with fiducials COM translation and pink crosses refer to the registration with translation and rotation of the fiducials

The Dice coefficients obtained with this registration mode are mostly worse than those obtained after registration using the fiducials COM translation. In the case of target #12, this result was expected given that the target is very distant to the fiducials pattern. The fiducials and target motion is also very different. Regarding target #2, this is maybe due to the deformations in the fiducials pattern. The Absor function searches the

most appropriate rotation for all fiducials, but the presence of deforma-
tions could induce a wrong rotation. The mean RBE is low, namely 1.5
mm, but maximal values reach 4.9 mm.
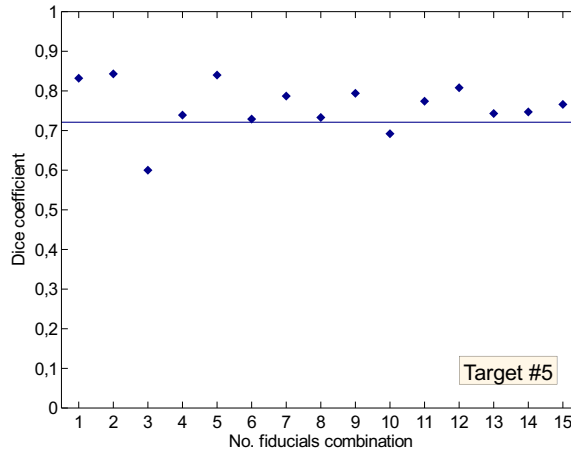
Figure 4.11: Dice coefficient for each possible combination of fiducials, for target #5,
Ph2 registered to Ph1

Program automation that allows testing all possible combinations of se-
lected fiducials, brings an overview of the possible results.
Dice coefficients obtained for each possible combination of fiducials are
shown in Figure 4.11 for target #5 and for registration based on fiducials
translation only.

4.3.4.2   Distance between target and volume center of mass

The distance between the COM of the two structures is used to quantify
the discordance between the fiducials and target movements. The dis-
tances between the COM of all phases before and after registration based
on fiducials are presented for some patients, in Figure 4.12. The results
for registration modes with only translation and with translation and ro-
tation of fiducials COM were shown.
In all cases, except for targets #2 and #12, the GTVs of the two phases
are closer after the registration mimicking the Synchrony tracking system.
These results confirm results obtained regarding the Dice coefficients.
As for the Dice coefficient, the different distances between the COMs de-
pending on the fiducials combination are shown in Figure 4.13 for target
#5, for registration based on fiducials translation.
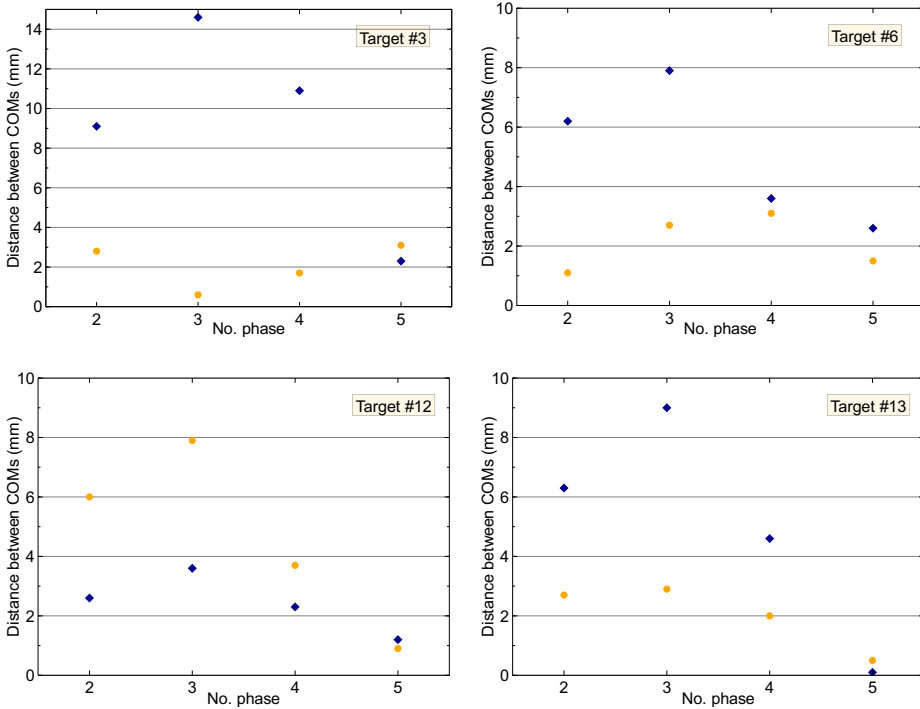
Figure 4.12: Distances between the target COM for each phase, before and after registration to the reference phase,for three patients and the target COM of the primary phase (Ph1). The blue diamonds refer to the results without registration, the orange circles refer to the registration with fiducials COM translation
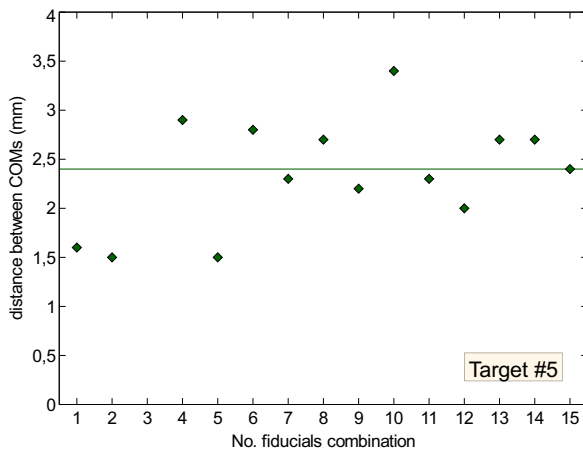
Figure 4.13: Distance between target COMs for each possible combination of fiducials, for target #5, Ph2 registered to Ph1

4.4   Discussion

Artifacts, due to the patient breathing irregularities, are present in the patient 4D PET-CT images. They appear in the sagittal and coronal view as a displacement of the liver on several slices. To limit the uncertainties, the study is conducted only when all the fiducials and the target are not in the artifact zone.

The first method has demonstrated the inconsistency between PET and CT images in combined 4D PET-CT acquisition. These inconsistencies do not impact the quality of the PET images, the CT being used only for attenuation correction. On the other hand, while CT images are acquired on very few respiratory cycles, the acquisition duration of PET images is much longer, which provides averaged images that are more representative for the reality and more consistent with the treatment.

Because of the inconsistency in 4D PET-CT images, an alternative method was used for the determination of target contours for each respiratory phase, using only the 4D CT images. Displacement vectors fields (DVF) were calculated from the CT images for the target contours determination on all respiratory phases. The algorithm used for the DVF calculation belongs to the team of Accuray. A second algorithm, from a MatLab free access program, has been tested. The limits of this algorithm have been shown by its evaluation. An improvement of this program with the introduction of a B-spline algorithm is currently under investigation in order to have a method not depending on Accuray.

In this study, the Dice coefficient analysis was combined with the displacement of the target COM to determine the overlapping quality. The distances between the target COM of the different phases registered to the primary phase are generally lower when translating the fiducials COM. The results, using the registration mimicking the Synchrony tracking, show that the correlation between the target and the fiducials COM movements is good.
Taking into account the rotations of the fiducual pattern does not improve the results. Note that an error in the localization of two fiducials relatively close to each other would introduce a large rotational uncertainty. The

Absor function used for registration searches the most appropriate rotation for all fiducials, but the presence of deformations in the fiducials pattern could induce wrong rotation.

The modification of the tracking method does not seem necessary, taking into account the accuracy of current method and the uncertainty introduced by considering the rotations.

Potential deformations in the different liver segments could lead to a bad correlation between the fiducials pattern and the tumor when the fiducials do not ideally surround the lesion. The larger the distance between internal markers and target, the more this effect will be significant. The recommendation of maximal distance between the target surface and the fiducials is 60 millimeters. The fiducials should be implanted as closely as possible to the tumor. If there are several targets in different segments, a set of fiducials must be implanted around each target.

The fiducials location plays a crucial role in the correlation between internal markers and target movements. For the case where the fiducials are distant from the target, the correlation between target and fiducials movements must be evaluated before treatment delivery.

A poor correlation would induce the misplacement of the target during certain respiratory phases. The target will receive less dose than the dose planned because of the error in the localization of the treatment delivery. In practice a GTV to Clinical Target Volume (CTV) margin of 5 mm is used. Additionally a margin of 3 mm is used to define the Planning Target Volume (PTV). A homogeneous dose to the PTV is planned. A non-perfect correlation of target and fiducial movement will not have a large impact on the GTV coverage. On the other hand this also means that a treatment without tracking is already adequate when using these large margins. Other departments use smaller margins though. It is important to take into account the margins when deciding on whether or not using Synchrony for liver treatments.

In case of a poor correlation between target and fiducials movements, it is possible to determine potential solutions to improve the target tracking or to find treatment alternatives.

The introduction of the possibility to exclude some fiducials which have

an inappropriate motion for the tracking in the MatLab program was investigated. This option allows determining the fiducials to track prior to treatment.

The determination of a threshold for the correlation (of correlation coefficient, tumor size, fiducials location regarding the target) from which a treatment without tracking will be preferred could bring a simple solution for the cases for which the target motion is negligible.

Respiratory movements observed around targets and fiducials are lower than expected. This is thanks to the presence of the elastic abdominal restraining belt that minimizes the movement amplitude. In cases where the movements are extremely low, the utility of the Synchrony mode treatment could be reconsidered. Creating an Internal Target Volume (ITV) would be a more robust solution because it avoids the introduction of uncertainty in beam delivery location. The decrease in treatment time using an ITV treatment would increase patient comfort. The choice of the imaging modality for the ITV definition is essential because the accuracy of target contouring is an important part of the quality of the treatment. As seen in the previous Chapter, the liver targets contouring is very difficult on CT images, especially for a 4D acquisition that is performed without injection of contrast product. 4D PET examination could be a solution. However, the interpretation of the information obtained on the PET images limits this possibility. Indeed, there is no SUV threshold value that can exactly differentiate healthy and tumorous tissues. Another solution would be the 4D MRI acquisition, because the contouring is more accurate and reproducible on MR images. Practical problems should be solved, such as the acquisition in the treatment position with immobilization equipments.

4.5   Conclusion

This study demonstrates that the target and the fiducials center of mass movements are well correlated during the breathing cycle. A poor correlation can occur when the fiducials are very distant from the tumor.

In cases where the tumor and fiducials motion amplitudes seem different, the correlation must be evaluated. If the correlation between the target and fiducials movements is poor, and for a low motion amplitude, the

possibility of using an ITV treatment should be considered.

This study provides an important information on the inconsistency between PET and CT images obtained with a combined 4D PET-CT device. PET information is more representative of the average movement during the treatment than CT information.

Chapter 5

Monte-Carlo Dose Simulation

5.1   Introduction

A treatment plan is optimized to provide the best possible dose distribution, delivering a high dose to the target volume and a low dose to the Organs At Risk (OARs). The actual received dose distribution can differ from the planned one, because of patient movements, inaccurate patient positioning, and organ motion. Respiratory and cardiac motions are the main contributors to the intrafraction motion, which effects mainly the organs in the thorax and the abdomen areas.

Variation in patient position and movement can be minimized with the help of precise patient positioning systems and rigid immobilization devices. For some anatomical sites, especially the abdominal area, the internal motion of the organs due to the breathing process presents a challenge. The two main dosimetric impacts of the organ motion are an insufficient dose coverage of the targeted tumor volume and an excessive dose to healthy tissues. Both effects potentially compromise the clinical results.[87]

Langen *et al.* [87] reviewed the literature regarding the quantification of intrafraction motion of several organs. As previously studied, the mean liver motion reported is 16 mm with a range of 5-40 mm, for patients in supine position. The diaphragm and the kidneys seem moving as much as the liver for normal patient breathing. For deep breathing, differences in motion amplitude are observed between organs. The average peak-to-trough ranges from 24 mm for the kidneys to 60 mm for the diaphragm.

The CyberKnife ® treatment of liver tumors is typically performed using the Synchrony™ respiratory tracking system in order to reduce the errors introduced by the respiratory target motion. This treatment mode allows to precisely target the tumor volume throughout its movements.

The treatment planning is performed on a static patient model, based on 3D CT images, and the dose is prescribed to the Planning Target Volume (PTV). The internal motion of the OARs present in the radiation field of view is not considered during treatment planning. The internal movements and deformations during breathing might cause organs being displaced relative to the tumor and thus to the radiation field, as the CyberKnife robot is tracking the tumor in Synchrony mode. This is not taken into account into the treatment plan and can lead to a dose increase

or decrease in the organs at risk, depending on the relative motion. The OARs affected by this problem are mostly located around the tumor, especially the stomach, the colon, the duodenum and the right kidney. This source of uncertainty is accentuated by the use of CT images acquired in blocked exhalation for the treatment planning dose calculation. Patients frequently force the exhalation and the images obtained do not correspond to a situation actually observed during normal breathing.

The method the most commonly used to include the movements of the target due to breathing in the calculation of the estimated 3D dose is adding safety margins around the tumor volume. According to ICRU Reports 50 [88] and 62[76], the Gross Tumor Volume (GTV) is defined as the volume containing demonstrated tumor and the Clinical Target Volume (CTV) encloses the GTV plus a margin to account for suspected tumor involvement. The PTV is defined by the CTV plus a margin to allow for geometrical variations such as patient movement, positioning uncertainties and organ motion. This method does not allow considering the movements and deformations of the OARs.

The 4D dose calculation challenge is to predict the received dose to the patient taking into account organ movements and deformations during the treatment. This involves following relative organ movements to accumulate dose throughout the respiratory motion. Displacements and Deformations undergone by the voxels in the CT images can be determined using Displacement Vector Fields (DVFs) calculated between the images of different phases of the respiratory cycle.

In a study regarding the evaluation of dose prediction errors and optimization convergence errors in 4D inverse planning of robotic stereotactic lung radiotherapy, Chan *et al.* [89] suggest that 4D Monte Carlo (MC) optimization is important to improve the dosimetric accuracy in robotic-based stereotactic body radiotherapy, despite the longer computation time.

The aim of this chapter is to evaluate the impact of tracking the target on the organs at risk comparing the dose distributions obtained using 3D and 4D dose calculations and to determine the dosimetric impact of the potential inconsistency between the movements of target and fiducials.

5.2   Methods and Materials

The calculation of a dynamic dose distribution was performed in retrospective mode. The dose calculated on the different breathing phases was accumulated. All dose grids were registered on a single reference image using the DVFs. The summation was done by adding the voxels of each dose grid weighted with the time duration of the phase.

The dose calculations were performed using the Monte Carlo System (MCS) software. This software, based on EGSnrc, has been developed by a physicist of the Oscar Lambret Center. The system allows an independent verification of the dose distribution calculated by the Treatment Planning System of Cyberknife and Tomotherapy.

The MC dynamic dose calculation based on a treatment plan and on 4D CT images, gives a more realistic result of the dose actually delivered taking into account tracking the target during the respiratory cycle. The impact of tracking the target on the dose to the OARs was evaluated and the dosimetric impact of the potential inconsistency between the movements of target and fiducials was determined, by comparing 3D and 4D dose calculations.

5.2.1   Dosimetric effect of tracking motion on OARs

By comparing 3D and 4D dose calculation the impact of organ motion during the treatment can be determined.

The plan applied on the 4D CT images originates from the plan optimized on the 3D blocked exhalation CT images. The reference phase of the 4D CT is used as the 3D dose calculation that is compared to the 4D accumulated dose distribution below. The direct comparison between the 3D dose distribution obtained from the TPS would have been possible but it is better to always compare the dose distributions both calculated with MCS to avoid any bias introduced by the dose calculation algorithm. The RTStruct file that was used for optimisation of the clinically used plan, was shifted to the coordinate system of the CT dataset corresponding to the reference phase of the 4D CT dataset. The translations applied to the RTStruct file is identical to the one used to shift the beams. This leads to an optimal dose distribution on the reference phase (one can expect that the small differences, because of attenuation alterations between 3D and 4D phase 1 datasets, are negligible).

> The MCS calculation performed on the CT images of the reference phase (Phase#1) of the 4D CT dataset without beams displacement, equivalent to a static dose plan
>
> *compared to*
>
> The MCS calculation performed on each phase of the 4D CT with all beams shifted using the COM of the fiducials (consistent with the Synchrony mode). All calculated dose distributions are registered on the reference phase (Phase#1) using the DIR algorithm. The final dose distribution results from the sum of all registered doses matrices

5.2.2   Accuracy of fiducial tracking

The accuracy of the Synchrony mode can be evaluated by comparing the 4D MCS results obtained when displacing the beams using the COM of the fiducials to a displacement according to the COM of the GTV (ideal tracking).

> The MCS calculation performed on each phase of the 4D CT with all beams shifted using the COM of the fiducials. All calculated dose distributions are registered on the reference phase (Phase#1) using the DIR algorithm. The final dose distribution results from summing all registered dose matrices
>
> *compared to*
>
> The MCS calculation performed on each phase of the 4D CT with all beams shifted using the COM of the target (as Synchrony with a perfect similarity between the target and the fiducials). All calculated dose distributions are registered on the reference phase (Phase#1) with the DIR algorithm. The final dose distribution results from summing all registered dose matrices

5.2.3   Utility of respiratory tracking

The comparison between the 4D dose calculation with and without tracking of the fiducials COM highlights the utility of respiratory tracking. For the dose calculation corresponding to the dose obtained without respiratory tracking, the beams are shifted as the target COM for all phases

and the dose distributions are not registered before being summed. This is equivalent to not displacing the beams while the patient is moving, or in other words, to treat the patient without using Synchrony tracking.

> The MCS calculation performed on each phase of the 4D CT with all beams shifted using the COM of the fiducials (as Synchrony). All calculated dose distributions are registered on the reference phase (Phase#1) using the DIR algorithm. The final dose distribution results from summing all registered dose matrices
>
> *compared to*
>
> The MCS calculation performed on each phase of the 4D CT with all beams shifted using the COM of the target. The calculated dose distributions are normalized and summed without registration

5.2.4   Dosimetric Impact of CTV margin

In clinical practice a margin of 5 mm is added from GTV to CTV (clinical target). This is partially to take into account uncertainties in GTV delineation and partially to include microscopic spread of tumor cells. The results of the uncertainty of the delineation reproducibility of the GTV are smoothed by the CTV margin (refer to chapter 3). That is why the impact of the CTV margin on previous results of the current chapter was evaluated.

The accuracy of fiducial tracking and the utility of respiratory tracking were studied for patient 3 without CTV margin. The dose planning was performed with the PTV defined as GTV plus a margin of 3 mm (named PTV_margin).

5.2.5   TPS evaluation - double calculation

MCS is a dose calculation system completely independent of the MultiPlan calculation algorithm. A comparison between TPS and MCS for the same treatment plan on the same CT dataset allows the evaluation of the accuracy of the TPS dose calculation algorithm. Concretely, the following calculations were compared:

> The TPS calculation performed on the 3D CT images
> *compared to*
> The MCS calculation performed on the 3D CT images
> without beams displacement

5.2.6   MCS calculation

The MCS Monte Carlo calculation software, that simulates the photon beam produced by the CyberKnife, is presented in detail in chapter 2.

All data needed to perform the Monte Carlo simulation are imported into the MCS software. These data include:

– The **3D CT images** used for treatment planning

– The **4D CT images**

– The DICOM file containing the **structures** (RTStruct)

– The **RTDose** file of the dose distribution calculated by the TPS. The MC dose engine calculates dose on the same grid as used by the TPS to avoid any bias.

– The **RTPlan** file corresponding to the parameters of the treatment plan of the TPS (number, size and monitor units (MUs) of beams, collimators used ...)

– A text file containing the coordinates of the **shift** to apply to the beams between the different phases to simulate the tracking of the robot. The shift was calculated for each phase, as the difference between the coordinates of the considered point (e.g. the center of mass of the fiducials, see higher).

When the data are imported in the software, the calculation can be started. Different parameters should be defined, as the number of particles and the number of Central Processing Units (CPUs) used for the calculation.
Each calculation corresponds to a task. The MCS software allows comparing two dose distributions corresponding to two different tasks.

The Graphical User Interface (GUI) enables the visualization of dose distributions in the 3 different views and the Dose Volume Histograms

(DVHs) for all contoured structures. The visualization window of the GUI of MCS in shown in Figure 5.1.

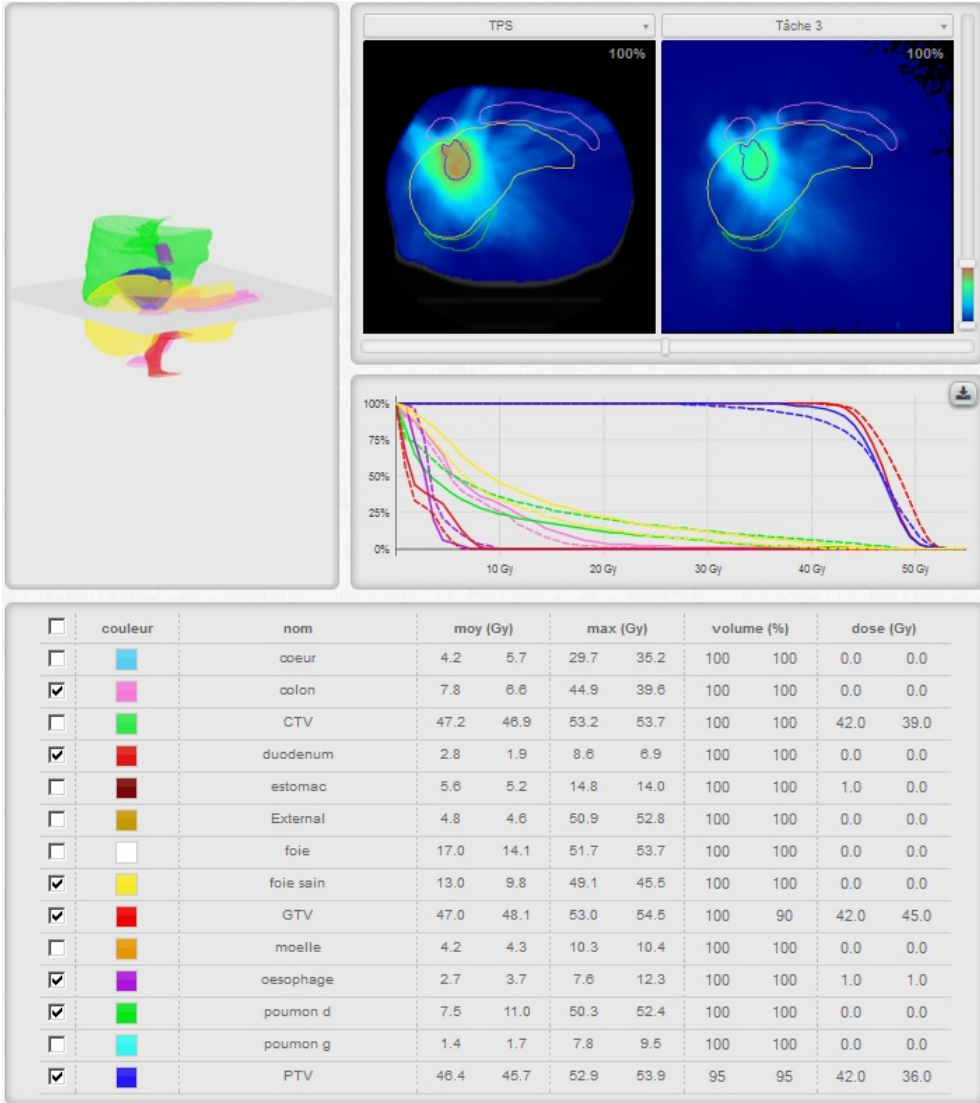|	couleur	nom	moy (Gy)		max (Gy)		volume (%)		dose (Gy)	
☐		coeur	4.2	5.7	29.7	35.2	100	100	0.0	0.0
☑		colon	7.8	6.6	44.9	39.6	100	100	0.0	0.0
☐		CTV	47.2	46.9	53.2	53.7	100	100	42.0	39.0
☑		duodenum	2.8	1.9	8.6	6.9	100	100	0.0	0.0
☐		estomac	5.6	5.2	14.8	14.0	100	100	1.0	0.0
☐		External	4.8	4.6	50.9	52.8	100	100	0.0	0.0
☐		foie	17.0	14.1	51.7	53.7	100	100	0.0	0.0
☑		foie sain	13.0	9.8	49.1	45.5	100	100	0.0	0.0
☑		GTV	47.0	48.1	53.0	54.5	100	90	42.0	45.0
☐		moelle	4.2	4.3	10.3	10.4	100	100	0.0	0.0
☑		oesophage	2.7	3.7	7.6	12.3	100	100	1.0	1.0
☑		poumon d	7.5	11.0	50.3	52.4	100	100	0.0	0.0
☐		poumon g	1.4	1.7	7.8	9.5	100	100	0.0	0.0
☑		PTV	46.4	45.7	52.9	53.9	95	95	42.0	36.0

Figure 5.1: Window of visualization

20 CPUs out of 60 were used for a task calculation, which allows running three tasks simultaneously. Dose was calculated using a resolution of 2 mm. The skin contours were used to avoid the dose calculation in the air

surrounding the patient, optimizing memory usage and calculation time. The phantom model, obtained using a stoichiometric calibration of the CT scanner, contained 15 bins.[90]

The parameters were common to all tasks except the number of particles, which was 100 million for 4D dose calculation and 500 million for 3D dose calculation. This allows having an equivalent statistics level between 3D and 4D dose calculation because of the summation of the five dose distributions for 4D. The number of particles is large enough to overcome the problems of statistics but still reasonable to allow a short calculation time (about 25 minutes).

For the 4D dose calculation, a task was run for each respiratory phase on the corresponding CT data. For each task, the beams were shifted between the different respiratory phases to simulate the displacement of the robot. Several displacement modes are available. The beams can be shifted as the Center Of Mass (COM) of the fiducials, as the COM of the target, or as any other precisely definable point in the CT images of each phase. The reference phase corresponds to the first phase.

The five 3D dose distributions obtained were summed using a MatLab program internally developed.
This program gives the possibility to registrate the distributions before the summation. Rigid and deformable registration are possible. The rigid registration of the dose distributions calculated for the different respiratory phases will not be used because only the dose on the PTV can be evaluated using this registration method. The deformable registration allows the evaluation of both the PTV coverage and the dose to the OARs. The deformable registration is performed using Displacement Vector Fields (DVFs) calculated from the 4D CT images, using a Deformable Image Registration (DIR) algorithm. The DIR algorithm is provided by Accuray and detailed in section 2.6.2 of chapter 4. The DVFs were tested in the previous chapter using the coordinates of the fiducials and the contours of the kidney. This demonstrated the high accuracy of the DVF calculation.

The visualization and the DVHs calculation were based on the structures that derive from the RTStruct attached to the 3D images used for the

treatment planning. In cases of 4D calculation, the RTStruct file has been shifted from the 3D CT to the 4D CT coordinate system.

Several tools are available for comparing two dose distributions. The MCS software provides the DVHs for the target volumes and the organs at risk. The visualization of the CT images, the structures and the dose distribution (as a color map) in the three different views, allows observing the differences between the dose distributions (as a shift) that would explain differences in the DVHs. Moreover, the mean and maximal dose, and the dose corresponding to a percentage of the volume, are given in a table for each structure. The percentage of volume and the dose can be change as desired. A dose profile can be obtained drawing a line on dose image.

The entire protocol for the dose distribution calculation and comparison is detailed in Appendix B.

5.2.7　Patient characteristics

The study was conducted for 4 patients treated for HCC or metastatic liver tumors. The tumors were located in different segments in the liver. Details are shown in Table 5.1. The tumor size corresponds to the size of the GTV.

No. patient		Gender	Age	Tumor location	Tumor size (cc)	Nearby organs
1		M	73	HCC junction SIV-SVIII	123	right lung : interface colon : interface
2		M	43	HCC junction SV-SVI	125	duodenum : interface right kidney : interface colon : interface
3		M	79	HCC SVII	16	coast : interface
4	GTV1	M	76	HCC SV	11	-
	GTV2			HCC SVII	17	right lung < 1cm

Table 5.1: List of patient characteristics

5.2.8   4D CT acquisition

The 4D CT images were acquired using the Aquilion™ LB (Toshiba Medical Co Ltd, Tokyo, Japan) coupled with the Real-time Position Management™ system (RPM) (Varian Medical Systems, Palo Alto, CA) for patient respiratory recording.

The patients were placed in supine position with the same immobilization materials as used during the treatment delivery, specifically the abdominal restraining belt. The parameters can be adapted for each patient but they are commonly fixed to 120 kV and 150 mAs for a patient with normal corpulence. The 4D image set was acquired in a second time, after the different series of 3D CT scans usually performed during the simulation session, with a maximal field of view of 20 cm in craniocaudal direction.

The acquisition of 4D images was performed continuously during patient free breathing accumulating several entire respiratory cycles. The RPM system recorded the respiratory signal during the acquisition time to retrospectively sort the images according to the phase of the respiratory cycle. The 4D CT was divided in five volumetric CT sets corresponding to five respiratory phases of equal duration time, and images were reconstructed with a millimetric slice thickness.

The maximal field of view used for the 4D CT acquisition is not sufficiently large in superior-inferior (SI) direction for a good calculation accuracy. The attenuation is not considered for some beams passing above or below the scan area. To rectify this problem, slices of the 3D CT dataset were added. The total height of the obtained 4D CT dataset was 40 cm.

5.3   Results

5.3.1   Dosimetric effect of tracking motion on OARs

The dosimetric impact of tracking motion on organs at risk is studied comparing the 3D dose distribution calculated on the images of Phase 1 of the 4D CT dataset and the 4D dose distribution with fiducials tracking (mimicking Synchrony), both calculated by MCS.
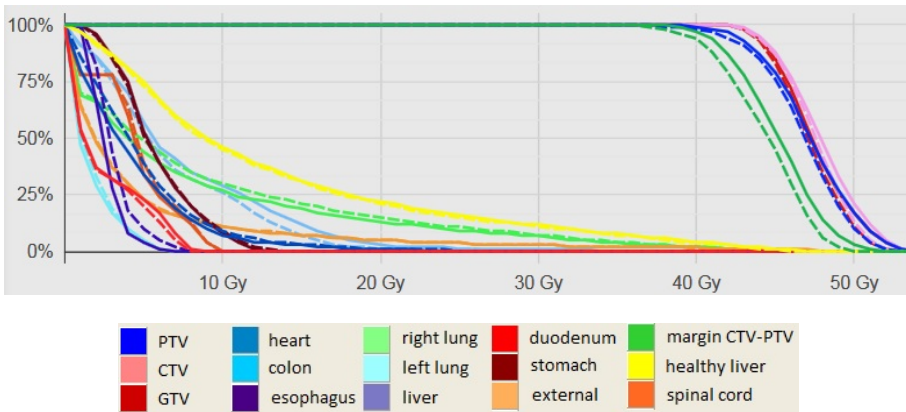

Figure 5.2: DVHs for 3D dose distribution calculated by MCS on the 4D_Ph1 CT images (solid line) and 4D dose distribution calculated by MCS with fiducials tracking (dashed line), for patient 1 [Volume in percentage on the ordinate]

Figure 5.3: OARs DVHs for 3D dose distribution calculated by MCS on the 4D_Ph1 CT images (solid line) and 4D dose distribution calculated by MCS with fiducials tracking (dashed line), for patient 1 [Volume in percentage on the ordinate]
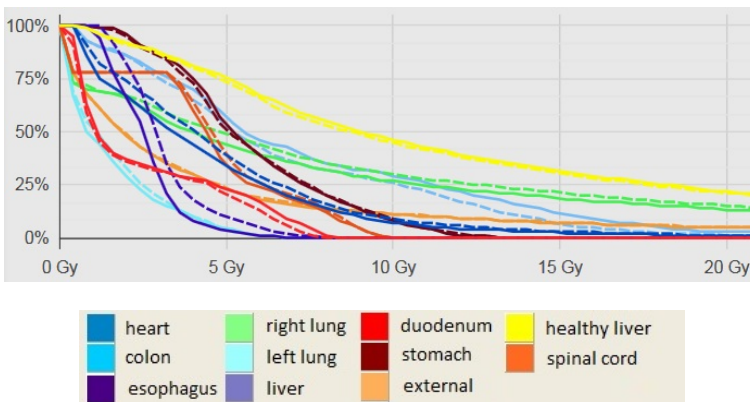
For patient 1, a very small difference is observed between the PTV DVHs. This difference could be caused by the inaccuracy of the correlation between the fiducials and the target movements. The dose delivered with fiducials tracking is slightly higher than the planned dose in the right lung and the esophagus. On the contrary, the dose to the colon is slightly lower. These differences are insignificant though.

The mean degradation of the PTV coverage is low but variations are more important in the margin volume from CTV to PTV, as observed in Figure 5.2. The GTV has a nonzero probability to be in this area where the dose coverage is rapidly degraded.

For better visibility of results, only the DVHs of organs at risk are presented for other patients if the difference observed between the target DVHs is negligible.

Figure 5.4: OARs DVHs for 3D dose distribution calculated by MCS on the 4D_Ph1 CT images (solid line) and 4D dose distribution calculated by MCS with fiducials tracking (dashed line), for patient 2

The dosimetric impact on the OARs is negligible, including for the nearby organs as duodenum and right kidney, regarding patient 2.

Figure 5.5: OARs DVHs for 3D dose distribution calculated by MCS on the 4D_Ph1 CT images (solid line) and 4D dose distribution calculated by MCS with fiducials tracking (dashed line), for patient 3

Slightly more dose is delivered in the duodenum with fiducial tracking, contrary to the heart that received less dose. Dose differences are not significant for patient 3.
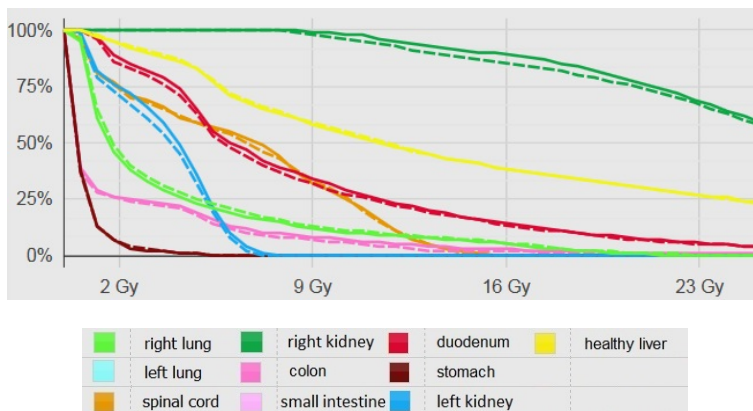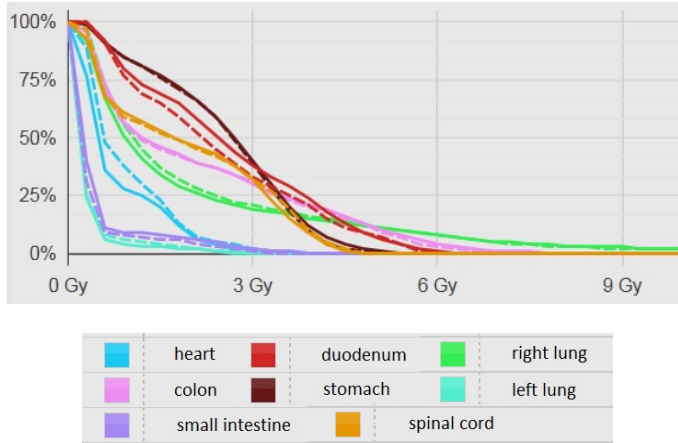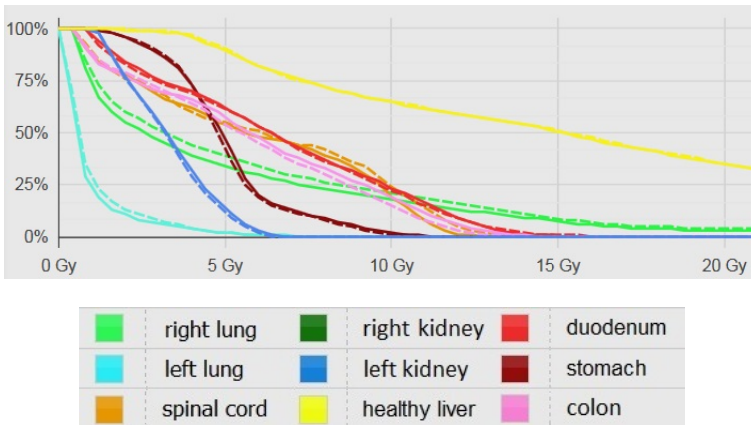

Figure 5.6: OARs DVHs for 3D dose distribution calculated by MCS on the 4D_Ph1 CT images (solid line) and 4D dose distribution calculated by MCS with fiducials tracking (dashed line), for patient 4

Regarding patient 4, only the right lung receives more dose when the organs motion is considered in the dose calculation.

5.3.2 Accuracy of fiducial tracking

The accuracy of the fiducial tracking is evaluated by comparing two 4D dose distributions, one by displacing the beams using the fiducials COM and the other by tracking the GTV COM. The DVHs obtained for the two tracking modes are shown in Figure 5.7 for patient 1.

The DVHs are similar for the target volumes and the OARs. A difference of 2 Gy on 95% of volume of the PTV is observed, which is insignificant.

Figure 5.7: DVHs for 4D dose distribution calculated by MCS with target tracking (solid line) and 4D dose distribution calculated by MCS with fiducials tracking (dashed line), for patient 1

The DVHs are similar when the tracking is based on fiducials or in target COM, for OARs and targets, as shown in Figures 5.8 and 5.9, for the three other patients.

Figure 5.8: DVHs for 4D dose distribution calculated by MCS with target tracking (solid line) and 4D dose distribution calculated by MCS with fiducials tracking (dashed line), for patient 2
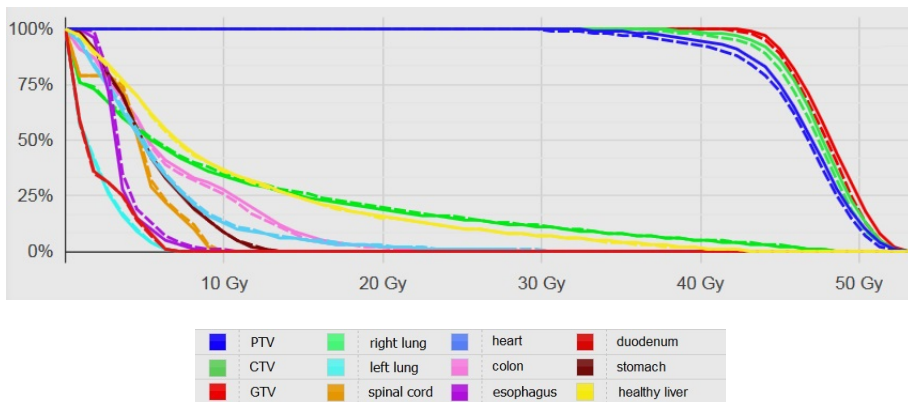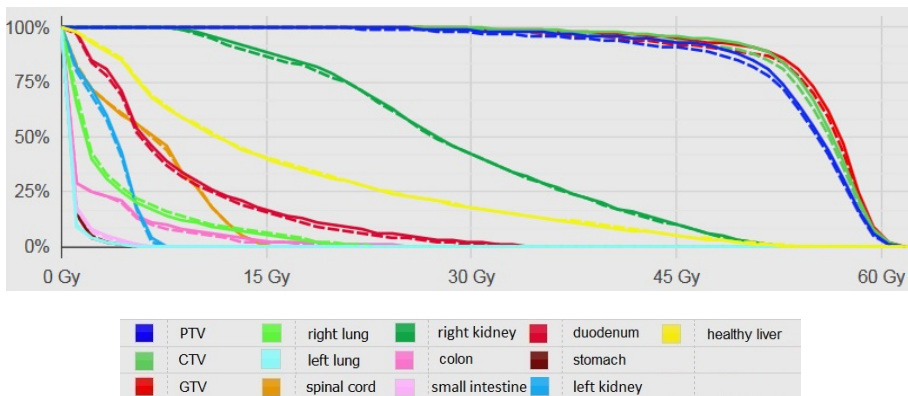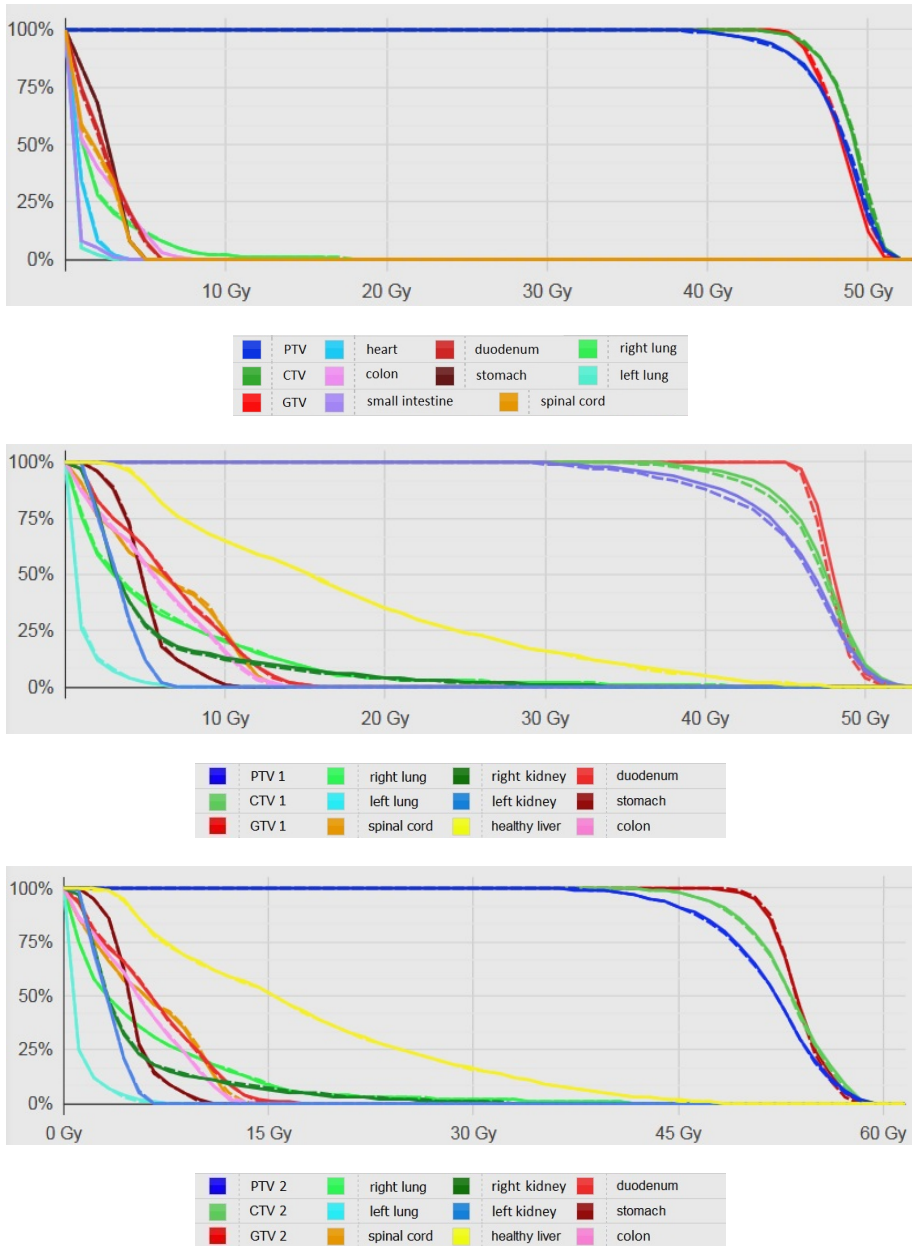
Figure 5.9: DVHs for 4D dose distribution calculated by MCS with target tracking (solid line) and 4D dose distribution calculated by MCS with fiducials tracking (dashed line), downwards for patient 3, patient 4 GTV1 and patient 4 GTV2

5.3.3 Utility of respiratory tracking

In this part, the 4D dose distribution with fiducials tracking (mimicking Synchrony) and the 4D dose without tracking are compared. They have been both calculated by MCS.
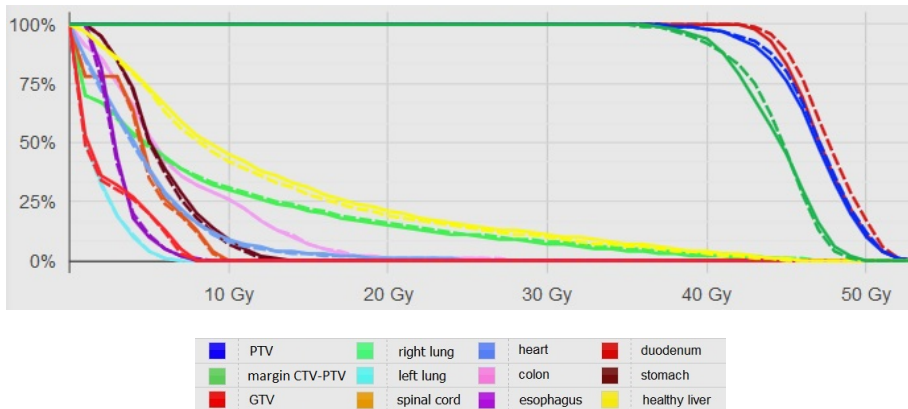
Figure 5.10: DVHs for 4D dose distribution calculated by MCS with fiducials tracking (solid line) and 4D dose distribution calculated by MCS without tracking (dashed line), for patient 1

The DVHs for patient 1 show that the fiducials tracking does not impact the dose to the OARs. We expected a large difference in the targeted volume, especially in the PTV, but the results show an insignificant difference between the two DVHs in the PTV. Only a difference of 2 Gy is observed on 95% of the volume of the PTV, and 0.2 Gy on 95% of the volume of the GTV. The coverage of the PTV and the dose to the OARs does not seem to be improved by tracking the tumor. This is partly due to the volume of the PTV that is large compared to the target movements amplitude.

The low amplitude of respiratory motion could be the cause of the results. The visualization of the dose distribution in coronal view for all phases allows to observe the amplitude of the movements of the target. The dose distributions for the 5 phases are ordered in Figure 5.11. The white square is the center of mass of the GTV and the white line is the position of the white square for phase 1.
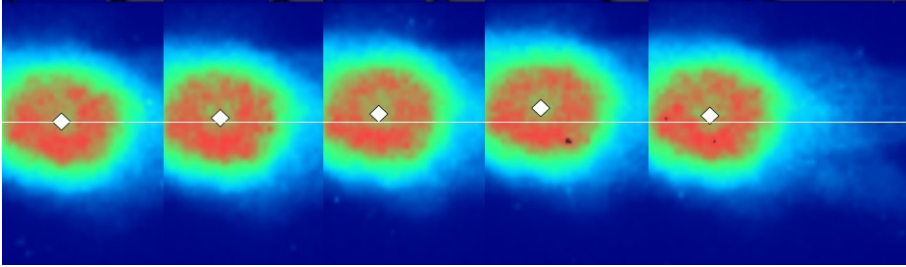
Figure 5.11: Dose distribution in coronal view for phases 1 to 5 (from left to right), for patient 1
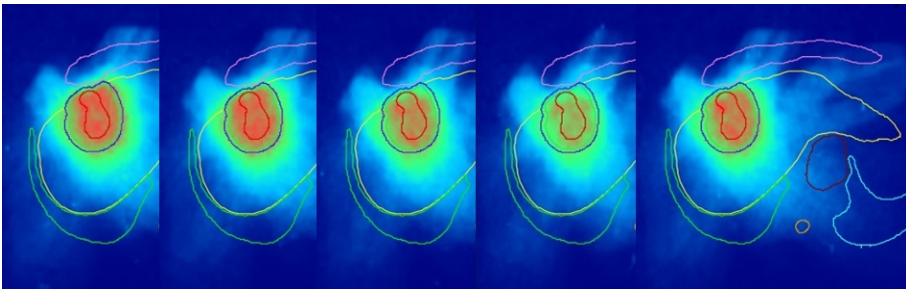
Figure 5.12: Dose distribution in transversal view for phases 1 to 5 (from left to right), for patient 1

The low movement in craniocaudal direction is visible. Only phase 4 is significantly displaced relative to Phase 1, with 9 mm of difference.

This is confirmed by the transversal slices in Figure 5.12. The dose to the GTV and PTV is mainly lower for Phase 4. This phase participates for only a fifth of the total 4D dose, which does not impact the PTV coverage.

The DVHs of the PTV for the five phases are in Figure 5.13. The degradation of PTV coverage is only significant for Phase 4.
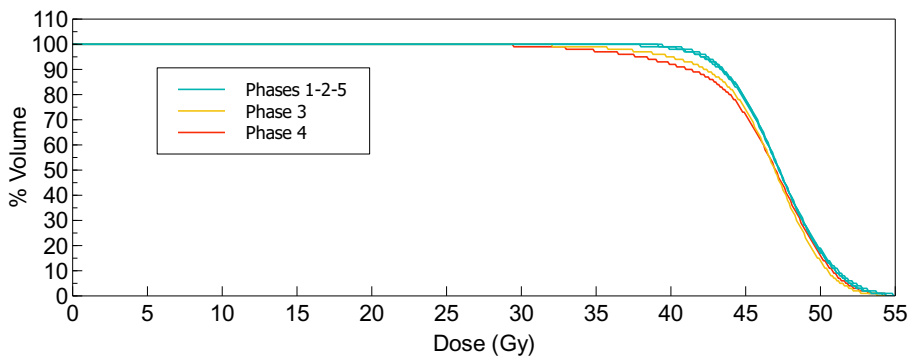
Figure 5.13: DVHs of PTV for all phases, for patient 1

As previously discussed, the variation of PTV coverage is the most important in the margin from CTV to PTV. The profile defined on the dose distributions corresponding to 4D_Phase1 and 4D_Phase4, illustrates that the dose differences are located at the edges of the high dose plateau, i.e. in the margin between CTV and PTV (Figure 5.15).
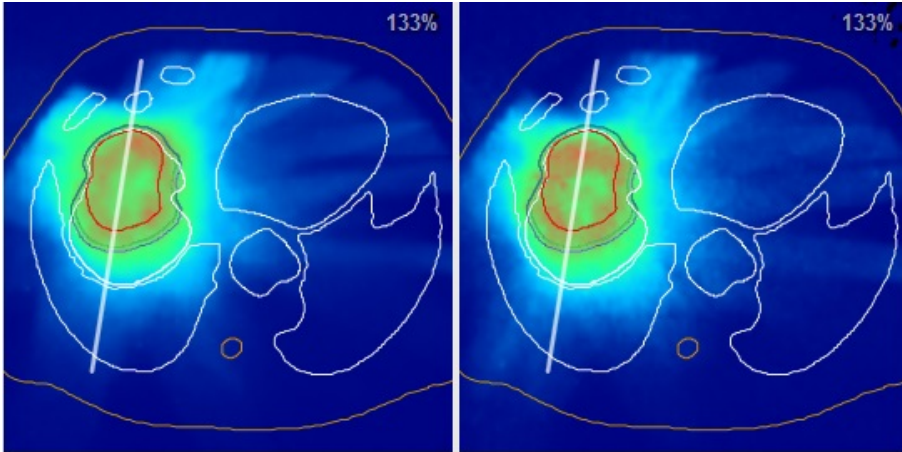
Figure 5.14: Dose distribution and profile line for dose calculation on 4D_Phase1 (left) and on 4D_Phase4 (right) images, for patient 1
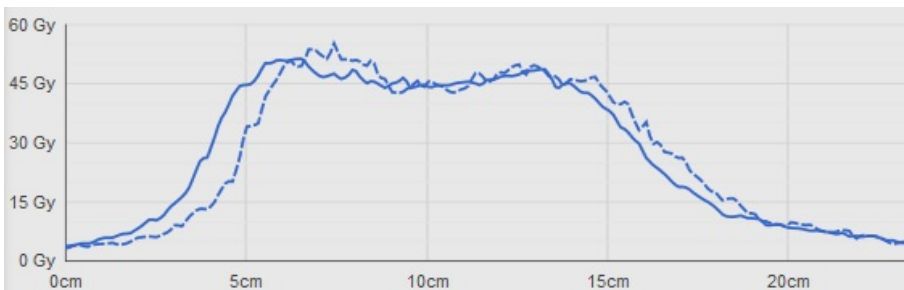
Figure 5.15: Dose profile for dose calculation on 4D_Phase1 (solid line) and on 4D_Phase4 (dashed line) images, for patient 1

The DVHs obtained for the margin in Figure 5.16 show that the coverage degradation is more important for the CTV-PTV margin.
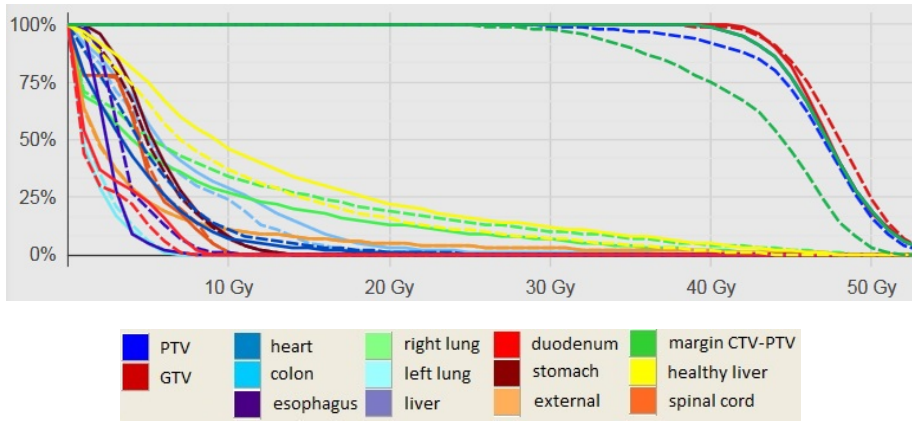
Figure 5.16: DVHs for dose calculation for Phase1 (solid line) and for Phase4 (dashed line), for patient 1 [Volume in percentage on the ordinate]

The results for patient 2 (Figure 5.17) are even more spectacular. No difference is observable between the dose to the targets volumes and OARs. Only the right kidney receives a higher dose whithout fiducials tracking. The maximal amplitude is 7 mm for the fiducials COM and 4 mm for the target COM.

The DVHs for the phase the most distant from the phase 1, in Figure 5.18, show the degradation of the PTV coverage if the beam is fixed during free breathing.

Figure 5.17: DVHs for 4D dose distribution calculated by MCS with fiducials tracking (solid line) and 4D dose distribution calculated by MCS without tracking (dashed line), for patient 2
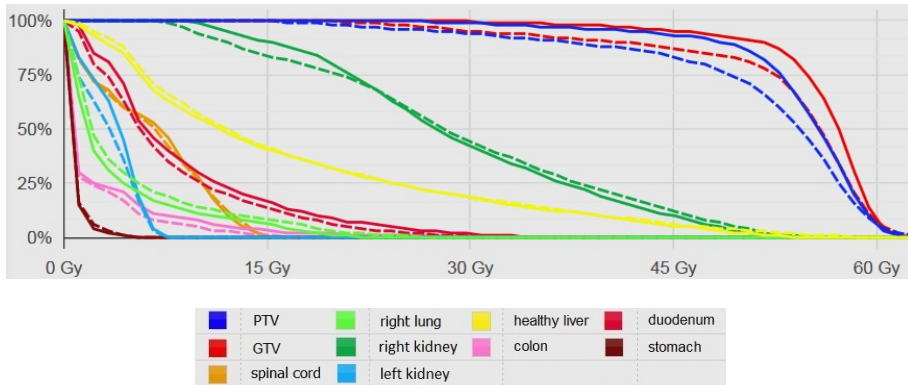
Figure 5.18: DVHs for 3D dose distribution calculated by MCS on the 4D_Ph1 CT images (solid line) and 3D dose distribution calculated by MCS on the 4D_Ph3 CT images (dashed line), for patient 2

The DVHs of the target and OARs for patient 3 are shown in Figure 5.19. The PTV is much degraded without tracking.

Figure 5.19: DVHs for 4D dose distribution calculated by MCS with fiducials tracking (solid line) and 4D dose distribution calculated by MCS without tracking (dashed line), for patient 3

Figure 5.20 shows the DVHs of the OARs and the two targets for patient 4. A degradation of the PTV coverage is visible for both targets. The differences in DVHs are more important than for the previous patients. This may be due to the larger amplitude of organ motion. The maximal motion amplitude is 13 mm for the fiducials COM, 7 mm for the target 1 COM and 10 mm for the target 2 COM.
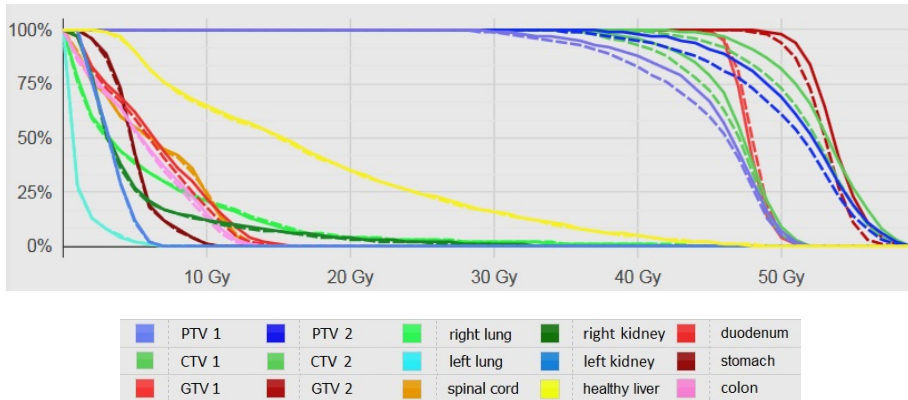
Figure 5.20: DVHs for 4D dose distribution calculated by MCS with fiducials tracking (solid line) and 4D dose distribution calculated by MCS without tracking (dashed line), for patient 4

The degradation of the PTV coverage is significant on Figures 5.21 and 5.22, which show the DVHs for 3D dose distributions calculated by MCS on the 4D_Ph1 and 4D_Ph3 CT images. Phase 3 is the phase the most distant than phase 1.
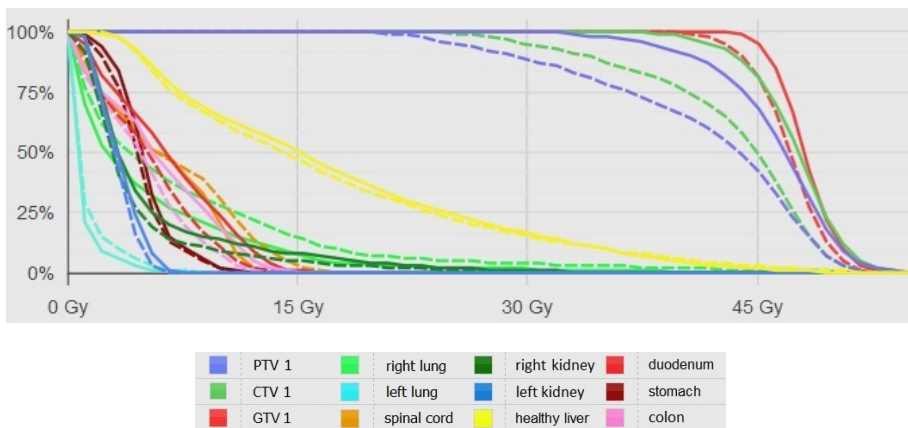
Figure 5.21: DVHs for 3D dose distribution calculated by MCS on the 4D_Ph1 CT images (solid line) and 3D dose distribution calculated by MCS on the 4D_Ph3 CT images (dashed line), for patient 4 GTV1
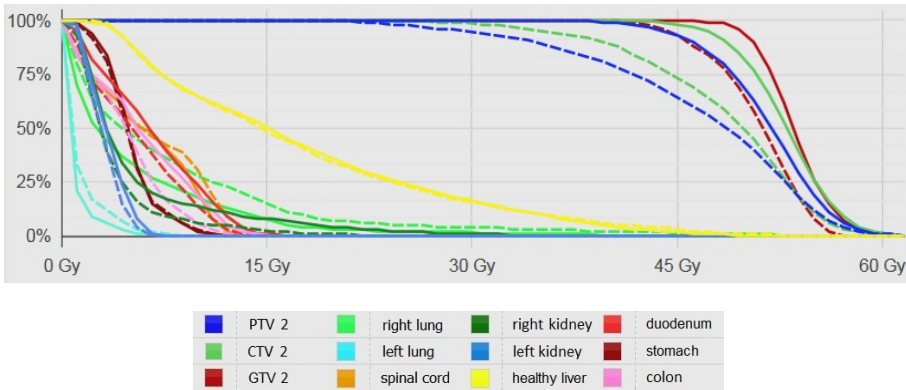
Figure 5.22: DVHs for 3D dose distribution calculated by MCS on the 4D_Ph1 CT images (solid line) and 3D dose distribution calculated by MCS on the 4D_Ph3 CT images (dashed line), for patient 4 GTV2

5.3.4   Dosimetric Impact of CTV margin

5.3.4.1   Accuracy of fiducial tracking
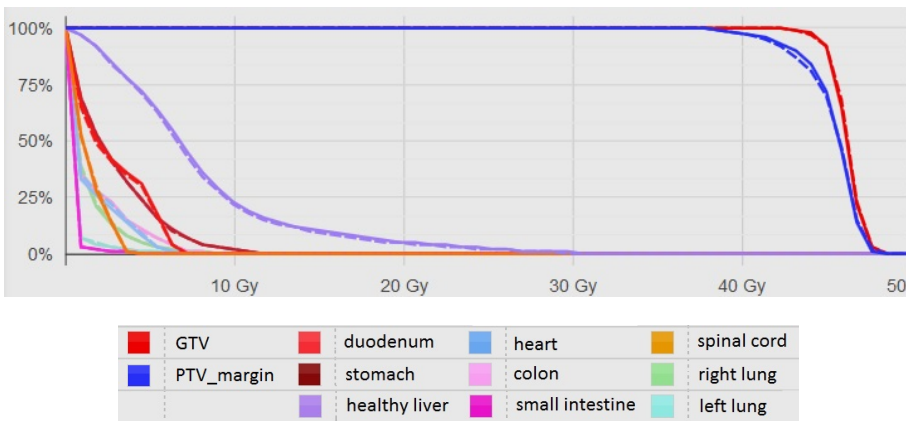
Figure 5.23: DVHs for 4D dose distribution calculated by MCS with target tracking (solid line) and 4D dose distribution calculated by MCS with fiducials tracking (dashed line), for patient 3 without CTV margin

The DVHs are perfectly overlapped that illustrates the good accuracy of the fiducial tracking (Figure 5.23). Same result was visible on Figure 5.9 for the same patient with CTV margin.
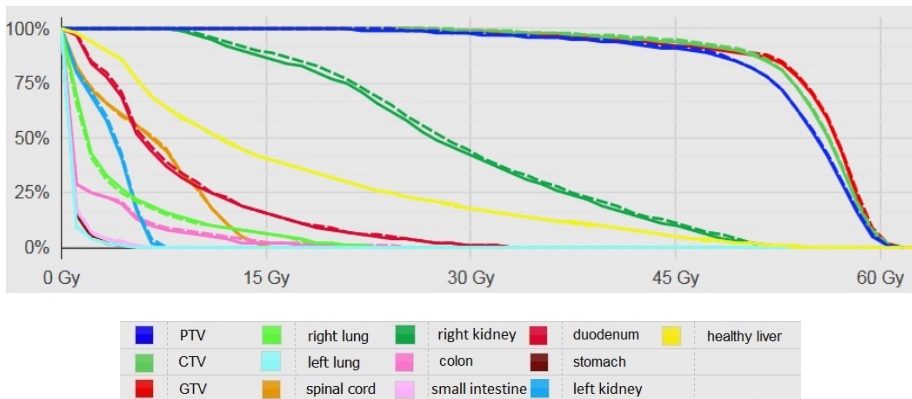
5.3.4.2   Utility of respiratory tracking
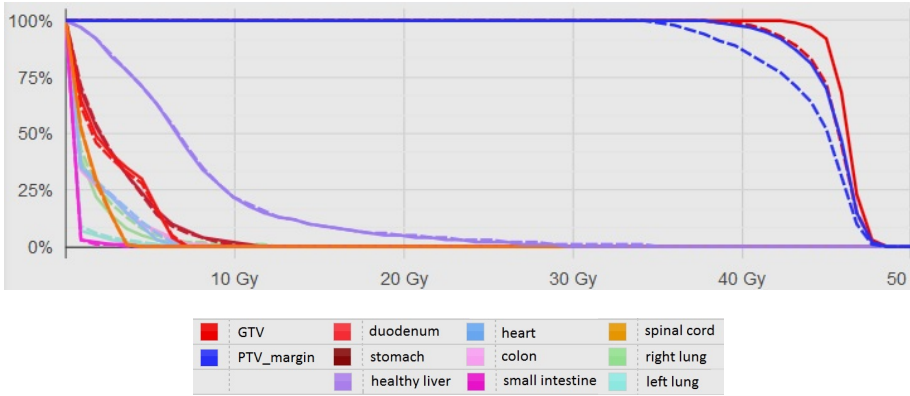
Figure 5.24: DVHs for 4D dose distribution calculated by MCS with fiducials
tracking (solid line) and 4D dose distribution calculated by MCS without tracking
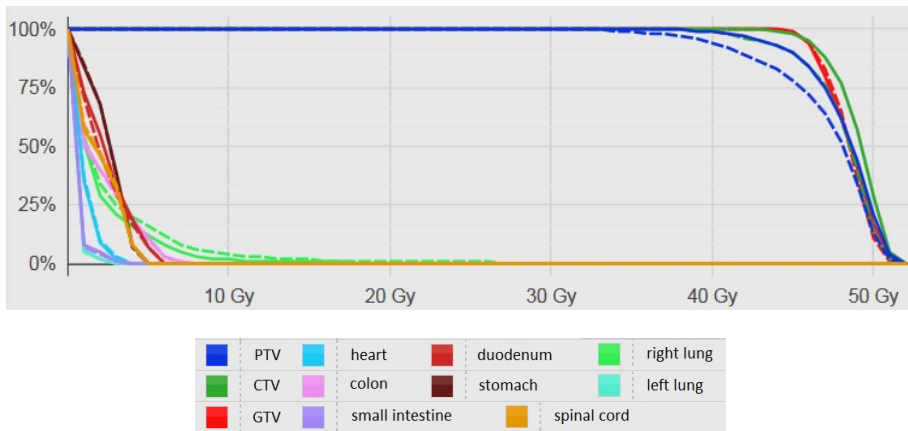(dashed line), for patient 3 without CTV margin

The dose coverage of the PTV_margin and of the GTV are degraded on
Figure 5.24 , while only the degradation of the PTV coverage was observ-
able whith CTV margin (refer section 5.3.3). The utility of respiratory
tracking seems more important when no CTV margin.
The DVHs for 3D dose distribution calculated by MCS on the 4D_Ph1
CT images and on the 4D_Ph3 CT images (dashed line) are shown on
Figure 5.25.
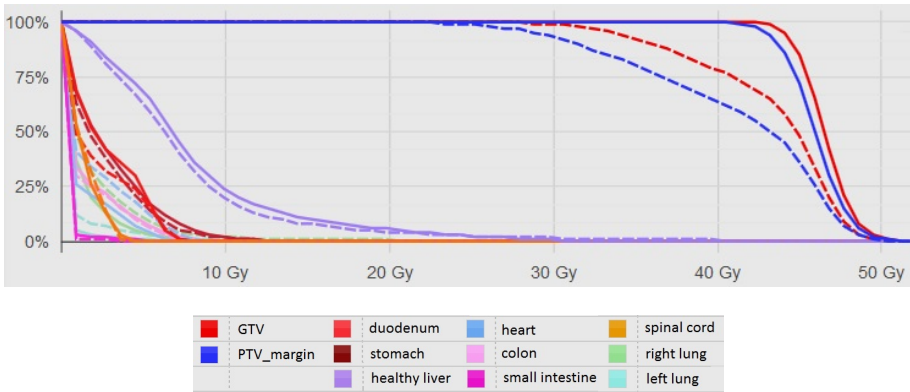
Figure 5.25: DVHs for 3D dose distribution calculated by MCS on the 4D_Ph1 CT
images and 3D dose distribution calculated by MCS on the 4D_Ph4 CT images
(dashed line), for patient 3 without CTV margin

The difference of dose coverage between Ph1 and Ph4 is very large, even for the GTV.

5.3.5 TPS evaluation - double calculation

Figures 5.26 and 5.27 illustrate the comparison between 3D dose distributions calculated by the TPS and by MCS for patient 1.

(a) 3D dose TPS   (b) 3D dose MCS
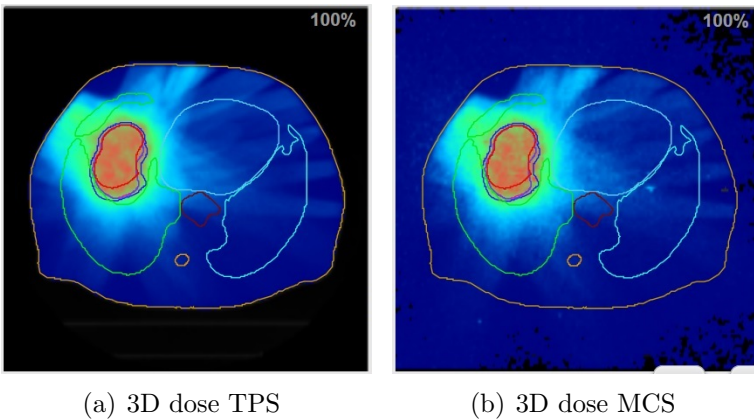
Figure 5.26: 3D dose distributions calculated by the TPS (a) and by MCS (b), for patient 1
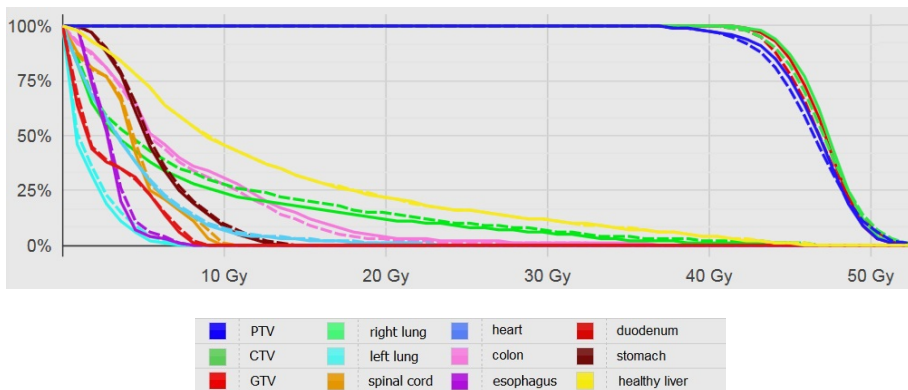
Figure 5.27: DVHs for 3D dose distributions calculated by the TPS (solid line) and by MCS (dashed line), for patient 1

The two 3D dose distributions seem similar on the color map in Figure 5.26. The DVHs confirm the similarity of the dose, especially in the

targeted volume. Only a small difference in the right lung is observed, certainly due to the difference in the cutoff energy of the electrons between the algorithm of the TPS (50 keV) and the MC simulations (10 keV).

The DVHs for the other three patients are shown below in Figures 5.28, 5.29, 5.30 and 5.31.
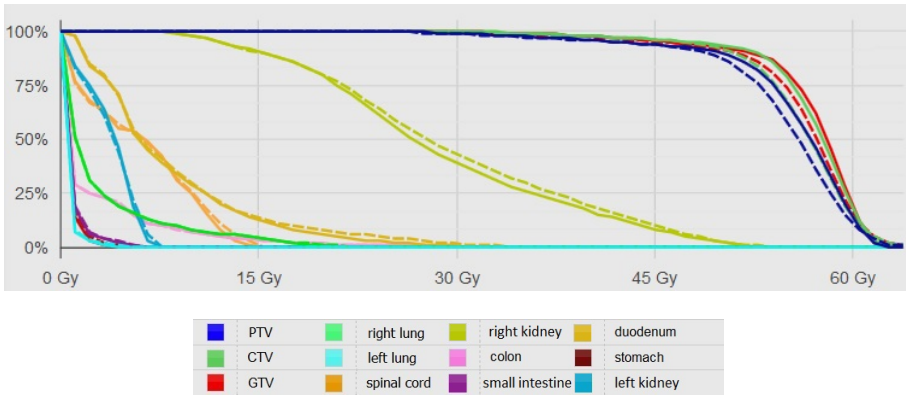
Figure 5.28: DVHs for 3D dose distributions calculated by the TPS (solid line) and by MCS (dashed line), for patient 2

For patient 2, the differences on the DVHs of the OARs are negligible and the dose is slightly higher in the target volumes. The differences are acceptable though.
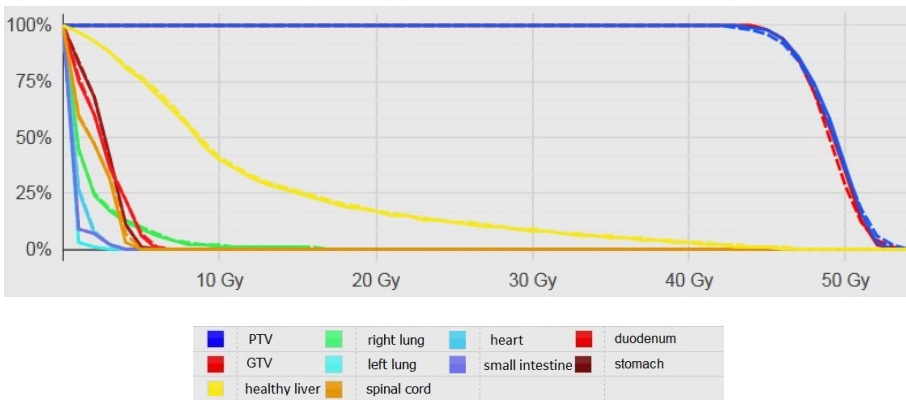
Figure 5.29: DVHs for 3D dose distributions calculated by the TPS (solid line) and by MCS (dashed line), for patient 3

No difference is observable on the DVHs for patient 3. The TPS and MCS calculations are perfectly consistent.
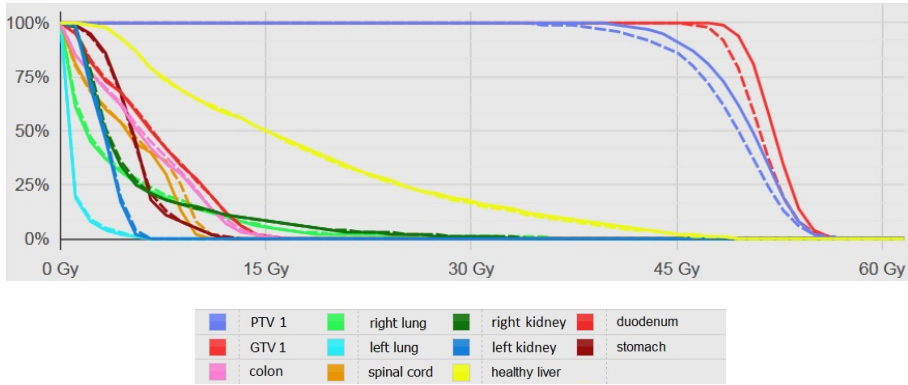
Figure 5.30: DVHs for 3D dose distributions calculated by the TPS (solid line) and by MCS (dashed line), for patient 4 GTV1

The DVHs related to the two targets of patient 4 show a better dose similarity for the GTV 2 that is located in the segment VII 5.31.
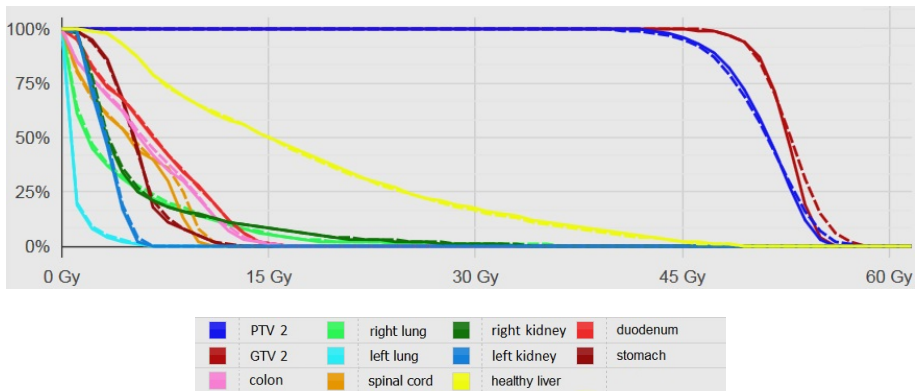
Figure 5.31: DVHs for 3D dose distributions calculated by the TPS (solid line) and by MCS (dashed line), for patient 4 GTV2

5.4   Discussion

4D dose accumulation can be performed using different methods. Heath *et al.* (2006) [91] deform the dose grid voxels to sum doses corresponding to different breathing phases. Mass conservation is taken into account by normalizing the density of the deformed voxels. In a more recent paper, Heath *et al.* (2008) [92] compared this method with a more conventional dose warping technique using tri-linear interpolation (the method used in current work). They obtained small differences between both methods for an extreme artificial case, but a limited resolution was used (4 x 4 x 2.5 mm^3), which certainly influences the results of the tri-linear interpolation method (in current work a resolution of 1 x 1 x 1 mm^3 was used). Their method was applied to lung tumors, where mass conservation is extremely important. This is not the case for liver tumors as the geometry is homogeneous.

More recently, it was realized that accumulation of energy deposition is more accurate compared to a direct dose summation ([93], [94]). This is especially the case when the voxel densities change, e.g. for the 4D dose distribution of lung tumors and for accumulating dose in adaptive radiotherapy where the GTV and certain organs at risk change in volume or mass (e.g. the parotids for head and neck cancer treatments). In current work, the voxel densities in liver do not change, neither does the volume of GTV and OARs. One could have a small influence on the dose accumulated in lung, but this is not an important parameter when optimizing liver treatments. The dose warping method was experimentally verified by using deformable gel phantoms ([95], [96]).

A residual uncertainty in the MC calculation is the application of the entire plan (all monitor units of all beams) on each breathing phase. The assumption that all phases are irradiated equally by all beams is an approximation. As the Cyberknife operates at 800 MU/min, and considering 5s for one respiratory cycle, 67 MUs are delivered per respiratory cycle. The minimal number of monitor units per beam is 45. If we take a concrete example (patient 3 in current study), there are only 4 beams delivered with less than 67 MUs. So in general every beam will at least irradiate all phases. On the other hand as the number of MUs is not a multiple of 67, a small part of each beam will be delivered to a limited number of phases. As the beams are randomly launched there will be no systematic effect

(i.e. no phase will be systematically under- or over irradiated). Only if there would be a perfect Synchrony between beam start and respiration phase, the first phase would be systematically over irradiated and the last underdosed. But this is never the case.

Firsly, the results demonstrate the good accuracy of the TPS 3D dose calculation. Only a small impact was observed regarding the dose distribution in lung, because of the usage of a relatively high energy cutoff during electron transport. This has a negligible impact for liver treatments though.

Concerning the 4D calculations, the tracking motion during breathing has a small effect on the dose to the OARs. The tracking motion could have a more important dosimetric impact when the target is near to organs, as the stomach or the duodenum, and for larger respiratory motion amplitudes.

The evaluation of the fiducials tracking shows that the Synchrony mode is not perfect. The inaccuracy of the tracking includes the uncertainties of the correlation between fiducials and target, and the uncertainties inherent to the tracking mode. Despite this, the dosimetric impact of this inaccuracy is insignificant. An improvement of the tracking method would not be useful, in any case not for the patients considered in current study. The results of the comparison between the dose distributions obtained with and without tracking were unexpected. No variation of the received dose for the OARs is observed and the PTV coverage is slightly degraded for some patients. However, the tracking is necessary in some cases, as patient 3, for which the PTV coverage is very degraded without tracking. The fiducials tracking is sufficiently accurate, although not really necessary for some patients studied. The main causes of this conclusion are the low amplitude of the internal movements, as demonstrated in the previous chapter, and the large size of the target volume.

This conclusion concerns the study performed with GTV-CTV margin, as that is realized in routine in the Oscar Lambret Center. In some Centers, no CTV is defined and the PTV is directly determined using a 3mm margin from GTV ([77], [78]). In this case, the conclusion must be put into perspective. As demonstrated in this chapter (Section 5.3.4.2), the respiratory tracking has a significant impact on dose coverage of target.

Margins applied for generation of CTV and PTV are large, namely 1 cm and 3 mm. The large volume of the PTV leads to a diminution of the impact of a dose modification in a small portion of the PTV, because of inaccurate tracking. The dose must be homogeneously delivered in this area to have a good coverage of the CTV taking into account all patient setup uncertainties (the 3 mm margin for the PTV is primarily for the inter fraction positioning uncertainty of the patient). The evaluation of received dose in the margin between CTV and PTV shown a larger degradation than in the whole PTV.

An alternative is to perform an ITV treatment. The comparison between both ITV and Synchrony treatment modes could be performed when the motion amplitude is low. An ITV treatment could be a time saving and a patient comfort improvement and is a more robust method with lower uncertainties.

5.5   Conclusion

The Monte Carlo simulation allowed the comparison of the target volume coverage between the fiducials tracking (Synchrony) and the perfect target tracking, and supported the results of the study regarding the correlation between the fiducials and the target during breathing (chapter 4). However, the utility of the respiratory tracking is questionable regarding the amplitude of respiratory motion and the CTV margin routinely used. This conclusion is applicable for the practice of Oscar Lambret Center but must be taken with caution for general case.

The present study evaluates the impact of incorporating organ motion into the planning process and the accuracy of Synchrony tracking. The method can be performed routinely without major strain on patient data needed. Only a 4D CT acquisition, a DVF calculation and the accessibility to MCS are needed. The method could be used to evaluate the treatment mode the most appropriate for patients with a low organ motion during breathing.

Including the uncertainties from intratreatment tracking motion into 3D

dose calculation does not seem necessary given the accuracy of the current planning method.

These conclusions have to be taken with caution until adding additional results.

Conclusions and Prospects

The delivery of high radiation doses in few fractions using the Cyberknife system with Synchrony tracking has been shown to be a successful approach for the treatment of liver tumors. However, remaining uncertainties should be evaluated to ensure and/or improve the accuracy of the treatment. The main objective of this thesis was to quantify the various uncertainties, especially the method of target delineation by the radiation oncologist, the handling of internal movements during optimisation of the treatment plan, and handling of these movements during the treatment delivery (tracking).

The study related to the tumor delineation showed that the uncertainty bound to the operator is important relative to other uncertainties (mechanical, dose calculation...). The results demonstrated that the reproducibility of the target delineation on CT images without contrast enhancement is poor, with a non zero probability of extreme outliers. This is due to the complex distinction between tumor and healthy tissue which have a similar density. CT images are routinely acquired with an injection of contrast product that substantially improves the target visualization. The study of the reproducibility of contouring by a physician on an enhanced contrast CT shows a better overlap of contoured targets with a higher average value and a lower variability of results. It is essential to continue to performe the CT imaging examinations with injection of contrast product, however, the uncertainty of the contouring remains significant. A dosimetric analysis demonstrated that the presence of contrast product during the acquisition of CT images for the treatment planning calculation does not have any influence on the dose distribution.

The reproducibility of the target delineation inter-physician, on CT images with contrast enhanced, has been studied. The bias introduced by the difference of their judgment, their experience or their learning, appears significant.

As MRI provides a better soft tissue contrast, the reproducibility of MRI based contouring was investigated and compared to the results obtained on CT. The results obtained showed a very good contouring reproducibility. The MRI modality appears to be very suitable for the target delineation in the liver. The intervention of a radiologist can provide a significant improvement, thanks to his interpretation of the different MR sequences available. The MR imaging seems to be a good alternative,

provided that the radiation oncologist is assisted by a skilled radiologist. Moreover to use the most adapted imaging modality, continuous education, training, and cross-collaboration of the radiation oncologist with other specialties can reduce the degree of variability in tumor delineation.

Another source of uncertainty when treating liver lesions by Cyberknife using the Synchrony tracking mode is bound to the movements and the deformations in the liver. The usage of dynamic imaging and the calculation of displacement vector fields of tissues during breathing allow studying movements and deformations in the liver and their impact on the accuracy of the respiratory tracking.
Respiratory movements observed around targets and fiducials are lower than expected, certainly due to the presence of the elastic abdominal restraining belt that minimizes the movement amplitude. The literature returns larger movements of abdominal organs, especially the liver, without restraining belt. Suramo *et al.* studied superior-inferior organ motion in 50 patients in supine position. The mean peak-to-through liver movement was 25 mm (range 10-40 mm) under normal respiration, and 55 mm (range 30-80 mm) under deep-breathing conditions. [97]
The correlation between the movements of the tumor and those of internal markers tracked during treatment is evaluated. A poor correlation would induce the misplacement of the robot during certain respiratory phases. The target will receive less dose because of the error in the localization of the treatment delivery.

We determined the usefulness of the consideration of the rotations of the fiducials in the model of respiratory tracking. The results illustrate that the rotations do not improve the results, partly because the presence of deformations in the fiducials pattern could induce wrong rotation. The modification of the tracking method does not seem necessary, taking into account the accuracy of current method and the uncertainty introduced by considering the rotations.

The results, using the registration mimicking the Synchrony tracking, show that the correlation between the target and the fiducials COM movements is good. However, the location of the fiducials plays a crucial role in the correlation between internal markers and target movements. The

fiducials should be implanted as closely as possible to the tumor and a
set of fiducials must be implanted around each target if there are several
lesions in different liver segments. In cases where the tumor and fidu-
cials motion amplitudes seem different, the correlation must be evaluated
before treatment delivery, especially when fiducials are distant from the
target.

In case of a poor correlation between target and fiducials movements, it is
possible to determine potential solutions to improve the target tracking or
to find treatment alternatives. Some fiducials which have an inappropriate
motion for the tracking can be excluded from the tracking process or a
treatment without tracking (creating an internal target volume (ITV))
could be considered in the extreme cases for which the target motion is
negligible. As the majority of the patients studied had a very low target
motion, an ITV treatment could have provided a good alternative, even
when the correlation between motion of target and fiducials is good.

The dosimetric study using Monte Carlo simulations allowed the compar-
ison of the target volume coverage between the fiducials tracking (Syn-
chrony) and the perfect target tracking, and supported the results of the
study regarding the correlation between the fiducials and the target dur-
ing breathing. However, the uselessness of the respiratory tracking has
been confirmed for some patient studied, partly due to the low amplitude
of target motion and the large CTV margin. The utility of the respiratory
tracking can differ depending on the treatment practices, as the definition
of a CTV margin.

The 4D MC calculation allowed also to evaluate the impact of incorpo-
rating organ motion into the planning process. The internal movements
do not seem to have any influence on the received dose to the OARs. This
conclusion is drawn from the study of some patient datasets, the existence
of particular cases is not excluded.

The 4D PET/CT study has clearly demonstrated that the correlation
between the 4D PET and the 4D CT is sometimes poor, because of the
different acquisition time. The 4D CT takes a snapshot of the breathing
pattern of the patient, which is not always representative for the treat-

ment. The actual motion of the tumor is better described by a slower imaging system such as 4D PET or even 4D MRI which averages the motion over a large number of respiratory cycles, which is much more consistent with the actual treatment delivery. Because of this inconsistency between 4D PET and 4D scan we had no choice than to use DVFs to study the correlation between target and fiducials motion. A 4D MRI sequence that provides visibility of target and fiducials would be the optimal solution. This is currently under investigation.

The algorithm used for the DVF calculation belongs to the team of Accuray. A second algorithm, from a MatLab free access program, has been tested. The limits of this algorithm have been demonstrated by its evaluation. An improvement of this program, with introducing the Insight Segmentation and Registration Toolkit (ITK) and more specifically the algorithms based on BSpline, is currently under investigation in order to have a method not depending on Accuray.

MR imaging modality is an important source of information for the target delineation in the liver. The use of MR images should gain importance in the current protocol of delineation. For that, the radiation oncologists should collaborate closely with the radiologists to precisely interpret the different MR imaging sequences to refine the delineation performed on CT images. Over time, the ideal solution would be to perform the delineation of target and OARs on the MRI images only. This is impossible yet because of the planning protocol that uses the CT data. The contours duplication from MR to CT images would demand a very accurate registration between both modalities. This registration is complicated, in part because of organ movements and deformations due to breathing and the different conditions in image acquisition.

One might expect that MRI will become more and more important in the near future, thanks to the quantity and quality of the information that this modality provides. In this way, MRI will probably replace CT for delineation as well as for treatment planning. Although some practical aspects need to be considered, the place of MRI in the process is evolving, which is clearly illustrated by the availability of MRI simulators [80].

The poor delineation precision, the low amplitude of respiratory motion, the large size of the lesions, the large CTV margin used, the complexity and low dosimetric impact of the respiratory tracking and the possible impact on OARs when not using 4D optimization are many reasons to think that the Synchrony tracking would not be necessary for most cases. The ITV treatment would be beneficial for these cases ?

Many questions arise regarding the current clinical practice and the possible ITV treatment concerning the liver tumors.

The question about the clinical impact of the different determined uncertainties is important. The fact that PTV degradation is not visible on the DVH (because of large PTV volume), does this mean that it is clinically irrelevant ? Other parameter should be used, e.g. the absolute PTV volume that is underdosed ?

Regarding the GTV delineation, the clinical practice should be more precisely defined. The combination of MRI and CT modalities is it always performed (visually or by rigid/deformable registration)? What it decided if MRI or contrast enhancement during CT acquisition is not available? For these cases, an ITV treatment should be systematically performed, depending (or not) on the GTV motion amplitude?

Regarding the low amplitude of organ motion, does the abdominal compression belt play a role ? 4D scan with and without belt should be acquired for several patients.

What is the exact meaning of CTV margin (microscopic spread or delineation uncertainty or combination of both)? And does CTV margin play a role in deciding between ITV/Synchrony treatment ?

The fiducials would be necessary when using ITV treatment, or only a Spine would be adequate? The imaging process would be precisely defined. For instance, the ITV treatment will request 4D CT images with a large field of view in craniocaudal direction.

How estimate the simplicity gain of using ITV treatment, as no fiducial implant and no respiratory tracking (gain in treatment time, patient comfort...)?

After all these questions resolved, a protocol should be established to decide on using Synchrony tracking or ITV treatment. Would a 4D calculation before treatment help to decide ? A 4D scan would be systematically acquired for each patient ?

References

[1] Human body anatomy. www.aokainc.com.

[2] V. T. Huynh. Couinaud liver segments in ct scanner. Vietnamese Radiology Network, 2011.

[3] Jordi Bruix and Josep M Llovet. Prognostic prediction and treatment strategy in hepatocellular carcinoma. *Hepatology*, 35(3):519–524, 2002.

[4] O De Dreuille, P Maszelin, H Foehrenbach, G Bonardel, and J-F Gaillard. Principe et technique de la tomographie par émission de positons (tep). *EMC-Radiologie*, 1(1):2–35, 2004.

[5] Antoine Wagner, Frederik Crop, Thomas Lacornerie, and Nick Reynaert. Characterization of recombination effects in a liquid ionization chamber used for the dosimetry of a radiosurgical accelerator. *J Vis Exp*, (87), 2014.

[6] Aristeidis Sotiras, Davatzikos Christos, Nikos Paragios, et al. Deformable medical image registration: A survey. 2012.

[7] Organisation mondiale de la sante (oms), 02 2014.

[8] Institut de veille sanitaire (InVS) lnstitut national du cancer Reseau des registres des cancers Francim, Service de biostatistique des Hospices Civils de Lyon (HCL). Evolution de l'incidence et de la mortalite par cancer en france entre 1980 et 2012. Technical report, 2013.

[9] Institut National du Cancer (INCa). Les cancers en france, edition 2013. Technical report, 2014.

[10] La radiotherapie : Apres un siecle d'evolution, des nouveaux traitements "sculptes" a la forme de la tumeur, 10 2003.

[11] A. L. Boyer C. Kappas E. Klein T. Rock Mackie M. Sharpe J. Van Dyk N. Papanikolaou, J.J. Battista. Tissue inhomogeneity corrections for megavoltage photon beams: the report of aapm task group 85. *Medical physics*, 2004.

[12] ICRU. Report 24. *International Commission on Radiation Units and Measurements, Bethesda, MD*, 1976.

[13] A. Dutreix. When and how can we improve precision in radiotherapy? *Radiother Oncol*, 2(4):275–292, Dec 1984.

[14] See Ching Chan, Chi Leung Liu, Chung Mau Lo, Banny K. Lam, Evelyn W. Lee, Yik Wong, and Sheung Tat Fan. Estimating liver weight of adults by body weight and gender. *World J Gastroenterol*, 12(14):2217–2222, Apr 2006.

[15] A Sam Beddar, Kristofer Kainz, Tina Marie Briere, Yoshikazu Tsunashima, Tinsu Pan, Karl Prado, Radhe Mohan, Michael Gillin, and Sunil Krishnan. Correlation between internal fiducial tumor motion and external marker motion for liver tumors imaged with 4d-ct. *Int J Radiat Oncol Biol Phys*, 67(2):630–638, Feb 2007.

[16] Edward D Brandner, Andrew Wu, Hungcheng Chen, Dwight Heron, Shalom Kalnicki, Krishna Komanduri, Kristina Gerszten, Steve Burton, Irfan Ahmed, and Zhenyu Shou. Abdominal organ motion measured using 4d ct. *Int J Radiat Oncol Biol Phys*, 65(2):554–560, Jun 2006.

[17] Torsten Rohlfing, Calvin R Maurer, Jr, Walter G. O'Dell, and Jianhui Zhong. Modeling liver motion and deformation during the respiratory cycle using intensity-based nonrigid registration of gated mr images. *Med Phys*, 31(3):427–432, Mar 2004.

[18] Gabor Szekely Golnoosh Samei, Christine Tanner. Advantage of a patient-speci

c respiratory motion model for the liver.

[19] Gary L. Davis, Jane Dempster, James D. Meler, Douglas W. Orr, Mark W. Walberg, Brian Brown, Brian D. Berger, John K. O'Connor, and Robert M. Goldstein. Hepatocellular carcinoma: management of an increasingly common problem. *Proc (Bayl Univ Med Cent)*, 21(3):266–280, Jul 2008.

[20] Hashem B. El-Serag and K Lenhard Rudolph. Hepatocellular carcinoma: epidemiology and molecular carcinogenesis. *Gastroenterology*, 132(7):2557–2576, Jun 2007.

[21] Jordi Bruix, Morris Sherman, and American Association for the Study of Liver Diseases , Practice Guidelines Committee. Management of hepatocellular carcinoma. *Hepatology*, 42(5):1208–1236, Nov 2005.

[22] M. Levrero. Viral hepatitis and liver cancer: the case of hepatitis c. *Oncogene*, 25(27):3834–3847, Jun 2006.

[23] Paul M. Silverman and Janio Szklaruk. Controversies in imaging of hepatocellular carcinoma: multidetector ct (mdct). *Cancer Imaging*, 5:178–187, 2005.

[24] Jorge A. Marrero, Robert J. Fontana, Sherry Fu, Hari S. Conjeevaram, Grace L. Su, and Anna S. Lok. Alcohol, tobacco and obesity are synergistic risk factors for hepatocellular carcinoma. *J Hepatol*, 42(2):218–224, Feb 2005.

[25] S. C. Larsson and A. Wolk. Overweight, obesity and risk of liver cancer: a meta-analysis of cohort studies. *Br J Cancer*, 97(7):1005–1008, Oct 2007.

[26] Tadatoshi Takayama. Surgical treatment for hepatocellular carcinoma. *Jpn J Clin Oncol*, 41(4):447–454, Apr 2011.

[27] Tadatoshi Takayama, Masatoshi Makuuchi, Masamichi Kojiro, Gregory Y. Lauwers, Reid B. Adams, Stephanie R. Wilson, Hyun-Jung Jang, Chusilp Charnsangavej, and Bachir Taouli. Early hepatocellular carcinoma: pathology, imaging, and therapy. *Ann Surg Oncol*, 15(4):972–978, Apr 2008.

[28] Josep M. Llovet, Andrew Burroughs, and Jordi Bruix. Hepatocellular carcinoma. *Lancet*, 362(9399):1907–1917, Dec 2003.

[29] K. N. Khan, H. Yatsuhashi, K. Yamasaki, M. Yamasaki, O. Inoue, M. Koga, and M. Yano. Prospective analysis of risk factors for early intrahepatic recurrence of hepatocellular carcinoma following ethanol injection. *J Hepatol*, 32(2):269–278, Feb 2000.

[30] M. Koda, Y. Murawaki, A. Mitsuda, K. Ohyama, Y. Horie, T. Suou, H. Kawasaki, and S. Ikawa. Predictive factors for intrahepatic recurrence after percutaneous ethanol injection therapy for small hepatocellular carcinoma. *Cancer*, 88(3):529–537, Feb 2000.

[31] R. Lencioni, C. Della Pina, and C. Bartolozzi. Percutaneous image-guided radiofrequency ablation in the therapeutic management of hepatocellular carcinoma. *Abdom Imaging*, 30(4):401–408, 2005.

[32] American Cancer Society.

[33] Tibor Tot. Adenocarcinomas metastatic to the liver. *Cancer, 85: 171177*, 85:171–177, 1999.

[34] Stphane Benoist, Antoine Brouquet, Christophe Penna, Catherine Juli, Mostafa El Hajjam, Sophie Chagnon, Emmanuel Mitry, Philippe Rougier, and Bernard Nordlinger. Complete response of colorectal liver metastases after chemotherapy: does it mean cure? *J Clin Oncol*, 24(24):3939–3945, Aug 2006.

[35] http://www.cancer.gov/cancertopics/factsheet/sites-types/metastatic.

[36] A. Lausch, K. Sinclair, M. Lock, B. Fisher, N. Jensen, S. Gaede, J. Chen, and E. Wong. Determination and comparison of radiotherapy dose responses for hepatocellular carcinoma and metastatic colorectal liver tumours. *Br J Radiol*, 86(1027):20130147, Jul 2013.

[37] Cneyt Ebruli Murat Beyzadeoglu, Gokhan Ozyigit. *Basic Radiation Oncology*, chapter 2, pages 119–125. 2010.

[38] Accuray Incorporated. *Equipment specifications.* 2009.

[39] W. Kilby, J. R. Dooley, G. Kuduvalli, S. Sayeh, and CR Maurer, Jr. The cyberknife robotic radiosurgery system in 2010. *Technol Cancer Res Treat*, 9(5):433–452, Oct 2010.

[40] Dieterich S. Taylor D. Wu X. Kilby W., Main W.M. In-vivo assessment of the synchrony respiratory tracking system accuracy. In *5th Annual CyberKnife User's Meeting*, Sunnyvale, CA, 2006. CyberKnife Society.

[41] Mischa Hoogeman, Jean-Briac Prvost, Joost Nuyttens, Johan Pll, Peter Levendag, and Ben Heijmen. Clinical accuracy of the respiratory tumor tracking system of the cyberknife: assessment by analysis of log files. *Int J Radiat Oncol Biol Phys*, 74(1):297–303, May 2009.

[42] Matthew John Allen. *Delivery and activation of contrast agents for Magnetic Resonance Imaging*. PhD thesis, California Institute of Technology, 2004.

[43] Kotaro Shimada, Hiroyoshi Isoda, Yuusuke Hirokawa, Shigeki Arizono, Toshiya Shibata, and Kaori Togashi. Comparison of gadolinium-eob-dtpa-enhanced and diffusion-weighted liver mri for detection of small hepatic metastases. *Eur Radiol*, 20(11):2690–2698, Nov 2010.

[44] Ali Muhi, Tomoaki Ichikawa, and Utaroh Motosugi. Diffusion-weighted imaging of the liver. In *Abdomen and Thoracic Imaging*, pages 253–278. Springer, 2014.

[45] Christoph Kenis, Filip Deckers, Bert De Foer, Franois Van Mieghem, Steven Van Laere, and Marc Pouillon. Diagnosis of liver metastases: can diffusion-weighted imaging (dwi) be used as a stand alone sequence? *Eur J Radiol*, 81(5):1016–1023, May 2012.

[46] Masayuki Kanematsu, Hiroshi Kondo, Satoshi Goshima, Hiroki Kato, Usuke Tsuge, Yoshinobu Hirose, Myeong-Jin Kim, and Noriyuki Moriyama. Imaging liver metastases: review and update. *European journal of radiology*, 58(2):217–228, 2006.

[47] Aisheng Dong, Hua Yu, Yang Wang, Hui Dong, and Changjing Zuo. Fdg pet/ct and enhanced ct imaging of tumor heterogeneity in hepatocellular carcinoma: Imaging-pathologic correlation. *Clin Nucl Med*, Oct 2013.

[48] Bernd Neumaier Bjrn Volkmer Albrecht Guhlmann Klaus Kleinschmidt Richard Hautmann Sven N. Reske Jorg Kotzerke, Jorgen Prang. Experience with carbon-11 choline positron emission tomography in prostate carcinoma. *European Journal of Nuclear Medicine*, Volume 27, Issue 9:1415–1419, 2000.

[49] Yuka Yamamoto, Yoshihiro Nishiyama, Reiko Kameyama, Keiichi Okano, Hirotaka Kashiwagi, Akihiro Deguchi, Masato Kaji, and Motoomi Ohkawa. Detection of hepatocellular carcinoma using 11c-choline pet: comparison with 18f-fdg pet. *J Nucl Med*, 49(8):1245–1248, Aug 2008.

[50] T. Beyer, D. W. Townsend, T. Brun, P. E. Kinahan, M. Charron, R. Roddy, J. Jerin, J. Young, L. Byars, and R. Nutt. A combined pet/ct scanner for clinical oncology. *J Nucl Med*, 41(8):1369–1379, Aug 2000.

[51] Thomas Beyer, Gerald Antoch, Stefan Mller, Thomas Egelhof, Lutz S. Freudenberg, Jrg Debatin, and Andreas Bockisch. Acquisition protocol considerations for combined pet/ct imaging. *J Nucl Med*, 45 Suppl 1:25S–35S, Jan 2004.

[52] SFPM RAPPORT. Recommandations pour la mise en service et lutilisation dun systme de planification de traitement en radiothrapie (tps). 2010.

[53] Barbara Vanderstraeten. *Biologically conformal radiation therapy and Monte Carlo dose calculations in the clinic*. PhD thesis, Ghent University, 2007.

[54] WR Nelson, H Hirayama, and DW Rogers. Report no: Slac-265. *The EGS4 Code System*, 1985.

[55] I Kawrakow and D Rogers. The egsnrc code system: Monte carlo simulation of electron and photon transport. 2000.

[56] Judith F Briesmeister et al. Mcnptm-a general monte carlo n-particle transport code. *Version 4C, LA-13709-M, Los Alamos National Laboratory*, 2000.

[57] Laurie S Waters. Mcnpx users manual. *Los Alamos.(Accesed in Apr 15, 2012 at http://mcnpx. lanl. gov/opendocs/versions/v230/MCNPX_2. 3.0 _Manual. pdf)*, 2002.

[58] F Salvat, JM Fernandez-Varea, E Acosta, and J Sempau. Penelope: A code system for monte carlo simulation of electron and photon transport. version 2001. *Nuclear Energy Agency Organisation for Economic Co-Operation and Development. Available at: http://www. nea. fr/dbprog/penelope. pdf*, 2003.

[59] S Agostinelli, John Allison, K ea Amako, J Apostolakis, H Araujo, P Arce, M Asai, D Axen, S Banerjee, G Barrand, et al. Geant4a simulation toolkit. *Nuclear instruments and methods in physics research section A: Accelerators, Spectrometers, Detectors and Associated Equipment*, 506(3):250–303, 2003.

[60] Omar Chibani and Chang-Ming Charlie Ma. Photonuclear dose calculations for high-energy photon beams from siemens and varian linacs. *Medical physics*, 30(8):1990–2000, 2003.

[61] D. Schaart W; van der Zee M. Tomsej C. Van Vliet-Vroegindeweij J. Jansen M. Coghe C. De Wagter B. Heijmen N. Reynaert, S. van de Marck. Monte carlo treatment planning - an introduction: Report 16 of the netherlands commission on radiation dosimetry. Technical report, NCS, Delft, june 2006.

[62] A Bielajew and I Kawrakow. High accuracy monte carlo calculations. In *World Congress on Medical Physics and Biomedical Engineering (Nice, 14–19 September) Med. Biol. Eng. Comput*, page 1096, 1997.

[63] DWO Rogers, CM Ma, B Walters, GX Ding, D Sheikh-Bagheri, and G Zhang. Beamnrc users manual national research council of canada. *NRCC Report PIRS-0509 (A) revK*, 2002.

[64] BRB Walters and DWO Rogers. Dosxyznrc users manual ionizing radiation standards national research council of canada. *NRCC Report PIRS-794*, 2002.

[65] Christian Barillot. *Fusion de données et imagerie 3D en médecine.* PhD thesis, 1999.

[66] Bertrand Delhay. *Estimation spatio-temporelle de mouvement et suivi de structures déformables. Application à limagerie dynamique du coeur et du thorax.* PhD thesis, Institut National des Sciences Appliquées de Lyon, 2006.

[67] Vincent Noblet. *Recalage non rigide d'images crbrales 3D avec contrainte de conservation de la topologie.* PhD thesis, Ph. D. thesis, Université Louis Pasteur-Strasbourg, 2006.

[68] Deshan Yang, Scott Brame, Issam El Naqa, Apte Aditya, Yu Wu, S Murty Goddu, Sasa Mutic, Joseph O Deasy, and Daniel A Low. Technical note: Dirart–a software suite for deformable image registration and adaptive radiotherapy research. *Medical physics*, 38:67, 2011.

[69] Noriyuki Kadoya, Yukio Fujita, Yoshiyuki Katsuta, Suguru Dobashi, Ken Takeda, Kazuma Kishi, Masaki Kubozono, Rei Umezawa, Toshiyuki Sugawara, Haruo Matsushita, and Keiichi Jingu. Evaluation of various deformable image registration algorithms for thoracic images. *J Radiat Res*, 55(1):175–182, Jan 2014.

[70] Kemal Arda, Nazan Ciledag, Bilgin Kadri Aribas, Elif Aktas, and Kenan Kse. Quantitative assessment of the elasticity values of liver with shear wave ultrasonographic elastography. *Indian J Med Res*, 137(5):911–915, May 2013.

[71] Chang Young Son, Seung Up Kim, Woong Kyu Han, Gi Hong Choi, Hana Park, Seung Choul Yang, Jin Sub Choi, Jun Yong Park, Do Young Kim, Sang Hoon Ahn, Chae Yoon Chon, and Kwang-Hyub Han. Normal liver elasticity values using acoustic radiation force impulse imaging: a prospective study in healthy living liver and kidney donors. *J Gastroenterol Hepatol*, 27(1):130–136, Jan 2012.

[72] W. F. Weitzel, K. Kim, J. M. Rubin, H. Xie, and M. O'Donnell. Renal advances in ultrasound elasticity imaging: measuring the compliance of arteries and kidneys in end-stage renal disease. *Blood Purif*, 23(1):10–17, 2005.

[73] M. M. Urie, M. Goitein, K. Doppke, J. G. Kutcher, T. LoSasso, R. Mohan, J. E. Munzenrider, M. Sontag, and J. W. Wong. The role of uncertainty analysis in treatment planning. *Int J Radiat Oncol Biol Phys*, 21(1):91–107, May 1991.

[74] P-J. Valette, F. Cotton, and F. Giammarile. [target volume contouring for radiotherapy planning: application of multimodalities imaging]. *Cancer Radiother*, 13(6-7):581–587, Oct 2009.

[75] C. F. Njeh. Tumor delineation: The weakest link in the search for accuracy in radiotherapy. *J Med Phys*, 33(4):136–140, Oct 2008.

[76] International Commission on Radiation Units and Measurements. Icru report 62. prescribing, recording and reporting photon beam therapy. supplement to icru report 50. 1999.

[77] Laura A Dawson, Andrew Zhu, Jennifer Knox, Sunil Krishnan, Tim Craig, Chandan Guha, Lisa Kachnic, Michael T Gillin, Theodore S Hong, and Kathryn Winter. Radiation therapy oncology group rtog 1112 randomized phase iii study of sorafenib versus stereotactic body radiation therapy followed by sorafenib in hepatocellular carcinoma. *Update*, 2013.

[78] Stanley H Benedict, Kamil M Yenice, David Followill, James M Galvin, William Hinson, Brian Kavanagh, Paul Keall, Michael Lovelock, Sanford Meeks, Lech Papiez, et al. Stereotactic body radiation therapy: the report of aapm task group 101. *Medical physics*, 37(8):4078–4101, 2010.

[79] Joakim H. Jonsson, Adam Johansson, Karin Sderstrm, Thomas Asklund, and Tufve Nyholm. Treatment planning of intracranial targets on mri derived substitute ct data. *Radiother Oncol*, 108(1):118–122, Jul 2013.

[80] Slobodan Devic. Mri simulation for radiotherapy treatment planning. *Med Phys*, 39(11):6701–6711, Nov 2012.

[81] Hiroki Shirato, Yvette Seppenwoolde, Kei Kitamura, Rikiya Onimura, and Shinichi Shimizu. Intrafractional tumor motion: lung and liver. *Semin Radiat Oncol*, 14(1):10–18, Jan 2004.

[82] Eric W Pepin, Huanmei Wu, Yuenian Zhang, and Bryce Lord. Correlation and prediction uncertainties in the cyberknife synchrony respiratory tracking system. *Med Phys*, 38(7):4036–4044, Jul 2011.

[83] David P Gierga, Johanna Brewer, Gregory C Sharp, Margrit Betke, Christopher G Willett, and George T Y Chen. The correlation between internal and external markers for abdominal tumors: implications for respiratory gating. *Int J Radiat Oncol Biol Phys*, 61(5):1551–1558, Apr 2005.

[84] L. A. Dawson, K. K. Brock, S. Kazanjian, D. Fitch, C. J. McGinn, T. S. Lawrence, R. K. Ten Haken, and J. Balter. The reproducibility of organ position using active breathing control (abc) during liver radiotherapy. *Int J Radiat Oncol Biol Phys*, 51(5):1410–1421, Dec 2001.

[85] P-Y. Bondiau, K. Bnzery, V. Beckendorf, D. Peiffert, J-P. Grard, X. Mirabel, A. Nol, V. Marchesi, T. Lacornerie, F. Dubus, T. Sarrazin, J. Herault, S. Marci, G. Angellier, and E. Lartigau. [cyberknife robotic stereotactic radiotherapy: technical aspects and medical indications]. *Cancer Radiother*, 11(6-7):338–344, Nov 2007.

[86] S. T. Kee. Fiducial placement to facilitate the treatment of pancreas ans liver llesion with the cyberknife system. *Technique and Application, Accuray recommendations.*

[87] KM Langen and DTL Jones. Organ motion and its management. *International Journal of Radiation Oncology* Biology* Physics*, 50(1):265–278, 2001.

[88] International Commission on Radiation Units and Measurements. Icru report 50. prescribing, recording and reporting photon beam therapy. 1993.

[89] Mark K H. Chan, Dora L W. Kwong, Anthony Tong, Eric Tam, and Sherry C Y. Ng. Evaluation of dose prediction error and optimization convergence error in four-dimensional inverse planning

of robotic stereotactic lung radiotherapy. *J Appl Clin Med Phys*, 14(4):4270, 2013.

[90] Vanderstraeten B., Chin P.W., Fix M., Leal A., Mora G., Reynaert N., Seco J., Soukup M., Spezi E., De Neve W., and Thierens H. Conversion of ct numbers into tissue parameters for monte carlo dose calculations: a multi-centre study. *Phys Med Biol*, 52(3):539–562, Feb 2007.

[91] Emily Heath and Jan Seuntjens. A direct voxel tracking method for four-dimensional monte carlo dose calculations in deforming anatomy. *Med Phys*, 33(2):434–445, Feb 2006.

[92] E Heath, J Seco, Z Wu, GC Sharp, H Paganetti, and J Seuntjens. A comparison of dose warping methods for 4d monte carlo dose calculations in lung. In *Journal of Physics: Conference Series*, volume 102, page 012013. IOP Publishing, 2008.

[93] Emily Heath, Frederic Tessier, and Iwan Kawrakow. Investigation of voxel warping and energy mapping approaches for fast 4d monte carlo dose calculations in deformed geometries using vmc++. *Phys Med Biol*, 56(16):5187–5202, Aug 2011.

[94] H Li, H Zhong, J Kim, T Nurushev, C Glide-Hurst, M Gulam, and IJ Chetty. Dosimetric difference between direct dose mapping and energy/mass transfer mapping for 4d dose accumulation. *Medical Physics*, 38(6):3692–3692, 2011.

[95] U. J. Yeo, M. L. Taylor, J. R. Supple, R. L. Smith, L. Dunn, T. Kron, and R. D. Franich. Is it sensible to "deform" dose? 3d experimental validation of dose-warping. *Med Phys*, 39(8):5065–5072, Aug 2012.

[96] J Adams and H Zhong. Tu-c-108-01: Verification of deformable dose calculation with phantom measurements. *Medical Physics*, 40(6):430–430, 2013.

[97] I. Suramo, M. Pivnsalo, and V. Myllyl. Cranio-caudal movements of the liver, pancreas and kidneys in respiration. *Acta Radiol Diagn (Stockh)*, 25(2):129–131, 1984.

[98] David A. Geller Allan Tsung. *Molecular Pathology Library - Gross and Cellular Anatomy of the Liver*, volume 5, chapter 1, pages 3–6. 2011.

[99] K. O. Babalola, B. Patenaude, P. Aljabar, J. Schnabel, D. Kennedy, W. Crum, S. Smith, T. F. Cootes, M. Jenkinson, and D. Rueckert. Comparison and evaluation of segmentation techniques for subcortical structures in brain mri. *Med Image Comput Comput Assist Interv*, 11(Pt 1):409–416, 2008.

[100] Thomas Beyer, Gerald Antoch, Stefan Mller, Thomas Egelhof, Lutz S. Freudenberg, Jrg Debatin, and Andreas Bockisch. Acquisition protocol considerations for combined pet/ct imaging. *J Nucl Med*, 45 Suppl 1:25S–35S, Jan 2004.

[101] T. Beyer, D. W. Townsend, T. Brun, P. E. Kinahan, M. Charron, R. Roddy, J. Jerin, J. Young, L. Byars, and R. Nutt. A combined pet/ct scanner for clinical oncology. *J Nucl Med*, 41(8):1369–1379, Aug 2000.

[102] P-Y. Bondiau, K. Bnzery, V. Beckendorf, D. Peiffert, J-P. Grard, X. Mirabel, A. Nol, V. Marchesi, T. Lacornerie, F. Dubus, T. Sarrazin, J. Herault, S. Marci, G. Angellier, and E. Lartigau. [cyberknife robotic stereotactic radiotherapy: technical aspects and medical indications]. *Cancer Radiother*, 11(6-7):338–344, Nov 2007.

[103] Edward D. Brandner, Andrew Wu, Hungcheng Chen, Dwight Heron, Shalom Kalnicki, Krishna Komanduri, Kristina Gerszten, Steve Burton, Irfan Ahmed, and Zhenyu Shou. Abdominal organ motion measured using 4d ct. *Int J Radiat Oncol Biol Phys*, 65(2):554–560, Jun 2006.

[104] Institut National du Cancer (INCa). Les traitements du cancer du foie. Technical report, 2011.

[105] Mariska D. den Hartogh, Marielle E P. Philippens, Iris E. van Dam, Catharina E. Kleynen, Robbert J H A. Tersteeg, Ruud M. Pijnappel, Alexis N T J. Kotte, Helena M. Verkooijen, Maurice A A J. van den Bosch, Marco van Vulpen, Bram van Asselen, and Hjg Desire

van den Bongard. Mri and ct imaging for preoperative target volume delineation in breast-conserving therapy. *Radiat Oncol*, 9:63, 2014.

[106] H. Cem Onal E. Topkan and M. Nur Yavuz. Managing liver metastases with conformal radiation therapy. *The Journal of Supportive Oncology*, 6, N.1, 2008.

[107] Isabelle M. Gagn and Don M. Robinson. The impact of tumor motion upon ct image integrity and target delineation. *Med Phys*, 31(12):3378–3392, Dec 2004.

[108] Carlo Greco, Gianpiero Catalano, Alfio Di Grazia, and Roberto Orecchia. Radiotherapy of liver malignancies. from whole liver irradiation to stereotactic hypofractionated radiotherapy. *Tumori*, 90(1):73–79, 2004.

[109] Emily Heath, Jan Unkelbach, and Uwe Oelfke. Incorporating uncertainties in respiratory motion into 4d treatment plan optimization. *Med Phys*, 36(7):3059–3071, Jul 2009.

[110] Kunihiko Izuishi, Yuka Yamamoto, Hirohito Mori, Riko Kameyama, Shintaro Fujihara, Tsutomu Masaki, and Yasuyuki Suzuki. Molecular mechanisms of [18f]fluorodeoxyglucose accumulation in liver cancer. *Oncol Rep*, 31(2):701–706, Feb 2014.

[111] Nikolaj K G. Jensen, Danielle Mulder, Michael Lock, Barbara Fisher, Rebecca Zener, Ben Beech, Roman Kozak, Jeff Chen, Ting-Yim Lee, and Eugene Wong. Dynamic contrast enhanced ct aiding gross tumor volume delineation of liver tumors: An interobserver variability study. *Radiother Oncol*, Mar 2014.

[112] Bernd Neumaier Bjrn Volkmer Albrecht Guhlmann Klaus Kleinschmidt Richard Hautmann Sven N. Reske Jrg Kotzerke, Jrgen Prang. Experience with carbon-11 choline positron emission tomography in prostate carcinoma. *European Journal of Nuclear Medicine*, Volume 27, Issue 9:1415–1419, 2000.

[113] Sang Hoon Jung, Sang Min Yoon, Sung Ho Park, Byungchul Cho, Jae Won Park, Jinhong Jung, Jin-Hong Park, Jong Hoon Kim,

and Seung Do Ahn. Four-dimensional dose evaluation using deformable image registration in radiotherapy for liver cancer. *Med Phys*, 40(1):011706, Jan 2013.

[114] Riccardo Lencioni and Laura Crocetti. Image-guided ablation for hepatocellular carcinoma. *Recent Results Cancer Res*, 190:181–194, 2013.

[115] Haisen S. Li, Hualiang Zhong, Jinkoo Kim, Carri Glide-Hurst, Misbah Gulam, Teamour S. Nurushev, and Indrin J. Chetty. Direct dose mapping versus energy/mass transfer mapping for 4d dose accumulation: fundamental differences and dosimetric consequences. *Phys Med Biol*, 59(1):173–188, Jan 2014.

[116] Gary Luxton, Paul J. Keall, and Christopher R. King. A new formula for normal tissue complication probability (ntcp) as a function of equivalent uniform dose (eud). *Phys Med Biol*, 53(1):23–36, Jan 2008.

[117] Pietro Majno, Gilles Mentha, Christian Toso, Philippe Morel, Heinz O. Peitgen, and Jean H D. Fasel. Anatomy of the liver: An outline with three levels of complexity - a further step towards tailored territorial liver resections. *J Hepatol*, Nov 2013.

[118] Alejandra Mendez Romero and Morten Hyer. Radiation therapy for liver metastases. *Curr Opin Support Palliat Care*, 6(1):97–102, Mar 2012.

[119] A. Niemierko. Reporting and analyzing dose distributions: a concept of equivalent uniform dose. *Med Phys*, 24(1):103–110, Jan 1997.

[120] Omid Nohadani, Joao Seco, and Thomas Bortfeld. Motion management with phase-adapted 4d-optimization. *Phys Med Biol*, 55(17):5189–5202, Sep 2010.

[121] H Foehrenbach G Bonardel JF Gaillard O de Dreuille, P Maszelin. *Principe et technique de la tomographie par mission de positons (TEP)*, volume 35-310-A-10. Encyclopdie Mdico-Chirurgicale, 2002.

[122] Lszl Rusk and Adm Pernyi. Automated liver lesion detection in ct images based on multi-level geometric features. *Int J Comput Assist Radiol Surg*, Oct 2013.

[123] Kenji Suzuki, Hieu Trung Huynh, Yipeng Liu, Dominic Calabrese, Karen Zhou, Aytekin Oto, and Masatoshi Hori. Computerized segmentation of liver in hepatic ct and mri by means of level-set geodesic active contouring. *Conf Proc IEEE Eng Med Biol Soc*, 2013:2984–2987, 2013.

[124] Giorgio Treglia, Elisabetta Giovannini, Davide Di Franco, Maria Lucia Calcagni, Vittoria Rufini, Maria Picchio, and Alessandro Giordano. The role of positron emission tomography using carbon-11 and fluorine-18 choline in tumors other than prostate cancer: a systematic review. *Ann Nucl Med*, 26(6):451–461, Jul 2012.

[125] Yuka Yamamoto, Yoshihiro Nishiyama, Reiko Kameyama, Keiichi Okano, Hirotaka Kashiwagi, Akihiro Deguchi, Masato Kaji, and Motoomi Ohkawa. Detection of hepatocellular carcinoma using 11c-choline pet: comparison with 18f-fdg pet. *J Nucl Med*, 49(8):1245–1248, Aug 2008.

[126] Deshan Yang, Scott Brame, Issam El Naqa, Apte Aditya, Yu Wu, S Murty Goddu, Sasa Mutic, Joseph O Deasy, and Daniel A Low. Technical note: Dirart–a software suite for deformable image registration and adaptive radiotherapy research. *Medical physics*, 38:67, 2011.

[127] Deshan Yang and Issam El Naqa. Dirart (deformable image registration and adaptive radiotherapy) software suite (version 1.0 a) user instruction manual.

[128] El Naqa I. Yang D. *DIRART Software Suite - User Instruction Manual*. 2009.

[129] Seung-Gu Yeo, Dae Yong Kim, Tae Hyun Kim, Sun Young Kim, Yong Sang Hong, and Kyung Hae Jung. Whole-liver radiotherapy for end-stage colorectal cancer patients with massive liver metastases and advanced hepatic dysfunction. *Radiat Oncol*, 5:97, 2010.

Appendix A.
Functionalities of the MatLab GUI

Input Data	
Reference RTStruct	Load Structures file (RTSS.dcm)
RTStruct 2	
Phase choice	Load text file with fiducials coordinates
	Select the phase/images set
Registration	
Fiducials VOI1	Select fiducials used for registration
Fiducials VOI2	Fiducials selected should be identical for the two VOIs
OK	Create text file "fiducials_temp.txt" (in the parent folder of RTSS) containing the coordinates of selected fiducials for registration
clear	Deselect all fiducials
Transform VOI2	Run the registration between the VOI2 and the VOI of Reference (mode of registration selected in dialog box) using the fiducials previously selected
	Save the new RTSS file (in the parent of the Reference RTSS)
VOIs information	
COM	Calculate the coordinates of the VOI COM
Volume	Calculate the absolute volume of the VOI (in cc)
Plot contours	Plot the contour points of the VOI
Plot surface	Display the surface of the VOI

Rigid Body Error (RBE)	Calculate the distance differences between each pair of fiducials between the fiducials of both images sets
	Create text file "rigid_body_error.txt" (in the parent folder of RTSS)
	Display the mean and maximal RBE
Details	Display the detail of all RBE
Test all combinations	Create a text file "list_combinations.txt" (in the parent folder of RTSS) containing the list of the different possible combinations of fiducials
	Create a text file "results.txt" (in the parent folder of RTSS) containing the distance between the COM, the volume ratio and the Dice coefficient for each fiducial combination
VOIs comparison	
COM distance	Calculate the distance between the COM of both VOIs compared (in mm)
Overlap parameters	Calculate the different overlap metrics, especially the volume ratio and the Dice coefficient between both VOIs compared
Graphical visualization	
Zoom	Allow to zoom in the graphical window
Pan	Allow to move the image in the graphical window
Rotate	Allow a 3D rotation of VOIs
Clear	Clean the graphical window

Appendix B.
Protocol for MCS dose calculation

MCS folder composition

– Create a folder for 3D CT and each phase of 4D CT (ex: IDpatient_3D)

<u>shift fiducials</u>

– Calculate the fiducials COM for 3D and all phases of 4D CT
– Calculate the shift between 3D CT and each phase of 4D CT (ex: COM_fid_Ph3 - COM_fid_3D)
– Create a text file for each shift (ex: Ph3 - 3D x_shift y_shift z_shift)
– Put the text files in the respective folders

<u>shift target</u>

– Calculate the target COM for RtStruct attached to 3D CT
– Apply the shift of fiducials COM between 3D and 4D_Ph1 CT (=COM_fid_Ph1 - COM_fid_3D) to obtain the target COM in 4D_Ph1 CT
– Deform this point with the DVFs to obtain the target COM in all phases of the 4D CT (using test_dvf_class.m)
– Calculate the shift between 3D CT and each phase of 4D CT (ex: COM_tar_Ph3 - COM_tar_3D)
– Create a text file for each shift (ex: Ph3-3D x_shift y_shift z_shift)
– Put the text files in the corresponding folders

<u>RtStruct for 4D cases</u>

– Shift all structures of the RtStruct attached to the 3D CT (using shift_rtstruct.m) to put the RtStruct in the 4D CT coordinate system (change the dicom_encoded_pixel_cells.m and dicom_prep_ImagePixel.m for writing rtss)
– Put the RtStruct shifted in each 4D folder

CT slices for 3D case

– Create a subfolder ct
– Put the 3D CT images in the subfolder

CT slices for 4D cases

– Shift the 3D CT dataset in the coordinate system of the 4D CT dataset:

> Remote Desktop -> Dosical1
> /home/mcs/MCS/src
> In file shift_CT.cc (l. 27-29) : Correct the 3 specific shifts for the patient
> Close and Save the file
> Compile : ./compile
>
> In the patient CT folder
> (ex: /home/mcs/MCS/release/traitments/IDpatient_3D/ct)
> Apply the shift to the CT dataset selected: shift_CT_all
> (Takes few minutes)
> A subfolder shifted containing the 3D CT images shifted is created in the folder /ct
>
> Remark: Use vi to modify the file
> (type i for being able to write, Escp for not being able to write and :x for exiting)

– Import the 3D CT dataset shifted in Oncentra MasterPlan
– Select and Import the slices to add in each 4D CT folder
– Put the 4D CT images in each 4D CT folder

MCS calculation comparison

MCS does not open two dose distributions from two different folders.

– Put all tasks to compare in the same folder for the visualization.